Title

Integrative Mapping of Cardiac Neural Patterning and Impulse Propagation: Implications for Arrhythmogenesis

Author

Zhu, Ching

Publication Date

2022

UNIVERSITY OF CALIFORNIA

Los Angeles

Integrative Mapping of Cardiac Neural Patterning and Impulse Propagation:

Implications for Arrhythmogenesis

A dissertation submitted in partial satisfaction
of the requirements for the degree Doctor of Philosophy
in Molecular, Cellular, and Integrative Physiology

by

Ching Zhu

2022

ABSTRACT OF THE DISSERTATION

Integrative Mapping of Cardiac Neural Patterning and Impulse Propagation: Implications for Arrhythmogenesis

by

Ching Zhu
Doctor of Philosophy in Molecular, Cellular, and Integrative Physiology
University of California, Los Angeles, 2022
Professor Kalyanam Shivkumar, Chair

Autonomic dysregulation in cardiovascular disease plays a major role in the pathogenesis of arrhythmias. Cardiac neural control relies on complex feedback loops consisting of efferent and afferent limbs, which carry sympathetic and parasympathetic signals from the brain to the heart and sensory signals from the heart to the brain. Cardiac disease leads to neural remodeling and sympathovagal imbalances with arrhythmogenic effects. Preclinical studies of modulation at central and peripheral levels of the cardiac autonomic nervous system have yielded promising results, leading to early-stage clinical studies of these techniques in atrial fibrillation and refractory ventricular arrhythmias, particularly in patients with inherited primary arrhythmia syndromes and structural heart disease. However, significant knowledge gaps in basic cardiac neurophysiology limit the success of these neuromodulatory therapies. At the level of the myocardium, remodeling of injured sympathetic nerves on the heart after myocardial infarction (MI) contributes to adverse outcomes such as sudden arrhythmic death, yet the underlying structural mechanisms are poorly understood. We sought to examine microstructural changes on the post-MI heart and to directly link these changes with electrical dysfunction. We developed a high-resolution pipeline for anatomically precise alignment of electrical maps with structural myofiber and nerve-fiber maps created by customized computer vision algorithms. Using this integrative approach in a mouse model, we identified distinct structure-function correlates to objectively delineate the infarct border zone, a known source of post-MI arrhythmias. During tyramine-induced sympathetic nerve activation, we demonstrated regional patterns of altered electrical conduction aligned directly with altered neuroeffector junction distribution, pointing to potential neural substrates for cardiac arrhythmia. The pathophysiological alterations in sympathetic function of border zone nerve sprouts led us to initiate further mechanistic studies of how altered neural patterning fundamentally affects cardiac electrophysiology. Overall, this dissertation establishes a synergistic framework for examining structure-function relationships after MI with microscopic precision, which has potential to advance understanding of arrhythmogenic mechanisms.

The dissertation of Ching Zhu is approved.

Kristina Bostrom

Takako Makita

James N. Weiss

Kalyanam Shivkumar, Committee Chair

University of California, Los Angeles

2022

DEDICATION

This work is dedicated to

Robert G. Gourdie and Andrew W. Hunter, who taught me to think

and to

my family – Baby Faye, Peter, Mom, Dad – who taught me to love.

TABLE OF CONTENTS

LIST OF FIGURES

LIST OF TABLES

LIST OF ACRONYMS

AF	Atrial fibrillation
ANS	Autonomic nervous system
APD	Action Potential Duration
AVN	Atrioventricular node
CSD	Cardiac sympathetic denervation
GP	Ganglionated plexus
HR	Heart rate
ICNS	Intrinsic cardiac nervous system
LV	Left ventricle
iDISCO	Immunolabeling-enabled three-Dimensional Imaging of Solvent-Cleared Organs
RDN	Renal artery denervation
SCS	Spinal cord stimulation
SG	Stellate ganglion/ganglia
TEA	Thoracic epidural anesthesia
TH	Tyrosine hydroxylase
VNS	Vagal nerve stimulation

SUPPLEMENTARY MATERIALS

Supplementary Video 1. Dense scar with surviving myocytes mostly on endocardial side. Cleared heart showing 3-dimensional dense scar structure. In addition to excluding structural data from dense scar regions, we also excluded optical mapping data, as most of the surviving myocytes in this region were on the endocardial surface and thus not contiguous with the epicardial shell we used for our quantitative analyses. TH = tyrosine hydroxylase, NFH = neurofilament heavy (1:200, Sigma-Aldrich, AB5539).

PREFACE

Chapter 1. A version of this manuscript is published: Zhu C, Hanna P, Rajendran PS, Shivkumar K. Neuromodulation for Ventricular Tachycardia and Atrial Fibrillation: A Clinical Scenario-Based Review. JACC Clin Electrophysiol. 2019 Aug;5(8):881– 96.

Chapters 2-3. Zhu C, Rajendran P, Hanna P, Efimov I, Salama G, Fowlkes C, Shivkumar K. High-Resolution Structure-Function Mapping of Intact Hearts Reveals Altered Sympathetic Control of Infarct Border Zones. JCI Insight. 2022 Feb; 7(3):e153913.

This work was supported by the National Institutes of Health through the Common Fund’s Stimulating Peripheral Activity to Relieve Conditions (SPARC) program, Grants OT2 OD023848 (PI: K. Shivkumar) and NHLBI Postdoctoral Fellowship T32 HL007895, awarded to the Division of Cardiology, University of California, Los Angeles.

VITA

EDUCATION

Harvard University..09/2005-06/2009
AB in Biochemical Sciences *cum laude*

Stanford University School of Medicine 08/2010-05/2014
MD

POSTGRADUATE CLINICAL TRAINING

Beth Israel Deaconess Medical Center, Harvard Medical School.........06/2014-06/2016
Internal Medicine Internship and Residency

University of California, Los Angeles...07/2016-06/2022
General Cardiology Fellowship

SELECTED PEER-REVIEWED JOURNAL ARTICLES/ABSTRACTS

1. **Zhu C,** Rajendran P, Hanna P, Efimov I, Salama G, Fowlkes C, Shivkumar K. High-Resolution Structure-Function Mapping of Intact Hearts Reveals Altered Sympathetic Control of Infarct Border Zones. JCI Insight. 2022 Feb; 7(3):e153913.
2. **Zhu C**, Hanna P, Rajendran PS, Shivkumar K. Neuromodulation for Ventricular Tachycardia and Atrial Fibrillation: A Clinical Scenario-Based Review. JACC Clin Electrophysiol. 2019 Aug;5(8):881– 96.
3. **Zhu C**, Barker RJ, Hunter AW, Zhang Y, Jourdan J, Gourdie RG. Quantitative analysis of ZO-1 colocalization with Cx43 gap junction plaques in cultures of rat neonatal cardiomyocytes. Microsc Microanal. 2005 Jun;11(3):244–8.
4. Yao J, Ma F, Zhang L, **Zhu C**, Jumabay M, Yao Z, et al. Single-cell RNA-seq Identifies Dynamic Cardiac Transition Program from Adipose Derived Cells Induced by Leukemia Inhibitory Factor. *In Revision*.
5. Mori S, Hanna P, Dacey MJ, Temma T, Hadaya J, **Zhu C**, et al. Comprehensive Anatomy of the Pericardial Space and the Cardiac Hilum: Anatomical Dissections With Intact Pericardium. JACC Cardiovasc Imaging. 2021 Jun 9;S1936-878X(21)00361-2.
6. Hanna P, **Zhu C,** Shivkumar K, Buch B. Cryoballoon pulmonary vein isolation: Effects on neural control of the heart. Int J Cardiol. 2020 Sep 1;314:77-78.
7. Rajendran PS, Hanna P, **Zhu C**, Shivkumar K. Neuroinflammation as a mechanism for cardiovascular diseases. Int J Cardiol. 2019 Aug 1;288:128–9.
8. Hanna P, **Zhu C**, Rajendran PS, Shivkumar K. Anesthetizing the Fibrillating Heart. J Am Heart Assoc. 2019 May 21;8(10):e012713.
9. Dusi V, **Zhu C**, Ajijola OA. Neuromodulation Approaches for Cardiac Arrhythmias: Recent Advances. Curr Cardiol Rep. 2019 Mar 18;21(5):32.
10. Gourdie RG, Ghatnekar GS, O'Quinn M, Rhett MJ, Barker RJ, **Zhu C**, et al. The unstoppable connexin43 carboxyl-terminus: new roles in gap junction organization and wound healing. Ann N Y Acad Sci. 2006 Oct;1080:49–62.
11. Hunter AW, Barker RJ, **Zhu C**, Gourdie RG. Zonula occludens-1 alters connexin43 gap junction size and organization by influencing channel accretion. Mol Biol Cell. 2005 Dec;16(12):5686–98.

HONORS AND AWARDS

Second Prize in Biochemistry, Intel International Science and Engineering Fair, 2005. Received scholarship and Minor Planet #21827 was named “Chingzhu” by MIT Lincoln Laboratory

First Prize in Undergraduate Oral Presentation, Medical University of South Carolina Student Research Day, 2004 and 2006

Outstanding Student Research Award in Academic Pediatrics, Society for Pediatric Research, 05/2007.

Tibor Fabian Award, Tibor Fabian Awards Committee at UCLA, 2018-2022. For achievements as a physician-scientist in cardiovascular research.

Chief Cardiology Fellow, UCLA, 2020-2021

Young Investigator Award, Cardiac Electrophysiology Society, 05/2022

Fellow with Highest-Scoring Abstract Award, Heart Rhythm Society, 05/2022

EDITORIAL EXPERIENCE

The Harvard Science Review, Associate Editor, 2005-2007

Journal of Cardiovascular Electrophysiology, Peer Reviewer, 2019-present

JACC Cardiac Electrophysiology, Peer Reviewer, 2020-present

Cardiovascular Research, Peer Reviewer, 2021-present

Chapter 1:

Neuromodulation in cardiac arrhythmias

Introduction

The autonomic nervous system provides beat-to-beat control of cardiac function over an individual's entire lifetime. The two canonical limbs of the nervous system, sympathetic and parasympathetic, exist in a fine balance in normal physiological states (1). Cardiac disease profoundly alters this balance, causing sympathoexcitation and concomitant reduction in parasympathetic drive that are adaptive in the short term but become maladaptive in the long term if left unchecked (2).

Cardiac responses to internal and external stimuli are controlled by autonomic neural structures which can be divided into three main levels (Figure 1): i) brainstem and spinal cord; ii) extracardiac-intrathoracic ganglia; and iii) intrinsic cardiac nervous system (ICNS) (1, 2). Comprehensive details of the anatomy and functional interplay between these levels are provided in several recent reviews (2–5), and only a general description is provided here to establish a relevant framework for this clinical review.

The cardiac motor neurons, termed efferent neurons, are divided according to their roles in either sympathetic or parasympathetic signaling. Sympathetic efferent preganglionic neurons have cell bodies in the intermediolateral column of the spinal cord and project axons onto postganglionic sympathetic neurons, which are organized into the extracardiac-intrathoracic ganglia, including the middle cervical ganglia (MCG), stellate ganglia (SG, a fusion of the C8 and T1 ganglia), T2-T4 of the paravertebral sympathetic chain ganglia, and mediastinal ganglia. These postganglionic neurons then project via cardiopulmonary nerves to atrial and ventricular myocardium and intrinsic cardiac neurons (6). Preganglionic efferent neurons of the parasympathetic system are located within the brainstem and project axons which travel via the vagus nerve and its branches to postganglionic neurons within the ICNS (1). Cardiac sensory neurons, or afferent neurons, have cell bodies in the nodose and dorsal root ganglia and carry information from the heart to the brainstem and spinal cord. This sensory information is processed at multiple levels in complex feedback loops, which control sympathetic and parasympathetic efferent signals to maintain rhythm and circulation in the face of acute and chronic stressors (7). Finally, the ICNS itself (often referred to as the “little brain on the heart”) is organized into ganglionated plexi (GPs) with efferent and afferent neurons, which not only relay central signals but also form local reflexive circuits to independently regulate regional cardiac electrical, mechanical, and metabolic responses (8). Importantly, these ICNS neurons remain intact even when the heart is excised, and thus a transplanted heart comes with its own “little brain”.

Autonomic reflexes are a major pathophysiological driver of cardiac arrhythmias. Reduced cardiac output in disease states triggers acute baroreceptor reflexes, inflammatory pathways and neuronal remodeling, which increase sympathetic output and decrease parasympathetic signaling (9). At the level of the heart itself, the ICNS is also thought to process local sensory information and increase sympathetic outflow in a cardio-cardiac reflex (10, 11). The consequent electrophysiologic responses coincide with arrhythmic susceptibility (12, 13).

All three levels of the cardiac neuraxis undergo significant adverse remodeling in cardiac disease. In myocardial infarction (MI), for example, the ICNS undergoes denervation followed by nerve sprouting (attempted regeneration) at the peri-infarct zone, which is thought to contribute to regional heterogeneity in sympathetic response and repolarization dispersion leading to ventricular tachycardia/fibrillation (VT/VF) (14–

16). At the extracardiac-intrathoracic level, SG from humans with ischemic and non-ischemic cardiomyopathy have shown neuronal inflammatory changes and glial activation (17, 18). Additionally, neuronal injury has been reported in the brainstem and spinal cord in human and animal models of heart failure (HF) (19–21).

Over the last few decades, substantial evidence has accumulated supporting the association between autonomic imbalance and cardiac arrhythmias. Emerging data has shown that both the sympathetic and parasympathetic limbs of the autonomic nervous system can be leveraged for arrhythmia control (Figure 2). In this review, we describe the current state of neuromodulatory approaches for arrhythmia management, placing each technique in the context of its clinical application.

Acute Management of Electrical Storm

Clinical Scenario

A 78-year-old man with ischemic cardiomyopathy and chronic HF with severely reduced ejection fraction (EF) presented to the emergency department for nearly 160 ICD shocks. After admission, his ICD continued to fire multiple times for incessant VT, exhausting the battery. The patient required emergent sedation/intubation as well as continuous intravenous procainamide infusion to stabilize his rhythm. This was his third hospitalization for electrical storm (ES) in the past two months, having previously failed medical therapy (metoprolol and amiodarone) and multiple catheter ablations. Cardiac sympathetic denervation (CSD) had also been attempted previously but had to be aborted due to extensive pleural adhesions. After extensive discussion, a mutual decision was made with the patient to pursue a trial of percutaneous left stellate ganglion blockade (SGB). The patient tolerated the SGB well without complications, and procainamide was stopped. Six weeks later, he was readmitted for another appropriate ICD shock and underwent repeat left SGB with success. He was subsequently scheduled for outpatient left SGB every 4 weeks and now remains free of sustained VT/VF, 11 months after his first SGB procedure.

Beta-Adrenergic Blockade

Sympathetic overactivity is a fundamental driver of ES (22) and is further exacerbated by pain and distress from ICD shocks. Thus, sedation and mechanical ventilation are often utilized in patients with ES for minimizing pain, as well as for their ability to blunt autonomic reflexes (23–25). Similarly, because beta blockers also dampen sympathoexcitation, they have become a mainstay in the management of recurrent VT/VF and ES (26, 27). Their therapeutic mechanisms have been extensively studied – blockade of the beta-adrenergic G-protein coupled receptors inhibits downstream proarrhythmic changes to cardiac ion channel currents (28–30). Yet we may need to revisit some fundamental mechanisms of their antiarrhythmic effects.

The comparative effects of different beta blockers on ventricular arrhythmogenesis has been in the literature for decades (31, 32). Clinically, these differential effects were first demonstrated in a 2012 study, which found metoprolol to be significantly less effective than propranolol and nadolol for suppressing arrhythmias in patients with long QT syndrome (LQTS) types 1 and 2 (33). More recent data from Chatzidou et al. comparing the non-selective propranolol and the beta-1-selective metoprolol in the acute management of ES in HF (34) has helped to renew interest in the basic science of sympathetic activity in cardiovascular disease. The study found that patients treated with oral propranolol and IV amiodarone had a shorter length of stay with significantly reduced (2.67 times decrease) arrhythmic burden compared with those treated with oral metoprolol and amiodarone. The authors cite the selective downregulation of beta-1 adrenergic receptors over beta-2 receptors in HF, as well as propranolol's sodium channel blockade and central nervous system effects, as underlying mechanisms for their findings.

While this small-scale study suggests that the non-selective effects of propranolol may make it superior to metoprolol in acute management of ES, it remains unclear how non-selective beta blockade will fare beyond the acute phase. Indeed, up to a half of patients with ES, as in our preceding clinical scenario, will continue to have VT/VF despite antiarrhythmic drugs and guideline-directed beta blockade (35). As the propranolol versus metoprolol trial illustrates, the science behind even workhorse drugs like beta blockers cannot be taken for granted, and the widespread success of beta blockers still leaves significant room for improvement in neuromodulation for ES.

Stellate Ganglion Blockade and Thoracic Epidural Anesthesia

Blockade of the SG using percutaneous local anesthetic injection was first performed in 1934 (36) for the treatment of chronic pain syndromes. The procedure can be safely done at bedside with contrast fluoroscopy for anatomic guidance, though ultrasound guidance has also been successfully used (37), as well as pulsed radiofrequency in place of local anesthetic (38). In small human studies, SG blockade has been shown to decrease sympathetically driven cardiac excitability (39–41), likely through reducing both efferent sympathetic signals to, and afferent signals from, the heart. Thoracic epidural anesthesia (TEA) involves percutaneous injection of local anesthetic into the epidural space at the T1-T5 spinal cord and can inhibit efferent and afferent sympathetic influences from both left and right spinal roots (42, 43). TEA has previously been shown to decrease postoperative supraventricular arrhythmias in patients undergoing lung surgery, as well as to relieve anginal pain in ischemic heart disease (44, 45).

In a systematic review of 38 patients with ES who underwent SG blockade, ventricular arrhythmias were significantly reduced in 92% of subjects, from an average of 12 to 1 VT/VF episodes per day (46). A small clinical study of TEA for ES also showed a greater than 80% reduction in ventricular arrhythmias in 6 out of 8 patients (47). Based on the available data, Nademanee et al. has argued that SG blockade and beta blocker therapy may be more effective than the antiarrhythmics previously recommended by the Advanced Cardiac Life Support algorithm for ES (39).

Despite showing promise as temporary measures for stabilization in the acute management of ES, percutaneous SG blockade and TEA have some limitations, and their exact mechanisms of action remain to be elucidated. Both techniques have transient effects due to the inherent pharmacokinetics of local anesthetics. Additionally, the effect of SG blockade can be operator dependent, and the procedure lacks specificity for the heart (48), potentially dampening sympathetic tone to the head, neck, and diaphragm (which restricts its concurrent application to both the left and right sides). More permanent and cardiac-specific modes of disrupting sympathetic signaling are discussed in the following sections.

Inherited Primary Arrhythmia Syndromes

Clinical Scenario

A 24-year-old woman with no prior medical problems was referred to clinic for palpitations and two episodes of syncope after swimming. She was adopted, with unknown biological family history. Her ECG revealed a QTc interval of 612 milliseconds, with broad T waves consistent with LQTS type 1. Outpatient cardiac monitoring also revealed multiple runs of polymorphic VT.

The patient underwent successful ICD implantation and was started on nadolol. Genetic testing revealed the KCNQ1 mutation Q357R, confirming LQTS1. There were no tachytherapies from her ICD for the first 8 months after implantation, however she subsequently enrolled in graduate school and experienced 22 shocks over a 90-minute period. Verapamil was added, but after six weeks she was hospitalized again for numerous appropriate ICD shocks. She underwent left-sided CSD (LCSD) without complications. Over a 16-month follow-up period, she remained free of sustained VT and tachytherapies on device interrogations, and verapamil was tapered off.

Cardiac Sympathetic Denervation

Pioneered more than 100 years ago for the treatment of angina, CSD has had a recent resurgence in interest for the management of arrhythmia (49). After a long period of being overshadowed by modern pharmacological advances, LCSD re-emerged in clinical practice in 1961 as a therapy for medication-refractory VT (50, 51) and subsequently, for congenital LQTS (48, 52) as well as catecholaminergic polymorphic ventricular tachycardia (CPVT) (53, 54).

Both left-sided and bilateral CSD (BCSD) are typically performed via video-assisted thoracoscopic surgery (VATS) and involves removal of the lower half of the SG as well as the T2-T4 ganglia of the thoracic sympathetic chain (Figure 3). LCSD can usually be done in 40 minutes (and BCSD, in 120 minutes), and significantly reduces, but does not completely abolish, both efferent sympathetic and afferent neurotransmission to and from the heart, respectively (55). As the upper half of the SG and the MCG remain intact after the procedure, some efferent sympathetic innervation is preserved to mitigate the adverse off-target effects of total stellectomy (55). Though LCSD is traditionally used for inherited primary arrhythmia syndromes, the significant contribution of right-sided sympathetic nerves to ventricular arrhythmogenesis (detailed in the next section) has long been known (56) and confirmed in more recent work (57, 58).

At present, LQTS is the inherited primary arrhythmia in which LCSD has been best studied. The largest trial of LCSD for LQTS included 147 patients who were particular high-risk: they had very prolonged QT intervals (mean QTc 543ms), 48% had a prior cardiac arrest, 99% were symptomatic, and 75% of those on full-dose beta-blocker therapy remained symptomatic (59). During an 8-year follow-up after undergoing LCSD, cardiac events in these patients decreased by 91% and, in those with ES who had experienced multiple ICD shocks, the median number of ICD shocks decreased by 95%. Genotyping was performed for 51 patients in this study and showed that LCSD was more effective in LQT1 and LQT3 patients, consistent with the fact that the LQT1 mutation is in I_{Ks}, a delayed-rectifier potassium channel particularly sensitive to sympathetic stimulation (60, 61). The impressive, though incomplete, effect of LCSD supports the Class IIa recommendation for its use to improve quality of life for LQTS patients with refractory syncope and multiple ICD shocks despite beta-blocker therapy (62, 63).

The impact of LCSD on quality of life is also an especially important consideration in young patients with CPVT (64, 65). For these patients the risk of ES is particularly high as the distress and catecholamine release from a first ICD shock often initiates a vicious cycle of recurrent VT/VF and multiple subsequent shocks. The first study of LCSD efficacy in CPVT followed three patients, all with recurrent syncope and multiple ICD shocks despite beta blocker therapy, and it showed a complete suppression of symptoms for more than 10 years after LCSD (53). Subsequent larger studies have also shown LCSD to reduce major cardiac events and ICD shocks by 89-93% (66, 67). There were no significant complications reported in these studies, though transient Horner's syndrome was reported in a small number of patients (11%). These data suggest that for patients with primary inherited arrhythmias in whom the first-line therapy of beta blockade is incompletely effective, LCSD should be considered, perhaps even before implantation of an ICD (54).

Structural Heart Disease

Clinical Scenario

A 16-year-old male with no past medical history presented to the emergency department with palpitations after running, and was found to be in monomorphic VT. He was diagnosed with arrhythmogenic right ventricular cardiomyopathy (ARVC) based on T wave inversions in V1-V4, left-bundle inferior-axis VT, a sibling who died suddenly in his early 20s while exercising, and subtricuspid right ventricular dyskinesia with right ventricular EF of 30%. Genetic testing revealed a pathogenic c.2489+1G>A splice donor variant in the desmosomal gene *PKP2*.

The patient received a dual-chamber ICD and was discharged on metoprolol. Over the next few months, he was hospitalized numerous times for frequent appropriate ICD shocks while exercising and subsequently underwent two endocardial/epicardial ablations, as well as initiation of amiodarone, without success. The patient underwent bilateral CSD (BCSD) without complications. At one-year follow-up, the patient remained asymptomatic on metoprolol, and routine device interrogations showed no VT therapies.

Bilateral Cardiac Sympathetic Denervation

The safety and success of LCSD in inherited primary arrhythmias has led to the expansion of its use to structural heart disease (SHD). However, the initial case series describing LCSD for refractory VT/VF storm in patients with SHD showed that only 5 out of 9 patients benefited from the procedure (47). Interestingly, the patients in the study who underwent TEA, which affects both left- and right-sided sympathetic cardiac innervation, showed a greater response, with 75% having a greater than 80% reduction in their ventricular arrhythmia burden. These results raised the question of whether, for SHD, bilateral cardiac sympathectomy may be more effective than LCSD alone.

The anatomical contribution of both left (LSG) and right stellate ganglia (RSG) to sympathetic innervation of the left ventricle has been described since the 1960s (68), with canine models showing predominant RSG innervation of the anterior aspects of the ventricles while the LSG predominated the posterior aspects, though both SGs provide some innervation to all aspects of the ventricles. In the case of ARVC, abnormal sympathetic innervation of the right ventricle has been described since the disease was first reported (69). What remains unclear is the distinct functional effect of the RSG versus the LSG at the ventricular level. Conflicting studies have shown either no change in the refractory period of the anterior left ventricular wall with RSG stimulation, or a paradoxical decrease in ventricular refractory period with RSG removal (70–72). A more recent study in a porcine model by Vaseghi and colleagues found that innervation of the anterior left ventricular wall and effect on repolarization is shared by the bilateral SGs, though LSG stimulation may be more proarrhythmic by increasing dispersion of the refractory period across the ventricular wall (57).

While the precise role of the RSG in arrhythmogenesis remains to be elucidated, a 2017 retrospective analysis suggested that BCSD may be more effective for treatment for VT in SHD than LCSD alone (73). In this study, 121 patients with SHD (mostly non-ischemic etiologies) underwent either LCSD (19%) or BCSD (81%) for refractory VT or VT storm. In these patients, LCSD was always performed first, in case BCSD could not be tolerated due to hemodynamic instability. Over a median follow-up period of 1.1 years, those who underwent BCSD had significantly longer ICD-shock-free and transplant-free survival compared to those who underwent LCSD only, though the overall endpoints of recurrent ICD shocks and freedom from sustained VT were similar. Thus far, this has been the largest series of patients with predominantly structural heart disease undergoing CSD for refractory VT. Further, the Cardiac Sympathetic Denervation for Prevention of Ventricular Tachyarrhythmias (PREVENT VT) trial (74) has been planned to investigate the antiarrhythmic effects of BCSD.

Though significant preclinical and retrospective data have supported promising roles for LCSD and BCSD in the management of refractory VT, the efficacy of these relatively invasive procedures remains incomplete. Thus, efforts toward successful antiarrhythmic neuromodulation in SHD are being expanded to other limbs of the cardiac autonomic nervous system, which are discussed in the following sections.

Renal Artery Denervation

The effects of modulating renal sympathetic innervation have long been studied, from the experiments of Claude Bernard and Ernest Starling in the late 19th century (75, 76) to more recent work on its potential in treating hypertension (77, 78). Renal artery sympathetic fibers run parallel to the artery ostially to distally in the adventitial layer. Renal artery denervation (RDN) is performed via selective angiography and catheter ablation (Figure 4) and is aimed at inhibiting the afferent renal sympathetic pathway, which in turn decreases efferent sympathetic influence on the heart (79).

RDN has been shown to decrease VT/VF burden in a porcine postinfarct model (80) and in small human studies. In a 2015 observational study of 10 patients who underwent RDN for refractory VT/VF, ventricular arrhythmias and ICD shocks were both reduced from 28.5 and 8 episodes in the 6 months before RDN to 0 and 0 episodes over the 6 months after RDN, respectively (81). Another retrospective study of 32 patients showed that in those who underwent catheter ablation of VT plus adjunctive RDN, the number of VT/VF episodes as well as ICD shocks and anti-tachycardia pacing decreased significantly when compared to ablation alone, though mortality rates were similar in the two arms (82).

While RDN has not been compared directly to LCSD or BCSD for VT/VF treatment, its advantages include avoidance of thoracotomy, as well as potential to suppress reflexive sympathetic signaling from sources other than the bottom half of the SG (i.e. top half of SG, MCG, and circulating catecholamines). Recent data has suggested RDN may be considered as adjunctive therapy to CSD for ablation-refractory cases of VT/VF (83, 84). The small amount of data on RDN as antiarrhythmic therapy, including a recent trial on its use for atrial fibrillation (AF) (85), shows promise, but the procedure has yielded mixed results in its trials for hypertension treatment, likely due to inconsistent degrees of technical success and suboptimal anatomical targets (77). These challenges must be overcome if RDN is to be effectively applied to the treatment of ventricular arrhythmias.

Spinal Cord Stimulation

Relatively accessible anatomic location, as well as previously demonstrated safety and efficacy in treating angina and chronic pain (86, 87), have made thoracic spinal cord stimulation (SCS) a potential therapy for ventricular arrhythmias in SHD. SCS is achieved by inserting one or two leads with eight electrodes into the epidural space at the thoracic level (either at T1-T3 or T2-T4) and applying a small current at approximately the paresthesia threshold. Prior canine and porcine studies showed significant reduction in ischemia driven ventricular arrhythmias, even with brief (approximately 1-hour) periods of SCS (88–90). The spinal cord is where multiple tracts of the cardiac ANS converge, but the specific beneficial mechanisms underlying SCS remain poorly understood and may relate to both decreased sympathetic outflow and increased vagal tone (88, 91–94).

At present, data on SCS and ventricular arrhythmias in humans are limited to case series and small clinical trials. In 2012, a case series of two patients who underwent SCS showed reduced VT burden, from 128 and 90 episodes of VT over 2 months before SCS, to 6 and 0 episodes over 2 months after SCS (95). Two randomized trials primarily evaluating the effect of SCS in HF have had conflicting results and either failed or had insufficient power to show significant effect on ventricular arrhythmia burden. The SCS HEART study (96) showed significant HF symptom reduction and LVEF improvement in 17 patients after SCS, however the DEFEAT-HF study (97) did not show improved clinical outcomes for 66 patients who underwent SCS. There was also no significant reduction in ventricular arrhythmias based on limited data from ICD interrogations in DEFEAT-HF. The conflicting results could possibly be explained by the different anatomical locations (T1-T3 in SCS HEART, versus T2-T4 in DEFEAT-HF) of the electrodes in the thoracic spinal cord, and/or by the different stimulation parameters (12 hours per day via implanted stimulator in DEFEAT-HF versus continuously for SCS HEART). If SCS is to have reproducible success as antiarrhythmic therapy, future studies will need to investigate the distinct neurohormonal and electrophysiological effects of varying anatomical locations and stimulation protocols.

Vagal Nerve Stimulation

While increased sympathetic tone, the main target of the aforementioned neuromodulatory therapies, is arrhythmogenic, increased parasympathetic tone is thought to be cardioprotective in SHD – maintaining electrical stability via preservation of gap junction communication between myocytes, reducing heterogeneity of action potential duration, and decreasing circulating catecholamines and inflammatory markers (98–100). Clinically, augmenting parasympathetic tone to terminate VT was demonstrated as early as 1977 (101). This provides the mechanistic basis for investigating the effect of vagal nerve stimulation (VNS) on ventricular arrhythmias. VNS is achieved via surgical implantation of a pulse generator powering a cuff electrode around the vagus nerve. Left sided VNS has already been in clinical use for drug-refractory epilepsy (102) and depression (103). Initial feasibility studies for right-sided VNS in the treatment of HF yielded promising data for safety, tolerability, and preliminary efficacy (104).

In animal models, VNS has been shown to significantly reduce VT/VF occurrence and inducibility after coronary artery occlusion and reperfusion (105) and healed myocardial infarction (106), likely by decreasing heterogeneity of repolarization and stabilizing infarct border zones (107–109). Interestingly, adjustments in the frequency, pulse width, and current used for VNS changes the balance between increased efferent parasympathetic output and afferent inhibition of parasympathetic output (110). This suggests that VNS does not simply turn on parasympathetic input to the heart like a bimodal switch. There may be optimal parameters to achieve a therapeutic effect - a “neural fulcrum” at which the reflexive afferent decrease in central parasympathetic drive is counterbalanced by direct efferent increase in vagal parasympathetic outflow (111). Variable effects from altering stimulation parameters likely explains the conflicting results obtained from recent clinical trials of VNS for chronic HF (112–114), reviewed comprehensively elsewhere (115, 116), which utilized different VNS frequencies and pulse amplitudes. This more nuanced understanding of vagal stimulation parameters led to a 2018 study of preferentially efferent VNS in pigs with chronic MI after BCSD (117). After BCSD, VT was inducible in all infarcted animals during isoproterenol infusion, but VNS reduced this inducibility by 67%.

A disadvantage of cervical VNS is its invasiveness, and side effects such as voice changes, discomfort at implant site and infection have been described (118). A noninvasive alternative to cervical VNS, tragus nerve stimulation (TNS), is also being studied for VT/VF. TNS targets the cutaneous, auricular branch of the vagus nerve at the tragus. In a canine post-MI model, chronic intermittent TNS lasting 2 hours per day for 2 months reduced inducibility of ventricular arrhythmias, LSG neuronal activity, as well as nerve remodeling at the infarct border zone (119). A recent human study of TNS in 128 patients applied the treatment for 2 hours to patients with ST-elevation MI undergoing percutaneous coronary reperfusion (120). The incidence of VT/VF during the first 24 hours after reperfusion, as well as infarct size and inflammatory markers, was significantly reduced in those who underwent TNS compared to sham intervention. Though there has been progress in utilizing stimulation of the vagus nerve and its auricular branch, achieving convincing clinical benefit will require future studies to better incorporate our evolving understanding of the basic mechanisms underlying the “neural fulcrum”.

Atrial Fibrillation

Clinical Scenario

A 68-year-old man with severe rheumatic mitral regurgitation, chronic HF with preserved EF, and chronic persistent AF on amiodarone undergoes mitral valve replacement surgery with maze procedure and left atrial appendage exclusion. After completion of these main procedures, the patient was in normal sinus rhythm. Using a decapolar coronary sinus catheter, electrical isolation of the pulmonary veins (PVs) was confirmed with epicardial electrograms demonstrating conduction block. Subsequently, the four major epicardial fat pads known to contain intrinsic cardiac GPs were located: anterior to the right superior PV, infero-posterior to the right inferior PV, anterior to the left superior PV and left inferior PV (between the PVs and LAA), and infer-posterior to the left inferior PV. Botulinum toxin was injected into each of these fat pads, and the surgery was concluded.

The patient had an uncomplicated recovery. Three months later, he reported his exercise tolerance was significantly improved and ambulatory ECG monitoring was negative for recurrent AF. His amiodarone was subsequently stopped and, over 15 months of additional follow-up, multiple two-week event monitors have shown no recurrent AF.

Pulmonary Vein Isolation and the Intrinsic Cardiac Nervous System

Parasympathetic signaling has long been implicated in the pathogenesis of certain forms of AF (121). High-level vagal stimulation or the administration of cholinergic agonists lead to inducibility of sustained AF (122–124) via spatially heterogenous shortening of atrial refractoriness (125, 126) and shortening of atrial propagation wavelength (127). Vagal signaling to the heart is thought to be relayed by the GPs of the ICNS. In canine studies, AF inducibility from vagal stimulation was eliminated after catheter ablation of several atrial fat pads, which contain the GPs conveying information from the vagus nerve to the atria (128, 129). Thus, the intrinsic cardiac GPs are attractive targets for AF therapies (Figure 5), but translating the experimental data to clinical use remains challenging.

Since Haissaguerre et al first demonstrated the success of pulmonary vein isolation (PVI) for catheter ablation of AF, there has been widespread acceptance of the technique and its underlying mechanistic assumption – that PV ectopic foci are triggers of AF (130). Soon after the advent of PVI, it was observed to have autonomic effects, namely bradycardic events (131) and long-term alterations of heart rate variability (132). Given that the anatomical locations of intrinsic cardiac GPs approximately match PVI ablation sites, ICN denervation may play an important role in the efficacy of PVI (133).

Studies of PVI in conjunction with targeted ICN ablation have shown that the procedures may be synergistic. Two randomized trials by Katritsis et al compared PVI alone, ablation at expected anatomical locations of cardiac GPs, and PVI plus GP ablation (134, 135). The combined approach resulted in approximately 1.5-fold higher success rates of eliminating paroxysmal AF. A similar comparison study showed that PVI plus GP ablation was superior to PVI plus linear lesions (136). Surgical case series (137–139) have also described impressive success rates (65-86%) of AF ablation with a combined approach of PVI plus ablation of GPs and the ligament of Marshall (LOM), which serves as a pathway connecting intrathoracic cardiac neurons to the ICN. Percutaneous approaches of targeting the LOM via ethanol infusion in the vein of

Marshall (VOM) have also been validated in humans (140), and a randomized, multicenter trial (VOM-R01) is currently underway to investigate the role of VOM ethanol ablation in persistent AF.

The current clinical approaches to modulate the ICNS lack specificity, as the cardiac GPs contain diverse neuronal populations and neurotransmitter types (141). Thus, GP destruction is a crude approach with variable outcomes, which is readily apparent in the results of two recent trials targeting the ICNS for AF management. The AFACT trial (142) was a study of 240 patients in which patients with paroxysmal AF underwent PVI and those with persistent AF underwent PVI plus additional lines (Dallas lesion set). These patients were then randomized to receive either additional thoracoscopic epicardial ablation of GPs and LOM or no extra ablation. The additional GP and LOM ablation had no significant effect on AF recurrence and actually caused more adverse events such as major bleeding and sinus node dysfunction requiring pacemaker implantation. In contrast, a randomized study of botulinum toxin injection into epicardial fat pads in patients with paroxysmal AF undergoing CABG showed significant reduction in AF burden compared to placebo over a three-year postoperative follow-up period (143). The conflicting results of these trials highlight the profound knowledge gap in how ICNS physiology regulates atrial impulse propagation, which must be addressed to define the role for ICNS modulation in AF therapy.

Vagal Nerve Stimulation for Atrial Arrhythmias

While high-level vagal stimulation has been shown to cause AF inducibility, mild-to-moderate enhancement of vagal efferent activity has been observed to suppress PV firing even without inducing bradycardia (144). This paradox illustrates the complexity of cardiac autonomic pathways, where efferent and afferent signals, as well as central-peripheral nervous system interactions, exist in a delicate balance (111). In animal models, low level VNS (LL-VNS), delivered at stimulation voltages below the threshold of inducing bradycardia, prolonged the atrial and PV effective refractory periods (ERP), shortened AF duration, and suppressed activity of the atrial GPs (145–147). Several mechanisms by which LL-VNS suppresses AF have been proposed, including anti-adrenergic suppression of left SG activity (148) and release of the neurotransmitter vasostatin-1 (149). Interestingly, a recent canine study showed that LL-VNS mitigated inducibility of AF by preferentially targeting neurons of the ICNS which receive both efferent and afferent information, or so-called “convergent” neurons (150).

The antiarrhythmic effects of LL-VNS led to investigation of noninvasive low-level tragus stimulation (LLTS), which was also shown to suppress AF in animal models of rapid atrial pacing (151). In 2015, Stavrakis et al reported the first-in-man data on LLTS in patients with drug-refractory paroxysmal AF who were referred for catheter ablation (152). With only 1 hour of LLTS, right and left atrial ERP were prolonged, AF duration was reduced, and pro-inflammatory markers such as TNF-α and C-reactive protein were decreased. This study has since been expanded to a randomized clinical trial (TREAT AF), with promising preliminary results (153). The voltage threshold at which patient discomfort was reported was also significantly higher than that required to achieve the antiarrhythmic effects, which is encouraging for the potential of LLTS as a non-invasive treatment for paroxysmal AF.

Conclusions

Since the revival of CSD to treat inherited arrhythmia syndromes in the 1960s, significant progress has been made in developing neuromodulatory techniques for heart rhythm disorders. LCSD continues to improve outcomes for those with LQTS and CPVT, and BCSD is now becoming more widely used for its effectiveness in refractory VT/VF cases, especially in patients with SHD. Small clinical studies also have shown that modulation at the spinal cord, vagus, SG, ICNS, as well as distant renal sympathetic nerves can reduce ventricular arrhythmias and atrial fibrillation. But despite these optimistic early results, the efficacy of cardiac neuromodulation clearly needs further study. Case selection for likely responders is limited by our lack of understanding of the cardiac autonomic nervous system, a multilevel hierarchy with complex feedback loops which we are only beginning to unravel.

Some specific questions that still require experimental investigation include:

- What is the mechanism of benefit provided by increasingly used neuromodulatory procedures such as CSD?
- Do patients have differing baseline autonomic states that require individualized therapies toward the optimal sympathovagal balance?
- How can we effectively titrate neuromodulatory therapy using electrical readouts from the heart and/or biomarkers?

Recent advances in neurosciences such as optogenetics have been applied to fundamental questions in electrophysiology and cardiac neural control (154) and could pave the way to valuable clinical insights.

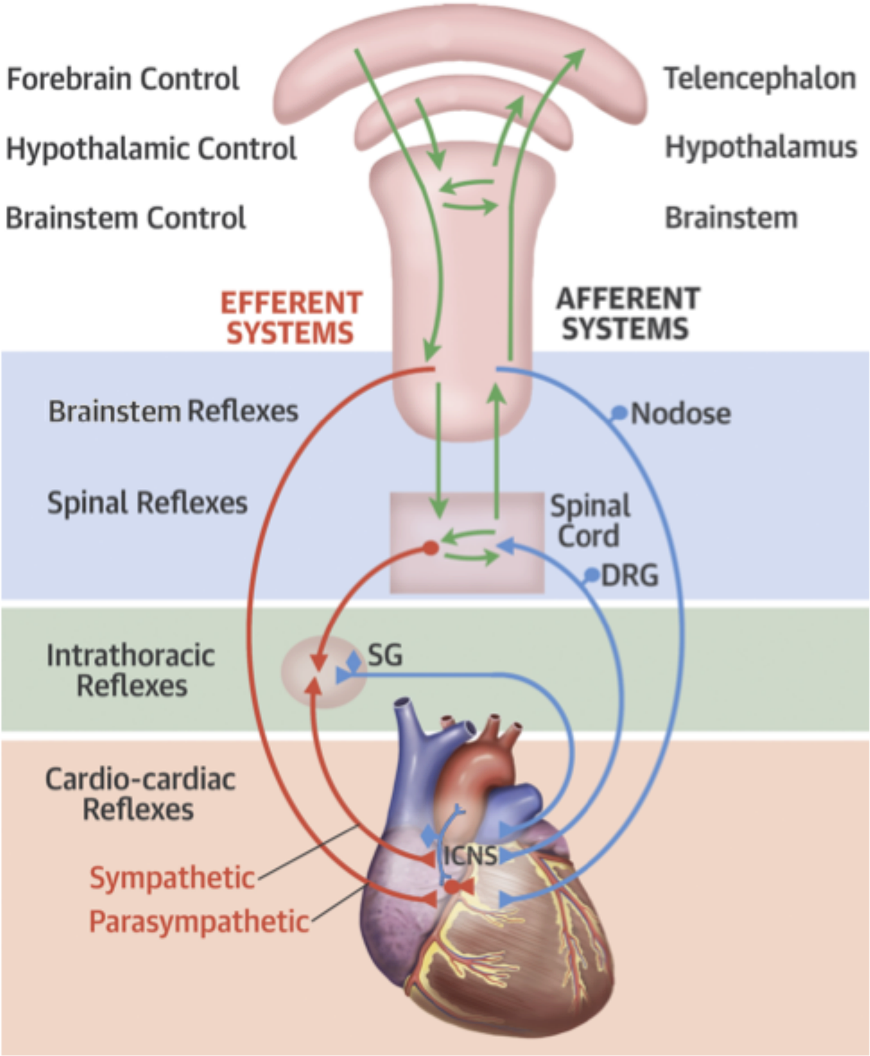

Figure 1. Cardiac Autonomic Control. Autonomic control of the heart consists of numerous, complex reflex loops which can be divided into three main levels: the brainstem spinal cord (blue box), intrathoracic extracardiac ganglia (green box), and the intrinsic cardiac nervous system (tan box). The afferent limb (blue lines) carries sensory information from the heart to higher levels, where it is processed by multiple components of the central nervous system (green lines). The efferent limb (red lines) carries signals from higher levels down to the heart, to modulate cardiac function. SG = stellate ganglion, DRG = dorsal root ganglion, ICNS = intrinsic cardiac nervous system. *Adapted from Goldberger JJ, Arora R, Buckley U, Shivkumar K. Autonomic Nervous*

System Dysfunction: JACC Focus Seminar. J. Am. Coll. Cardiol. 2019;73:1189–1206.

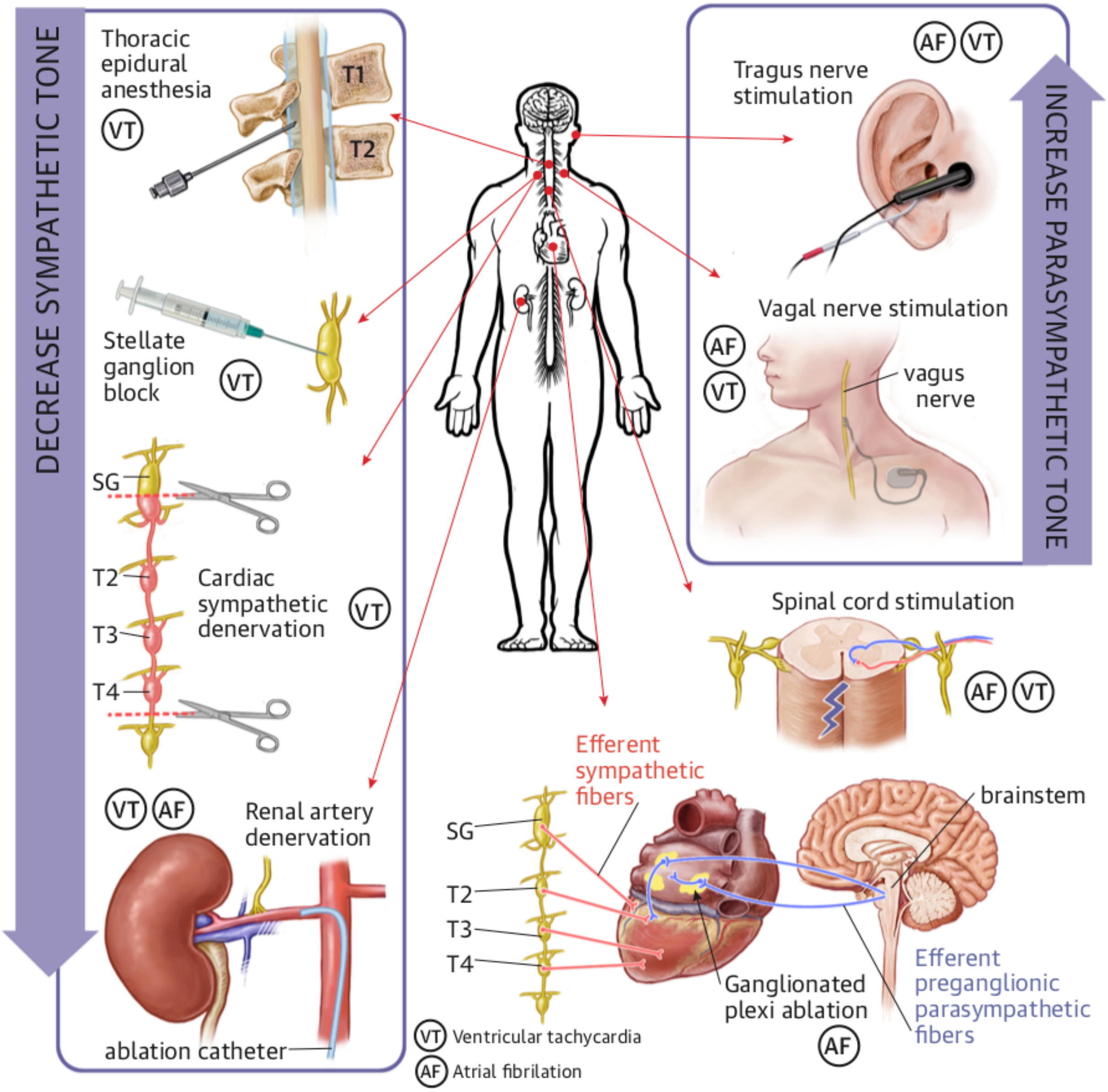

Figure 2. Neuromodulation for Arrhythmias. Neuromodulatory therapies targeting sympathetic and parasympathetic pathways have been applied at multiple levels of the cardiac autonomic nervous system to treat ventricular tachycardia (VT) and atrial fibrillation (AF). TEA = thoracic epidural anesthesia, SGB = stellate ganglion block, CSD = cardiac sympathetic denervation, RDN = renal artery denervation, SCS = spinal cord stimulation, GP = ganglionated plexi, TNS = tragus nerve stimulation, VNS = vagal nerve stimulation, ABVN = auricular branch of the vagus nerve. Afferent nerve fibers

are omitted for simplicity. *Adapted from Krokhaleva Y, Vaseghi M. Update on prevention and treatment of sudden cardiac arrest. Trends Cardiovasc. Med. 2019; https://doi.org/10.1016/j.tcm.2018.11.002.*

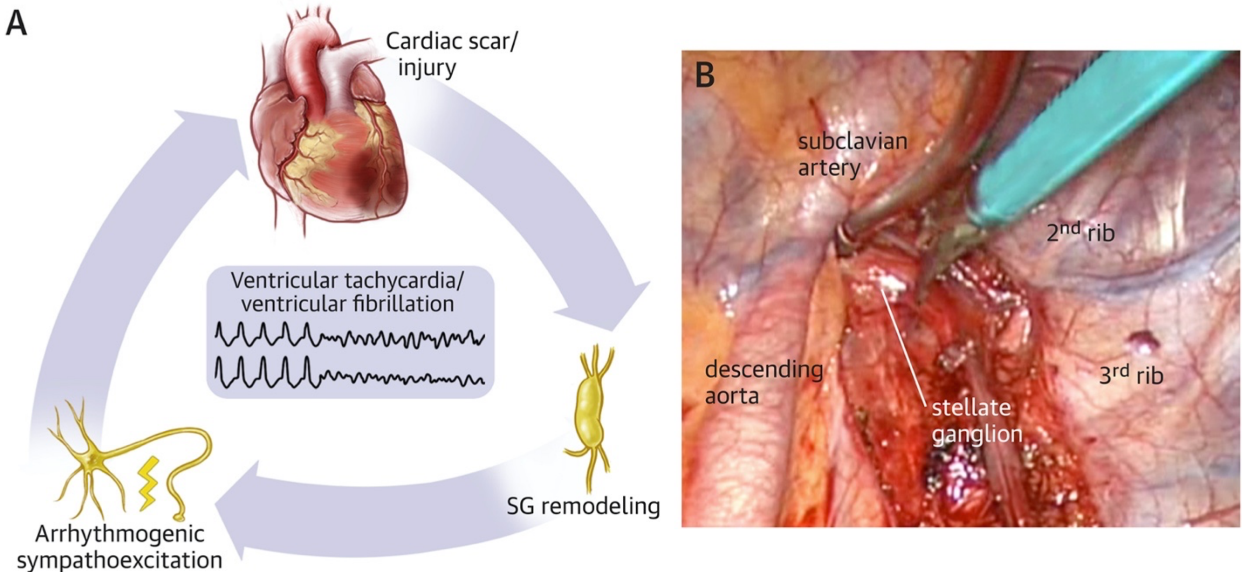

Figure 3. Cardiac Sympathetic Denervation. A) Structural heart diseases lead to remodeling of the stellate ganglia (SG), which causes increased sympathetic outflow leading to arrhythmias. *Adapted from Ajijola OA, Hoover DB, Simerly TM, et al. Inflammation, oxidative stress, and glial cell activation characterize stellate ganglia from humans with electrical storm. JCI Insight 2017;2.* B) Cardiac sympathetic denervation (CSD) is performed by removing the bottom half of the SG and T2-T4 ganglia under thoracoscopic guidance.

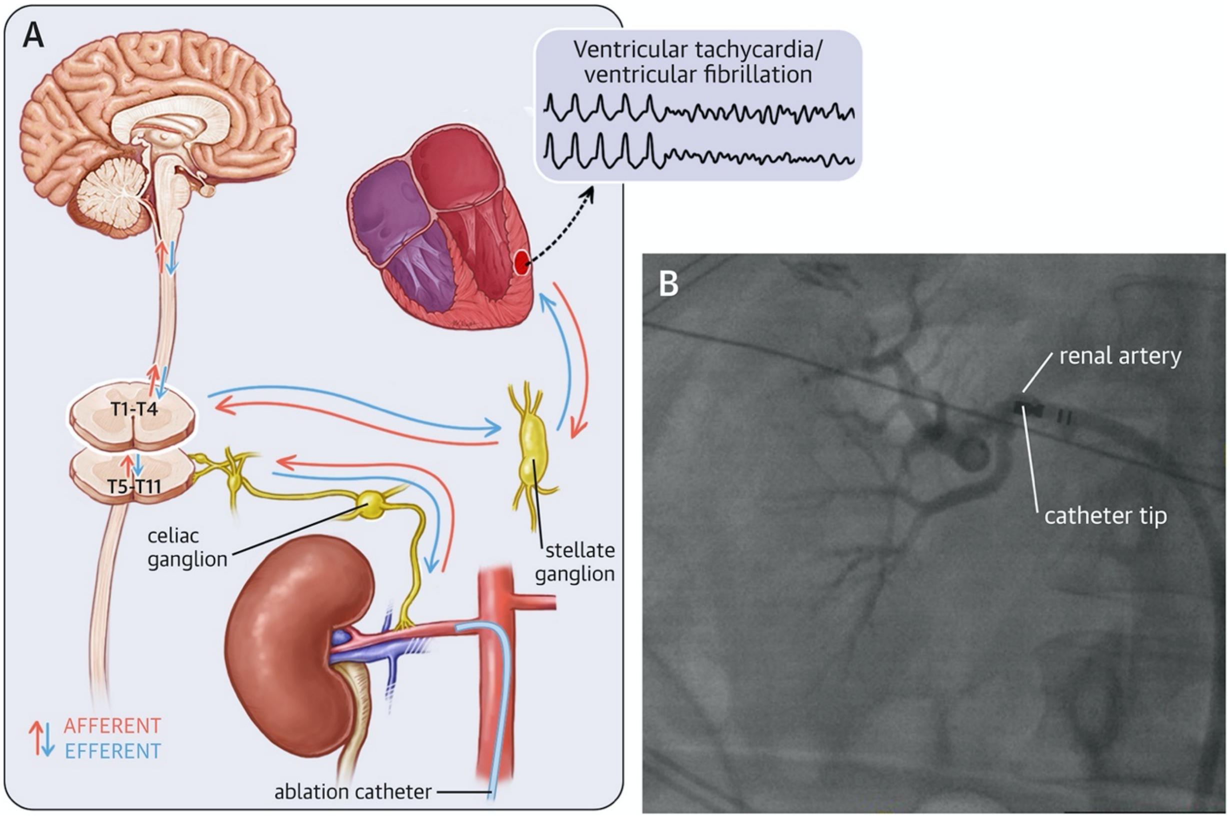

Figure 4. Renal Artery Denervation. A) Renal artery denervation (RDN) exerts its antiarrhythmic effect by decreasing renal afferent signals, which in turn decreases efferent sympathetic outflow to the heart. *Adapted from Bradfield JS, Vaseghi M, Shivkumar K. Renal denervation for refractory ventricular arrhythmias. Trends Cardiovasc. Med. 2014;24:206–213.* B) RDN is performed via catheter ablation under guidance by contrast angiography.

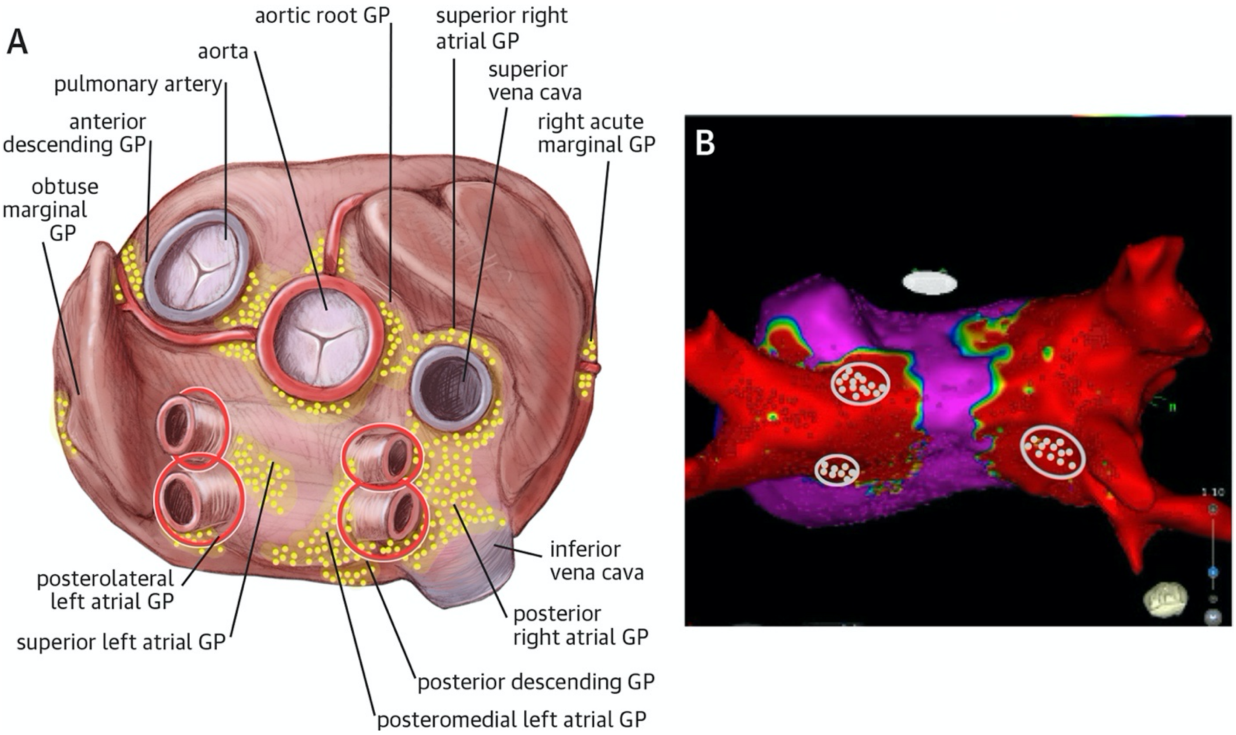

Figure 5. Pulmonary Vein Isolation and the Intrinsic Cardiac Nervous System. A) A dense network of intrinsic cardiac ganglionated plexi (GPs) (yellow dots) correlates anatomically with major cardiac vessels. These GPs also crudely match ablation sites targeted by most pulmonary vein isolation (PVI) techniques (red dotted lines) for atrial fibrillation (AF). *Adapted from Rajendran PS, Chui RW, Ajijola OA, et al. Neural Control of Cardiac Function in Health and Disease. Atlas of Cardiac Innervation 2016:13.* B) Electroanatomic map of pulmonary veins after AF ablation, showing correlation of ablation sites with intrinsic cardiac GPs (encircled gray dots).

References

1. Andresen MC, Kunze DL, Mendelowitz D. Central nervous system regulation of the heart. In: Armour JA, Ardell JL, editors. Basic and Clinical Neurocardiology. New York: Oxford University Press, 2004:187–219.

2. Armour JA. Cardiac neuronal hierarchy in health and disease. Am. J. Physiol. Regul. Integr. Comp. Physiol. 2004;287:R262-271.

3. Ardell JL, Andresen MC, Armour JA, et al. Translational neurocardiology: preclinical models and cardioneural integrative aspects. J. Physiol. 2016;594:3877–3909.

4. Jänig W. Neurocardiology: a neurobiologist's perspective. J. Physiol. 2016;594:3955–3962.

5. Hanna P, Rajendran PS, Ajijola OA, et al. Cardiac neuroanatomy - Imaging nerves to define functional control. Auton. Neurosci. Basic Clin. 2017;207:48–58.

6. Kawashima T. The autonomic nervous system of the human heart with special reference to its origin, course, and peripheral distribution. Anat. Embryol. (Berl.) 2005;209:425–438.

7. Hopkins DA, Armour JA. Ganglionic distribution of afferent neurons innervating the canine heart and cardiopulmonary nerves. J. Auton. Nerv. Syst. 1989;26:213–222.

8. Armour JA. Potential clinical relevance of the "little brain" on the mammalian heart. Exp. Physiol. 2008;93:165–176.

9. Floras JS. Sympathetic nervous system activation in human heart failure: clinical implications of an updated model. J. Am. Coll. Cardiol. 2009;54:375–385.

10. Schwartz PJ, Pagani M, Lombardi F, Malliani A, Brown AM. A cardiocardiac sympathovagal reflex in the cat. Circ. Res. 1973;32:215–220.

11. Wang H-J, Rozanski GJ, Zucker IH. Cardiac sympathetic afferent reflex control of cardiac function in normal and chronic heart failure states. J. Physiol. 2017;595:2519–2534.

12. El-Sherif N. Reentrant ventricular arrhythmias in the late myocardial infarction period. 6. Effect of the autonomic system. Circulation 1978;58:103–110.

13. Priori SG, Mantica M, Schwartz PJ. Delayed afterdepolarizations elicited in vivo by left stellate ganglion stimulation. Circulation 1988;78:178–185.

14. Cao JM, Chen LS, KenKnight BH, et al. Nerve sprouting and sudden cardiac death. Circ. Res. 2000;86:816–821.

15. Rajendran PS, Nakamura K, Ajijola OA, et al. Myocardial infarction induces structural and functional remodelling of the intrinsic cardiac nervous system. J. Physiol. 2016;594:321–341.

16. Vaseghi M, Lux RL, Mahajan A, Shivkumar K. Sympathetic stimulation increases dispersion of repolarization in humans with myocardial infarction. Am. J. Physiol. Heart Circ. Physiol. 2012;302:H1838-1846.

17. Ajijola OA, Wisco JJ, Lambert HW, et al. Extracardiac neural remodeling in humans with cardiomyopathy. Circ. Arrhythm. Electrophysiol. 2012;5:1010–1116.

18. Ajijola OA, Hoover DB, Simerly TM, et al. Inflammation, oxidative stress, and glial cell activation characterize stellate ganglia from humans with electrical storm. JCI Insight 2017;2.

19. Kumar R, Woo MA, Birrer BVX, et al. Mammillary bodies and fornix fibers are injured in heart failure. Neurobiol. Dis. 2009;33:236–242.

20. Woo MA, Macey PM, Keens PT, et al. Aberrant central nervous system responses to the Valsalva maneuver in heart failure. Congest. Heart Fail. Greenwich Conn 2007;13:29–35.
21. Nakamura K, Ajijola OA, Aliotta E, Armour JA, Ardell JL, Shivkumar K. Pathological effects of chronic myocardial infarction on peripheral neurons mediating cardiac neurotransmission. Auton. Neurosci. Basic Clin. 2016;197:34–40.
22. Vaseghi M, Shivkumar K. The Role of the Autonomic Nervous System in Sudden Cardiac Death. Prog. Cardiovasc. Dis. 2008;50:404–419.
23. Geraghty L, Santangeli P, Tedrow UB, Shivkumar K, Kumar S. Contemporary Management of Electrical Storm. Heart Lung Circ. 2019;28:123–133.
24. Mulpuru SK, Patel DV, Wilbur SL, Vasavada BC, Furqan T. Electrical storm and termination with propofol therapy: a case report. Int. J. Cardiol. 2008;128:e6-8.
25. Tsutsui K, Hayami N, Kunishima T, et al. Dexmedetomidine and clonidine inhibit ventricular tachyarrhythmias in a rabbit model of acquired long QT syndrome. Circ. J. Off. J. Jpn. Circ. Soc. 2012;76:2343–2347.
26. Credner SC, Klingenheben T, Mauss O, Sticherling C, Hohnloser SH. Electrical storm in patients with transvenous implantable cardioverter-defibrillators: incidence, management and prognostic implications. J. Am. Coll. Cardiol. 1998;32:1909–1915.
27. European Heart Rhythm Association, Heart Rhythm Society, Zipes DP, et al. ACC/AHA/ESC 2006 guidelines for management of patients with ventricular arrhythmias and the prevention of sudden cardiac death: a report of the American College of Cardiology/American Heart Association Task Force and the European Society of Cardiology Committee for Practice Guidelines (Writing Committee to Develop

Guidelines for Management of Patients With Ventricular Arrhythmias and the Prevention of Sudden Cardiac Death). J. Am. Coll. Cardiol. 2006;48:e247-346.

28. Kowey PR, Friehling TD, Marinchak RA. Electrophysiology of beta blockers in supraventricular arrhythmias. Am. J. Cardiol. 1987;60:32D-38D.

29. Dorian P. Antiarrhythmic action of beta-blockers: potential mechanisms. J. Cardiovasc. Pharmacol. Ther. 2005;10 Suppl 1:S15-22.

30. Bangalore S, Messerli FH, Kostis JB, Pepine CJ. Cardiovascular protection using beta-blockers: a critical review of the evidence. J. Am. Coll. Cardiol. 2007;50:563–572.

31. Anderson JL, Rodier HE, Green LS. Comparative effects of beta-adrenergic blocking drugs on experimental ventricular fibrillation threshold. Am. J. Cardiol. 1983;51:1196–1202.

32. Johansson BW. Effect of beta blockade on ventricular fibrillation- and ventricular tachycardia-induced circulatory arrest in acute myocardial infarction. Am. J. Cardiol. 1986;57:34F-37F.

33. Chockalingam P, Crotti L, Girardengo G, et al. Not all beta-blockers are equal in the management of long QT syndrome types 1 and 2: higher recurrence of events under metoprolol. J. Am. Coll. Cardiol. 2012;60:2092–2099.

34. Chatzidou S, Kontogiannis C, Tsilimigras DI, et al. Propranolol Versus Metoprolol for Treatment of Electrical Storm in Patients With Implantable Cardioverter-Defibrillator. J. Am. Coll. Cardiol. 2018;71:1897–1906.

35. Sorajja D, Munger TM, Shen W-K. Optimal antiarrhythmic drug therapy for electrical storm. J. Biomed. Res. 2015;29:20–34.

36. Leriche R, Fontaine R. L’anesthesie isolee du ganglion etoile: sa technique, ses indications, ses resultats. Presse Méd 1934;42:849–50.

37. Gofeld M, Bhatia A, Abbas S, Ganapathy S, Johnson M. Development and validation of a new technique for ultrasound-guided stellate ganglion block. Reg. Anesth. Pain Med. 2009;34:475–479.

38. Hayase J, Vampola S, Ahadian F, Narayan SM, Krummen DE. Comparative efficacy of stellate ganglion block with bupivacaine vs pulsed radiofrequency in a patient with refractory ventricular arrhythmias. J. Clin. Anesth. 2016;31:162–165.

39. Nademanee K, Taylor R, Bailey WE, Rieders DE, Kosar EM. Treating electrical storm : sympathetic blockade versus advanced cardiac life support-guided therapy. Circulation 2000;102:742–747.

40. Loyalka P, Hariharan R, Gholkar G, et al. Left stellate ganglion block for continuous ventricular arrhythmias during percutaneous left ventricular assist device support. Tex. Heart Inst. J. 2011;38:409–411.

41. Patel RA, Priore DL, Szeto WY, Slevin KA. Left stellate ganglion blockade for the management of drug-resistant electrical storm. Pain Med. Malden Mass 2011;12:1196–1198.

42. Mahajan A, Moore J, Cesario DA, Shivkumar K. Use of thoracic epidural anesthesia for management of electrical storm: a case report. Heart Rhythm 2005;2:1359–1362.

43. Meissner A, Eckardt L, Kirchhof P, et al. Effects of thoracic epidural anesthesia with and without autonomic nervous system blockade on cardiac monophasic action potentials and effective refractoriness in awake dogs. Anesthesiology 2001;95:132–138; discussion 6A.

44. Oka T, Ozawa Y, Ohkubo Y. Thoracic epidural bupivacaine attenuates supraventricular tachyarrhythmias after pulmonary resection. Anesth. Analg. 2001;93:253–259, 1st contents page.
45. Olausson K, Magnusdottir H, Lurje L, Wennerblom B, Emanuelsson H, Ricksten SE. Anti-ischemic and anti-anginal effects of thoracic epidural anesthesia versus those of conventional medical therapy in the treatment of severe refractory unstable angina pectoris. Circulation 1997;96:2178–2182.
46. Meng L, Tseng C-H, Shivkumar K, Ajijola O. Efficacy of Stellate Ganglion Blockade in Managing Electrical Storm: A Systematic Review. JACC Clin. Electrophysiol. 2017;3:942–949.
47. Bourke T, Vaseghi M, Michowitz Y, et al. Neuraxial modulation for refractory ventricular arrhythmias: value of thoracic epidural anesthesia and surgical left cardiac sympathetic denervation. Circulation 2010;121:2255–2262.
48. Schwartz PJ, Periti M, Malliani A. The long Q-T syndrome. Am. Heart J. 1975;89:378–390.
49. JONNESCO T. Traitment chirurgical de l’ angine de poitrine par la resection du sympathetique cervicothoracique. Presse Med 1921;29:193–195.
50. Estes EH, Izlar HL. Recurrent ventricular tachycardia. A case successfully treated by bilateral cardiac sympathectomy. Am. J. Med. 1961;31:493–497.
51. Zipes DP, Festoff B, Schaal SF, Cox C, Sealy WC, Wallace AG. Treatment of ventricular arrhythmia by permanent atrial pacemaker and cardiac sympathectomy. Ann. Intern. Med. 1968;68:591–597.

52. Moss AJ, McDonald J. Unilateral cervicothoracic sympathetic ganglionectomy for the treatment of long QT interval syndrome. N. Engl. J. Med. 1971;285:903–904.

53. Wilde AAM, Bhuiyan ZA, Crotti L, et al. Left cardiac sympathetic denervation for catecholaminergic polymorphic ventricular tachycardia. N. Engl. J. Med. 2008;358:2024–2029.

54. De Ferrari GM, Dusi V, Spazzolini C, et al. Clinical Management of Catecholaminergic Polymorphic Ventricular Tachycardia: The Role of Left Cardiac Sympathetic Denervation. Circulation 2015;131:2185–2193.

55. Irie T, Yamakawa K, Hamon D, Nakamura K, Shivkumar K, Vaseghi M. Cardiac sympathetic innervation via middle cervical and stellate ganglia and antiarrhythmic mechanism of bilateral stellectomy. Am. J. Physiol. Heart Circ. Physiol. 2017;312:H392–H405.

56. Verrier RL, Thompson PL, Lown B. Ventricular vulnerability during sympathetic stimulation: role of heart rate and blood pressure. Cardiovasc. Res. 1974;8:602–610.

57. Vaseghi M, Zhou W, Shi J, et al. Sympathetic innervation of the anterior left ventricular wall by the right and left stellate ganglia. Heart Rhythm 2012;9:1303–1309.

58. Yagishita D, Chui RW, Yamakawa K, et al. Sympathetic nerve stimulation, not circulating norepinephrine, modulates T-peak to T-end interval by increasing global dispersion of repolarization. Circ. Arrhythm. Electrophysiol. 2015;8:174–185.

59. Schwartz PJ, Priori SG, Cerrone M, et al. Left cardiac sympathetic denervation in the management of high-risk patients affected by the long-QT syndrome. Circulation 2004;109:1826–1833.

60. Schwartz PJ, Priori SG, Spazzolini C, et al. Genotype-phenotype correlation in the long-QT syndrome: gene-specific triggers for life-threatening arrhythmias. Circulation 2001;103:89–95.

61. Jost Norbert, Virág László, Bitay Miklós, et al. Restricting Excessive Cardiac Action Potential and QT Prolongation. Circulation 2005;112:1392–1399.

62. Schwartz PJ, Ackerman MJ. The long QT syndrome: a transatlantic clinical approach to diagnosis and therapy. Eur. Heart J. 2013;34:3109–3116.

63. Priori SG, Wilde AA, Horie M, et al. HRS/EHRA/APHRS expert consensus statement on the diagnosis and management of patients with inherited primary arrhythmia syndromes: document endorsed by HRS, EHRA, and APHRS in May 2013 and by ACCF, AHA, PACES, and AEPC in June 2013. Heart Rhythm 2013;10:1932–1963.

64. Antiel RM, Bos JM, Joyce DD, et al. Quality of life after videoscopic left cardiac sympathetic denervation in patients with potentially life-threatening cardiac channelopathies/cardiomyopathies. Heart Rhythm 2016;13:62–69.

65. Schwartz PJ. When the risk is sudden death, does quality of life matter? Heart Rhythm 2016;13:70–71.

66. Collura CA, Johnson JN, Moir C, Ackerman MJ. Left cardiac sympathetic denervation for the treatment of long QT syndrome and catecholaminergic polymorphic ventricular tachycardia using video-assisted thoracic surgery. Heart Rhythm 2009;6:752–759.

67. Roston TM, Vinocur JM, Maginot KR, et al. Catecholaminergic polymorphic ventricular tachycardia in children: analysis of therapeutic strategies and outcomes from an international multicenter registry. Circ. Arrhythm. Electrophysiol. 2015;8:633–642.
68. Yanowitz F, Preston JB, Abildskov JA. Functional distribution of right and left stellate innervation to the ventricles: production of neurogenic electrocardiographs changes by unilateral alteration of sympathetic tone. Circ. Res. 1966;18:416–428.
69. Wichter T, Hindricks G, Lerch H, et al. Regional myocardial sympathetic dysinnervation in arrhythmogenic right ventricular cardiomyopathy. An analysis using 123I-meta-iodobenzylguanidine scintigraphy. Circulation 1994;89:667–683.
70. Schwartz PJ, Verrier RL, Lown B. Effect of stellectomy and vagotomy on ventricular refractoriness in dogs. Circ. Res. 1977;40:536–540.
71. Cinca J, Evangelista A, Montoyo J, et al. Electrophysiologic effects of unilateral right and left stellate ganglion block on the human heart. Am. Heart J. 1985;109:46–54.
72. García-Calvo R, Chorro FJ, Sendra M, et al. The effects of selective stellate ganglion manipulation on ventricular refractoriness and excitability. Pacing Clin. Electrophysiol. PACE 1992;15:1492–1503.
73. Vaseghi M, Barwad P, Malavassi Corrales FJ, et al. Cardiac Sympathetic Denervation for Refractory Ventricular Arrhythmias. J. Am. Coll. Cardiol. 2017;69:3070–3080.
74. ClinicalTrials.gov. Identifier NCT01013714, Cardiac Sympathetic Denervation for Prevention of Ventricular Tachyarrhythmias - (PREVENT VT). 2009. Available at: https://clinicaltrials.gov/ct2/show/NCT01013714. Accessed May 16, 2019.

75. Bernard C. Leçons sur les propriétés physiologiques et les altérations pathologiques des liquides de l'organisme. Tome II. 1859;2.

76. Starling EH. THE CHEMICAL CONTROL OF THE BODY. J. Am. Med. Assoc. 1908;L:835–840.

77. Shivkumar K, Ajijola OA, Anand I, et al. Clinical neurocardiology defining the value of neuroscience-based cardiovascular therapeutics. J. Physiol. 2016;594:3911–3954.

78. DiBona GF, Esler M. Translational medicine: the antihypertensive effect of renal denervation. Am. J. Physiol. Regul. Integr. Comp. Physiol. 2010;298:R245-253.

79. Tung R, Shivkumar K. Neuraxial modulation for treatment of VT storm. J. Biomed. Res. 2015;29:56–60.

80. Jackson N, Gizurarson S, Azam MA, et al. Effects of Renal Artery Denervation on Ventricular Arrhythmias in a Postinfarct Model. Circ. Cardiovasc. Interv. 2017;10:e004172.

81. Armaganijan LV, Staico R, Moreira DAR, et al. 6-Month Outcomes in Patients With Implantable Cardioverter-Defibrillators Undergoing Renal Sympathetic Denervation for the Treatment of Refractory Ventricular Arrhythmias. JACC Cardiovasc. Interv. 2015;8:984–990.

82. Evranos B, Canpolat U, Kocyigit D, Coteli C, Yorgun H, Aytemir K. Role of Adjuvant Renal Sympathetic Denervation in the Treatment of Ventricular Arrhythmias. Am. J. Cardiol. 2016;118:1207–1210.

83. Bradfield JS, Vaseghi M, Shivkumar K. Renal denervation for refractory ventricular arrhythmias. Trends Cardiovasc. Med. 2014;24:206–213.

84. Liu K, Do D, Sorg J, et al. Abstract 16805: Renal Sympathetic Denervation as an Adjunctive Therapy to Radiofrequency Ablation and Cardiac Sympathetic Denervation for Refractory Ventricular Tachycardia. Circulation 2018;138:A16805–A16805.

85. Steinberg J. Evaluate Renal Artery Denervation In Addition to Catheter Ablation To Eliminate Atrial Fibrillation (ERADICATE-AF) Trial. Late Breaking Clinical Trial presented at: Heart Rhythm Scientific Sessions; May 9, 2019; San Francisco, CA.

86. Mannheimer C, Camici P, Chester MR, et al. The problem of chronic refractory angina; report from the ESC Joint Study Group on the Treatment of Refractory Angina. Eur. Heart J. 2002;23:355–370.

87. Zhang TC, Janik JJ, Grill WM. Mechanisms and models of spinal cord stimulation for the treatment of neuropathic pain. Brain Res. 2014;1569:19–31.

88. Wang S, Zhou X, Huang B, et al. Spinal cord stimulation protects against ventricular arrhythmias by suppressing left stellate ganglion neural activity in an acute myocardial infarction canine model. Heart Rhythm 2015;12:1628–1635.

89. Odenstedt J, Linderoth B, Bergfeldt L, et al. Spinal cord stimulation effects on myocardial ischemia, infarct size, ventricular arrhythmia, and noninvasive electrophysiology in a porcine ischemia-reperfusion model. Heart Rhythm 2011;8:892–898.

90. Lopshire JC, Zipes DP. Spinal cord stimulation for heart failure: preclinical studies to determine optimal stimulation parameters for clinical efficacy. J Cardiovasc. Transl. Res. 2014;7:321–329.

91. Foreman RD, Linderoth B, Ardell JL, et al. Modulation of intrinsic cardiac neurons by spinal cord stimulation: implications for its therapeutic use in angina pectoris. Cardiovasc. Res. 2000;47:367–375.
92. Latif OA, Nedeljkovic SS, Stevenson LW. Spinal cord stimulation for chronic intractable angina pectoris: a unified theory on its mechanism. Clin. Cardiol. 2001;24:533–541.
93. Wu M, Linderoth B, Foreman RD. Putative mechanisms behind effects of spinal cord stimulation on vascular diseases: a review of experimental studies. Auton. Neurosci. Basic Clin. 2008;138:9–23.
94. Ardell JL. Heart failure: Mechanisms of spinal cord neuromodulation for heart disease. Nat. Rev. Cardiol. 2016;13:127–128.
95. Grimaldi R, de Luca A, Kornet L, Castagno D, Gaita F. Can spinal cord stimulation reduce ventricular arrhythmias? Heart Rhythm 2012;9:1884–1887.
96. Tse H-F, Turner S, Sanders P, et al. Thoracic Spinal Cord Stimulation for Heart Failure as a Restorative Treatment (SCS HEART study): first-in-man experience. Heart Rhythm 2015;12:588–595.
97. Zipes DP, Neuzil P, Theres H, et al. Determining the Feasibility of Spinal Cord Neuromodulation for the Treatment of Chronic Systolic Heart Failure: The DEFEAT-HF Study. JACC Heart Fail. 2016;4:129–136.
98. Li M, Zheng C, Sato T, Kawada T, Sugimachi M, Sunagawa K. Vagal nerve stimulation markedly improves long-term survival after chronic heart failure in rats. Circulation 2004;109:120–124.

99. Ando Motonori, Katare Rajesh G., Kakinuma Yoshihiko, et al. Efferent Vagal Nerve Stimulation Protects Heart Against Ischemia-Induced Arrhythmias by Preserving Connexin43 Protein. Circulation 2005;112:164–170.

100. Zhang Y, Popovic ZB, Bibevski S, et al. Chronic vagus nerve stimulation improves autonomic control and attenuates systemic inflammation and heart failure progression in a canine high-rate pacing model. Circ. Heart Fail. 2009;2:692–699.

101. Waxman MB, Wald RW. Termination of ventricular tachycardia by an increase in cardiac vagal drive. Circulation 1977;56:385–391.

102. Uthman BM, Reichl AM, Dean JC, et al. Effectiveness of vagus nerve stimulation in epilepsy patients: a 12-year observation. Neurology 2004;63:1124–1126.

103. Shuchman M. Approving the vagus-nerve stimulator for depression. N. Engl. J. Med. 2007;356:1604–1607.

104. De Ferrari GM, Crijns HJGM, Borggrefe M, et al. Chronic vagus nerve stimulation: a new and promising therapeutic approach for chronic heart failure. Eur. Heart J. 2011;32:847–855.

105. Zuanetti G, De Ferrari GM, Priori SG, Schwartz PJ. Protective effect of vagal stimulation on reperfusion arrhythmias in cats. Circ. Res. 1987;61:429–435.

106. Vanoli E, De Ferrari GM, Stramba-Badiale M, Hull SS, Foreman RD, Schwartz PJ. Vagal stimulation and prevention of sudden death in conscious dogs with a healed myocardial infarction. Circ. Res. 1991;68:1471–1481.

107. Yamakawa K, So EL, Rajendran PS, et al. Electrophysiological effects of right and left vagal nerve stimulation on the ventricular myocardium. Am. J. Physiol. Heart Circ. Physiol. 2014;307:H722-731.

108. Yamakawa K, Rajendran PS, Takamiya T, et al. Vagal nerve stimulation activates vagal afferent fibers that reduce cardiac efferent parasympathetic effects. Am. J. Physiol. Heart Circ. Physiol. 2015;309:H1579-1590.

109. Vaseghi M, Salavatian S, Rajendran PS, et al. Parasympathetic dysfunction and antiarrhythmic effect of vagal nerve stimulation following myocardial infarction. JCI Insight 2017;2.

110. Ardell JL, Rajendran PS, Nier HA, KenKnight BH, Armour JA. Central-peripheral neural network interactions evoked by vagus nerve stimulation: functional consequences on control of cardiac function. Am. J. Physiol. Heart Circ. Physiol. 2015;309:H1740-1752.

111. Ardell JL, Nier H, Hammer M, et al. Defining the neural fulcrum for chronic vagus nerve stimulation: implications for integrated cardiac control. J. Physiol. 2017;595:6887–6903.

112. Zannad F, De Ferrari GM, Tuinenburg AE, et al. Chronic vagal stimulation for the treatment of low ejection fraction heart failure: results of the NEural Cardiac TherApy foR Heart Failure (NECTAR-HF) randomized controlled trial. Eur. Heart J. 2015;36:425–433.

113. Premchand RK, Sharma K, Mittal S, et al. Autonomic regulation therapy via left or right cervical vagus nerve stimulation in patients with chronic heart failure: results of the ANTHEM-HF trial. J. Card. Fail. 2014;20:808–816.

114. Hauptman PJ, Schwartz PJ, Gold MR, et al. Rationale and study design of the increase of vagal tone in heart failure study: INOVATE-HF. Am. Heart J. 2012;163:954-962.e1.

115. Byku M, Mann DL. Neuromodulation of the Failing Heart. JACC Basic Transl. Sci. 2016;1:95–106.

116. Hanna P, Shivkumar K, Ardell JL. Calming the Nervous Heart: Autonomic Therapies in Heart Failure. Card. Fail. Rev. 2018;4:92–98.

117. Yamaguchi N, Yamakawa K, Rajendran PS, Takamiya T, Vaseghi M. Antiarrhythmic effects of vagal nerve stimulation after cardiac sympathetic denervation in the setting of chronic myocardial infarction. Heart Rhythm 2018;15:1214–1222.

118. Spuck S, Tronnier V, Orosz I, et al. Operative and technical complications of vagus nerve stimulator implantation. Neurosurgery 2010;67:489–494.

119. Yu L, Wang S, Zhou X, et al. Chronic Intermittent Low-Level Stimulation of Tragus Reduces Cardiac Autonomic Remodeling and Ventricular Arrhythmia Inducibility in a Post-Infarction Canine Model. JACC Clin. Electrophysiol. 2016;2:330–339.

120. Yu L, Huang B, Po SS, et al. Low-Level Tragus Stimulation for the Treatment of Ischemia and Reperfusion Injury in Patients With ST-Segment Elevation Myocardial Infarction: A Proof-of-Concept Study. JACC Cardiovasc. Interv. 2017;10:1511–1520.

121. Garrey WE. Auricular fibrillation. Physiol. Rev. 1924;4:215–250.

122. Allessie MA, Bonke FI, Schopman FJ. Circus movement in rabbit atrial muscle as a mechanism of tachycardia. III. The “leading circle” concept: a new model of circus movement in cardiac tissue without the involvement of an anatomical obstacle. Circ. Res. 1977;41:9–18.

123. Allessie MA, Lammers WJ, Bonke IM, Hollen J. Intra-atrial reentry as a mechanism for atrial flutter induced by acetylcholine and rapid pacing in the dog. Circulation 1984;70:123–135.

124. Burn JH, Williams EMV, Walker JM. The effects of acetylcholine in the heart-lung preparation including the production of auricular fibrillation. J. Physiol. 1955;128:277–293.

125. Zipes DP, Mihalick MJ, Robbins GT. Effects of selective vagal and stellate ganglion stimulation of atrial refractoriness. Cardiovasc. Res. 1974;8:647–655.

126. Liu L, Nattel S. Differing sympathetic and vagal effects on atrial fibrillation in dogs: role of refractoriness heterogeneity. Am. J. Physiol. 1997;273:H805-816.

127. Smeets JL, Allessie MA, Lammers WJ, Bonke FI, Hollen J. The wavelength of the cardiac impulse and reentrant arrhythmias in isolated rabbit atrium. The role of heart rate, autonomic transmitters, temperature, and potassium. Circ. Res. 1986;58:96–108.

128. Chiou CW, Eble JN, Zipes DP. Efferent vagal innervation of the canine atria and sinus and atrioventricular nodes. The third fat pad. Circulation 1997;95:2573–2584.

129. Schauerte P, Scherlag BJ, Pitha J, et al. Catheter ablation of cardiac autonomic nerves for prevention of vagal atrial fibrillation. Circulation 2000;102:2774–2780.

130. Haïssaguerre M, Jaïs P, Shah DC, et al. Spontaneous Initiation of Atrial Fibrillation by Ectopic Beats Originating in the Pulmonary Veins. N. Engl. J. Med. 1998;339:659–666.

131. Tsai CF, Chen SA, Tai CT, et al. Bezold-Jarisch-like reflex during radiofrequency ablation of the pulmonary vein tissues in patients with paroxysmal focal atrial fibrillation. J. Cardiovasc. Electrophysiol. 1999;10:27–35.

132. Hsieh MH, Chiou CW, Wen ZC, et al. Alterations of heart rate variability after radiofrequency catheter ablation of focal atrial fibrillation originating from pulmonary veins. Circulation 1999;100:2237–2243.

133. Tan AY, Li H, Wachsmann-Hogiu S, Chen LS, Chen P-S, Fishbein MC. Autonomic innervation and segmental muscular disconnections at the human pulmonary vein-atrial junction: implications for catheter ablation of atrial-pulmonary vein junction. J. Am. Coll. Cardiol. 2006;48:132–143.

134. Katritsis DG, Giazitzoglou E, Zografos T, Pokushalov E, Po SS, Camm AJ. Rapid pulmonary vein isolation combined with autonomic ganglia modification: a randomized study. Heart Rhythm 2011;8:672–678.

135. Katritsis DG, Pokushalov E, Romanov A, et al. Autonomic denervation added to pulmonary vein isolation for paroxysmal atrial fibrillation: a randomized clinical trial. J. Am. Coll. Cardiol. 2013;62:2318–2325.

136. Steinberg JS, Pokushalov E, Mittal S. Renal denervation for arrhythmias: hope or hype? Curr. Cardiol. Rep. 2013;15:392.

137. Han FT, Kasirajan V, Kowalski M, et al. Results of a minimally invasive surgical pulmonary vein isolation and ganglionic plexi ablation for atrial fibrillation: single-center experience with 12-month follow-up. Circ. Arrhythm. Electrophysiol. 2009;2:370–377.

138. Edgerton JR, Brinkman WT, Weaver T, et al. Pulmonary vein isolation and autonomic denervation for the management of paroxysmal atrial fibrillation by a minimally invasive surgical approach. J. Thorac. Cardiovasc. Surg. 2010;140:823–828.

139. Krul SPJ, Driessen AHG, van Boven WJ, et al. Thoracoscopic video-assisted pulmonary vein antrum isolation, ganglionated plexus ablation, and periprocedural confirmation of ablation lesions: first results of a hybrid surgical-electrophysiological approach for atrial fibrillation. Circ. Arrhythm. Electrophysiol. 2011;4:262–270.

140. Báez-Escudero JL, Keida T, Dave AS, Okishige K, Valderrábano M. Ethanol infusion in the vein of Marshall leads to parasympathetic denervation of the human left atrium: implications for atrial fibrillation. J. Am. Coll. Cardiol. 2014;63:1892–1901.

141. Pauza DH, Skripka V, Pauziene N, Stropus R. Morphology, distribution, and variability of the epicardiac neural ganglionated subplexuses in the human heart. Anat. Rec. 2000;259:353–382.

142. Driessen AHG, Berger WR, Krul SPJ, et al. Ganglion Plexus Ablation in Advanced Atrial Fibrillation: The AFACT Study. J. Am. Coll. Cardiol. 2016;68:1155–1165.

143. Romanov A, Pokushalov E, Ponomarev D, et al. Long-term suppression of atrial fibrillation by botulinum toxin injection into epicardial fat pads in patients undergoing cardiac surgery: Three-year follow-up of a randomized study. Heart Rhythm 2018.

144. Tai CT, Chiou CW, Wen ZC, et al. Effect of phenylephrine on focal atrial fibrillation originating in the pulmonary veins and superior vena cava. J. Am. Coll. Cardiol. 2000;36:788–793.

145. Li S, Scherlag BJ, Yu L, et al. Low-level vagosympathetic stimulation: a paradox and potential new modality for the treatment of focal atrial fibrillation. Circ. Arrhythm. Electrophysiol. 2009;2:645–651.

146. Sha Y, Scherlag BJ, Yu L, et al. Low-level right vagal stimulation: anticholinergic and antiadrenergic effects. J. Cardiovasc. Electrophysiol. 2011;22:1147–1153.

147. Sheng X, Scherlag BJ, Yu L, et al. Prevention and reversal of atrial fibrillation inducibility and autonomic remodeling by low-level vagosympathetic nerve stimulation. J. Am. Coll. Cardiol. 2011;57:563–571.

148. Shen MJ, Cheng H-C, Park H-W, et al. Low-level vagus nerve stimulation upregulates small conductance calcium-activated potassium channels in the stellate ganglion. Heart Rhythm 2013;10:910–915.

149. Stavrakis S, Scherlag BJ, Fan Y, et al. Antiarrhythmic effects of vasostatin-1 in a canine model of atrial fibrillation. J. Cardiovasc. Electrophysiol. 2012;23:771–777.

150. Salavatian S, Beaumont E, Longpré J-P, et al. Vagal stimulation targets select populations of intrinsic cardiac neurons to control neurally induced atrial fibrillation. Am. J. Physiol. - Heart Circ. Physiol. 2016;311:H1311–H1320.

151. Yu L, Scherlag BJ, Li S, et al. Low-level transcutaneous electrical stimulation of the auricular branch of the vagus nerve: a noninvasive approach to treat the initial phase of atrial fibrillation. Heart Rhythm 2013;10:428–435.

152. Stavrakis S, Humphrey MB, Scherlag BJ, et al. Low-level transcutaneous electrical vagus nerve stimulation suppresses atrial fibrillation. J. Am. Coll. Cardiol. 2015;65:867–875.

153. Stavrakis S. Transcutaneous Electrical Vagus Nerve Stimulation To Suppress Atrial Fibrillation (TREAT AF): A Randomized Clinical Trial. Late Breaking Clinical Trial presented at: Heart Rhythm Scientific Sessions; May 9, 2019; San Francisco, CA.

154. Rajendran PS, Challis RC, Fowlkes CC, et al. Identification of peripheral neural circuits that regulate heart rate using optogenetic and viral vector strategies. Nature Communications 2019;10:1944.

Chapter 2:

Integrative mapping of neural structure and cardiac electrophysiology

Introduction

At the level of the nerve-myocyte interface, existing literature on neural control of myocardial impulse propagation has focused on molecular and cellular aspects, describing *in vitro* autonomic influence on cardiomyocyte function in normal and diseased states (1–5). These findings have been vital to the advancement of pharmacologic therapies, which have had significant, though incomplete, success in reducing cardiac morbidity and mortality (6). As anti-arrhythmic therapies also focus on structural substrate modification (7), elucidating upstream organ-level neurocardiac control is crucial to bridging the bench-to-bedside gap.

Previous studies using immunostaining of heart sections (8) and, more recently, tissue clearing of whole hearts (9) have shown intramyocardial neural structure at high resolution. However, the inability to directly correlate high-resolution structural and functional data from the same heart has impeded our understanding of how intramyocardial nerves directly control cardiac impulse propagation.

Our previous work established an important technical basis for high-resolution imaging and semi-automated analysis of global innervation patterns in healthy hearts (10). In this study, we integrate our prior techniques with electrical mapping of intact, diseased hearts to establish a novel, multi-modal pipeline allowing direct structure-to-function correlation.

RESULTS

High-resolution mapping and alignment of cardiac structure with electrical function

To evaluate structure-function relationships and changes in these relationships after MI, we developed a pipeline of aligning optical maps of myocardial impulse propagation directly with high-resolution images of myofiber and nerve fiber structure in the same hearts after tissue clearing and semi-automated fiber tracing (Figure 6A). With a two-camera system, we first optically mapped action potentials (APs) in normal (sham) hearts and chronic MI hearts and obtained a simultaneous brightfield image of surface vascular features (Figure 6B-C). We then fixed these hearts, immunolabeled them with the sympathetic nerve marker tyrosine hydroxylase (TH), and performed tissue clearing using a modified, immunolabeling-enabled 3-dimensional imaging of solvent-cleared organs (iDISCO) method (11) to allow for high-resolution confocal imaging and semi-automated structural analysis (10) (Figure 6D-F). To align the structural images back to the optical electrical maps, we used vascular fiducial points (venous bifurcations) clearly visible on both the brightfield heart images and the confocal images of muscle autofluorescence (Figure 6G-H). We found this transformation was sufficient to account for tissue deformation after clearing, bringing fiducials into good alignment over most of the surface visible in the brightfield image. Thus we were able to overlay structural data such as global nerve fiber features (Figure 6I) directly and precisely onto functional electrical data from the same hearts.

Structure-function alignment precisely correlates global ventricular electrical

propagation with myofiber orientation

After developing our structure-function alignment pipeline, we validated it in a proof-of-concept analysis to demonstrate the relationship between ventricular myofiber orientation and directionality of electrical propagation in the same heart. Ventricular conduction vectors were calculated from activation maps with basolateral left ventricular (LV) pacing (Figure 7A), exported as angular data matrices (Figure 7B), and visualized as vector orientation colormaps (Figure 7C). High-resolution muscle autofluorescence images were used for automated tracing of myofiber orientations (Figure 7D-E), which were then also visualized as colormaps (Figure 7F). We validated this automated myofiber tracing by comparison of muscle autofluorescence to viral labeling of cardiomyocytes (Figure 8).

Once the pairs of functional and structural maps from four representative sham hearts were aligned, we first qualitatively assessed the association between myofiber orientation and conduction vector orientation by creating cosine similarity maps (Figure 7G). Of note, our method of alignment detected the area of lowest cosine similarity around the right ventricular (RV) insertion point (where RV wall attaches to the interventricular septum anteriorly), where there is almost a 90-degree shift in myofiber orientation. Next, we quantitatively analyzed the degree of structure-function concordance in each heart by calculating angular correlation coefficients between myofiber and conduction data matrices, and then testing for matrix similarity (Table 1). We found significantly close correlation between structural myofiber orientation and functional conduction vector orientation, thus validating our alignment method and experimentally demonstrating the cable theory of myocardial impulse propagation (12–

14) at the global ventricular level.

DISCUSSION

We developed a high-resolution platform for precisely aligning functional maps of electrical propagation to structural maps of muscle and nerve fibers, using optical mapping, state-of-the-art intact-heart imaging, and computer vision algorithms for semi-automated feature detection. We validated this platform by demonstrating direct spatial correlation of ventricular myofiber structure to directionality of AP propagation at the global ventricular level. Our structure-function alignment method demonstrates close, global concordance between myofiber architecture and conduction vector fields for the first time in intact ventricles, a relationship which had previously only been studied at the single-myocyte level (13, 15) or through computational modeling of myocardial function (16–18).

METHODS

Animals

Animal experiments complied with all relevant ethical regulations and institutional regulations of the UCLA Animal Research Committee (Protocol #16-033). All mice used were male, C57BL/6J strain, obtained from the Jackson Laboratory, and approximately 16 weeks (±4 days) of age at the time of terminal mapping experiments.

Optical mapping of action potentials

In Langendorff-perfused hearts, optical mapping of V_m was performed as previously described (19, 20). Briefly, mice were sacrificed per protocol by anesthesia with 5%

isoflurane followed by cervical dislocation. Hearts were removed immediately and perfused via the aortic root with Tyrode's solution (130mM NaCl, 1.25mM $CaCl_2$, 5mM KCl, 1.2mM NaH_2PO_4, 1.1mM $MgCl_2$, 22mM $NaHCO_3$, and 50mM dextrose). Hearts were immobilized and immersed in a Tyrode's solution bath within a 3-D printed chamber to reduce motion artifact. Perfusate and bath temperature were maintained at 36.6-37°C. Hearts were stained with bolus injections of voltage-sensitive dye RH237 (8-10 µl of 2 mg/ml in DMSO, Thermo Fisher Scientific, S1109) into the coronary perfusate. Blebbistatin (Cayman Chemical, 13186) was added to the perfusate at a concentration of 1.7ug/mL for excitation-contraction uncoupling.

Light from two collimated ultra-high-power LED (Prizmatix, UHP-T-520-EP) guides was focused on the ventral epicardial surface of the heart for excitation. Emitted fluorescence was collected using a tandem-lens arrangement of Nikon NIKKOR 50mm f/1.2 camera lenses and split with a 635 nm dichroic mirror (Edmund Optics, 87064) (21). The V_m signal was filtered at 690 ± 50 nm (Chroma ET690/50m), and a simultaneous brightfield image for vascular visualization and alignment was taken using the shorter-wavelength filtered light at 590 ± 33nm (Chroma ET590/33m). The emitted Vm signals and brightfield images (for vascular alignment) were recorded using 2 CMOS cameras (SciMedia, MiCAM N256) with a sampling rate of 1.03 kHz and 256 x 256 pixels with a 14 x 14 mm field of view. Pixel resolution of the images was approximately 55 x 55 µm. Data were acquired in 2-second intervals before and after addition of tyramine to the perfusate at a concentration of 5 µM. Data acquisition was done using BV Workbench software version 1.7.10 (SciMedia).

For conduction velocity analyses, epicardial pacing was performed from the basolateral LV wall at a cycle length (CL) of 167ms (with current of 1.1-1.3 mA and pulse width of 0.8 ms), using a Transonic Scisense 1.1F mouse EP catheter (FTS-1113A-0518).

Optical mapping data analysis

Optical mapping data was analyzed using the open-source software ElectroMap (22). V_m activation maps were displayed as isochronal maps generated from points of maximum upstroke $(dF/dt)_{max}$ as well as depolarization midpoint of optical APs. Repolarization maps were generated from points of APD_{80}. A minimum of 4 beats were averaged at baseline and after tyramine infusion. A 3x3 Gaussian spatial filter, Top-hat, and Savitzky-Golay filters were applied to correct for baseline drift and noise. Maps were exported as 256 x 256 data matrices for alignment with structural data and quantitative analyses.

Immunohistochemistry and tissue clearing

After optical mapping, whole mouse hearts were fixed by immersion in 4% paraformaldehyde/phosphate-buffered saline (PBS) overnight at 4°C, then washed three times for 1h in 0.01M PBS at room temperature (RT). Hearts were stained and cleared using a modified iDISCO protocol (11). Fixed hearts were dehydrated by graded methanol treatments (20%, 40%, 60%, and 80% methanol in H_2O (vol/vol), each for 1 h at RT), washed twice with 100% methanol for 1 h at RT, and chilled at 4°C. Hearts were then immersed in 66% dichloromethane/33% methanol overnight at RT with agitation, washed twice in 100% methanol for 1 h at RT, and chilled to 4°C. Next, hearts were bleached with 5% H_2O_2 in methanol (vol/vol) overnight at 4°C. After bleaching, hearts were rehydrated with graded methanol treatments, followed by one wash with 0.01 M PBS and 2 washes with 0.01 M PBS with 0.2% Triton X-100, each for 1 h at RT. Hearts were permeabilized with 0.01 M PBS with 0.2% Triton X-100, 20% DMSO, and 0.3 M glycine and blocked with 0.01 M PBS with 0.2% Triton X-100, 10% DMSO, and 5% normal donkey serum, each for 2 d at 37°C with agitation. Hearts were incubated in sheep anti-TH (EMD Millipore, AB1542, 1:200) and/or rabbit anti-periostin (Abcam, ab14041, 1:200) diluted in 0.01 M PBS with 0.2% Tween-20 and 10 mg/ml heparin (PTwH) for 5-7 days at 37°C with agitation. Hearts were then washed 4-5 times in PTwH overnight at RT before incubating in secondary antibodies donkey anti-rabbit Cy3 (Jackson ImmunoResearch, 711-165-152, 1:300) and/or donkey anti-sheep Alexa Fluor 647 (Jackson ImmunoResearch, 713-605-147, 1:300) diluted in PTwH for 5-7 days at 37°C with agitation. Primary and secondary Ab were replenished approximately halfway through incubation period. Hearts were then washed several times in PTwH overnight at room temperature. For clearing, stained hearts were dehydrated with a graded methanol series and incubated in 66% dichloromethane/33% methanol for 3 h at room temperature with agitation. Hearts were then washed twice in 100% dichloromethane for 15 min at room temperature. Hearts were stored in benzyl ether (Millipore Sigma, 108014 ALDRICH; refractive index: 1.55) for up to 7 days prior to imaging.

Confocal imaging

Hearts were mounted in benzyl ether with adhesive plastic spacers (Sunjin Labs, IS012 and IS012). Images were acquired on a confocal laser scanning microscope (Zeiss, LSM 880) fitted with the following objectives: Fluar 5x/0.25 M27 Plan-Apochromat (working distance 12.5mm) and 10x/0.45 M27 (working distance 2.0 mm). Images were taken at both 5x and 10x magnifications for specific ROIs, such as RV and LV base, prior to the whole hearts being imaged at 5x in tiles with XY-resolution of 1.661μm and Z-resolution of 8.29μm.

Image processing and automated structural mapping

All image processing was performed using Zeiss Zen 2.1 v11, NIH ImageJ, Fiji (23), and custom Matlab scripts (available upon request from corresponding author). Computational tracing of nerve fibers was performed using a customized version of the open-source software neuTube (24). neuTube software was originally developed for tracing morphology of single cells. To trace nerves in large image volumes required additional pre- and post-processing including: (1) partitioning large volumes into smaller tiles, tracing each tile, and reassembling the traced morphologies, and (2) filtering out spurious junctions between parallel fibers and inaccurate fiber diameter estimates arising due to background staining. To quantify myofiber orientation distributions, we utilized confocal images of muscle autofluorescence. This was validated using comparison of autofluorescence with virally labeled myocyte imaging (Supplemental Figure 8). We computed the image gradient orientation at each point and then smoothed the gradient orientation field using a Gaussian weighted moving average window of size σ=100μm.

Structural images were aligned to functional images using vascular fiducial points from brightfield images obtained during optical mapping. For each sample, 5-10 fiducial points (branches in vasculature) visible in both brightfield optical mapping and confocal images were used to fit a perspective warping (homography) between the two images. Only structural data from the outer 100μm-thick "shell" of each heart were used for alignment and correlation with optical mapping data. This depth was determined empirically by light penetration experiments (Figure 9).

Quantitative data analysis

Conduction velocity and activation curves were calculated using ElectroMap. Cosine similarity maps were generated by calculating the cosine of the difference in angles at each pixel between the functional (conduction velocity) maps and the structural (myofiber orientation) maps.

Statistics

Angular correlation coefficients and matrix similarity p-values were calculated using open-source Matlab scripts for circular statistics (25) and a customized Matlab script based on open-source code utilizing Mantel's matrix similarity test (BRAMILA pipeline v2.0, available at https://version.aalto.fi/gitlab/BML/bramila) using 1000 permutations. Data are presented as medians in figures, and sample sizes are indicated in figure legends or main text. All statistical analyses for comparison are indicated in figure legends or main text, were two-tailed, and were performed in Prism 9.0.2 (GraphPad).

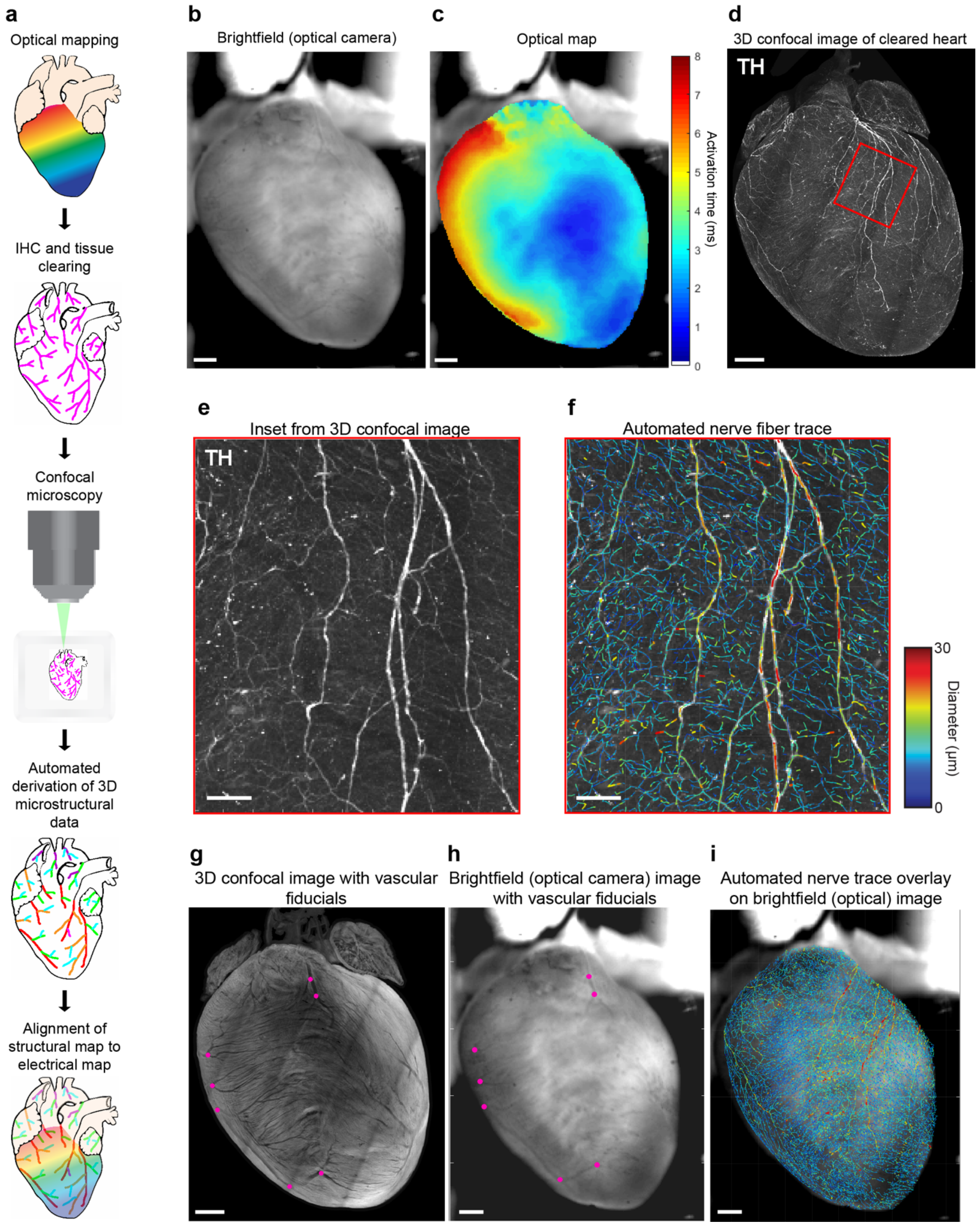

Figure 6. Optical mapping and tissue clearing pipeline to align electrical and structural maps. (a) Schematic of optical mapping, clearing, imaging, and automated

feature tracing steps in the alignment pipeline. **(b, c)** Brightfield image taken simultaneously with optical action potential map showing activation in sinus rhythm. **(d)** Maximum intensity projection (MIP) image of tyrosine hydroxylase (TH)-positive nerve fibers on the ventral surface of the same heart after immunohistochemistry (IHC), tissue clearing, and confocal imaging. **(e, f)** Zoomed insets of (**d**) with TH staining alongside nerve fiber tracing by computer vision, color-coded by fiber diameter. **(g, h)** Venous bifurcations (magenta points) on MIP confocal shell image of a cleared heart alongside brightfield image of same heart were used as fiducial anchors for alignment. **(i)** Automated global nerve fiber tracing aligned with brightfield image allows spatial correlation with optical action potential data. Scale bars are 1mm (**b-d, g-i**) and 100μm (**e, f**).

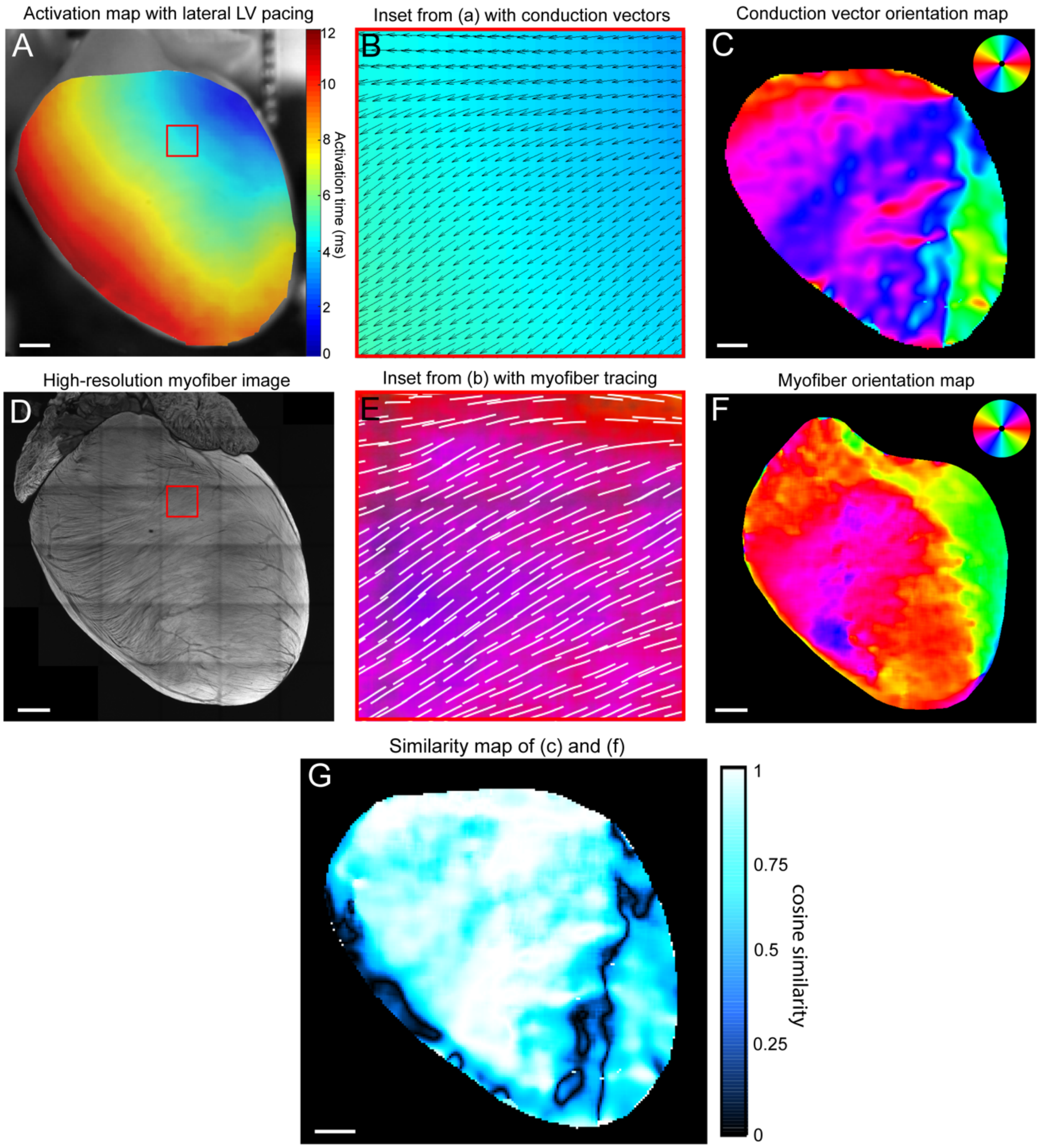

Figure 7. Structure-function alignment correlates global ventricular impulse propagation with myofiber orientation. (a) Optical activation map of representative sham heart with basolateral left ventricular (LV) pacing. **(b)** Zoomed inset of activation map with overlay of conduction velocity vectors calculated in ElectroMap. **(c)** Global ventricular conduction vector orientation map color-coded by vector angle. **(d)** Maximum intensity projection confocal image of muscle autofluorescence with high-

resolution myofiber structure. **(e)** Zoomed inset of (**d**) with overlay of automated myofiber orientation tracing. **(f)** Global ventricular myofiber orientation map color-coded by fiber angle. **(g)** Cosine similarity map calculated by taking cosine of angular difference between (**c**) and (**f**). Scale bars are 1mm (**a, c, d, f, g**).

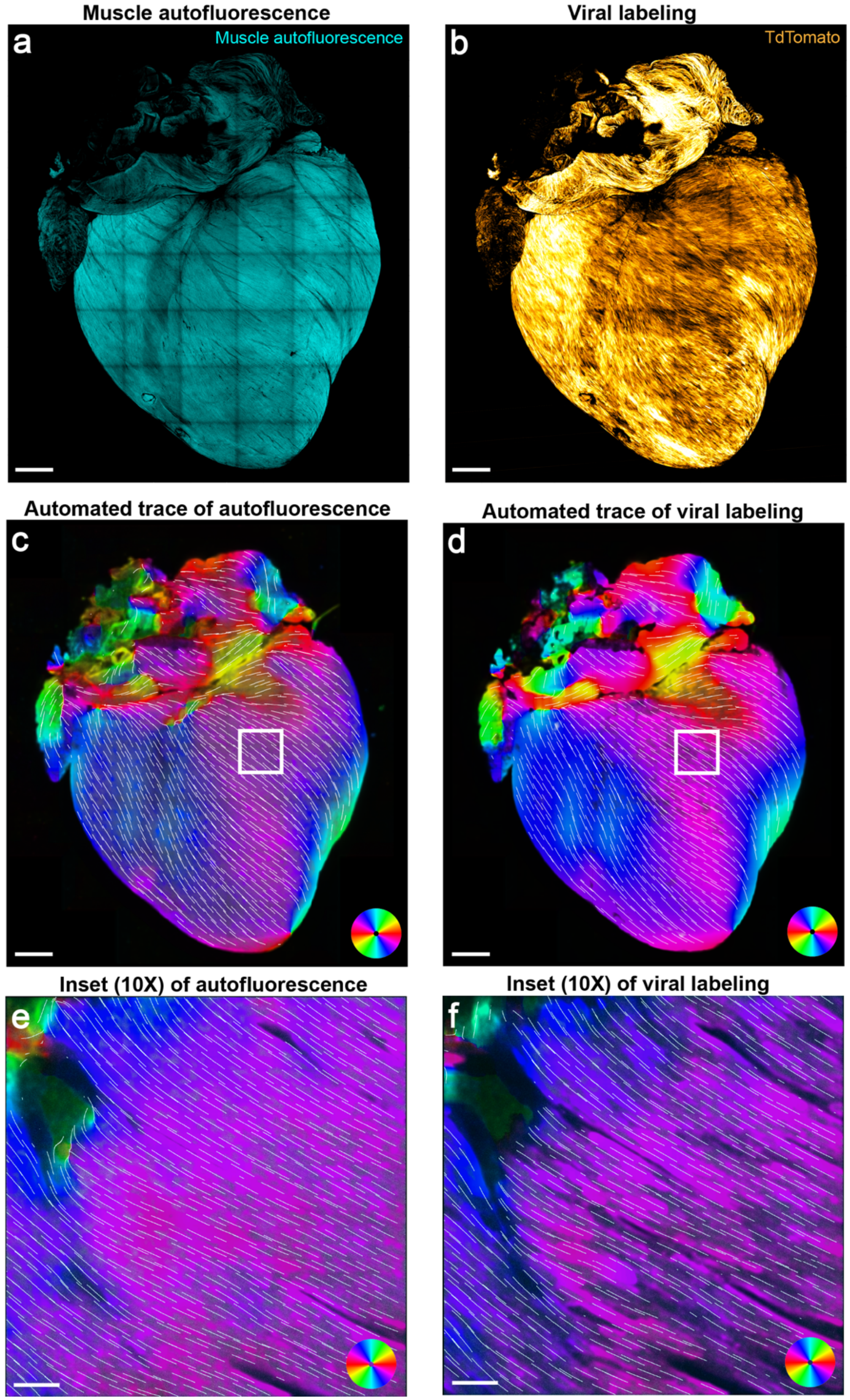

Figure 8. Validation of using muscle autofluorescence to trace myofiber orientation.

Muscle autofluorescence was imaged by excitation at 488nm and emission window collected from 491-554nm **(a)**. This was compared to fluorescent viral labeling of the same heart muscle **(b)** which was done by retro-orbital injection of AAV-PHP.S-CAG-TdTomato (1x1012 vg, Addgene, #59462-PHP.S), followed by confocal imaging after 2 weeks with excitation at 561nm and emission window from 562-625nm. Automated tracing of myofiber orientation was done for both autofluorescence and viral labeling images **(c-f)**, and Mantel matrix similarity testing was done for 2 representative hearts (angular correlation coefficients 0.9281 and 0.9169, p=1.293x10-9 and 3.127x10-8, 1000 permutations). All images are maximum intensity projections. Scale bars = 1mm **(a-d)** and 100μm **(e-f)**.

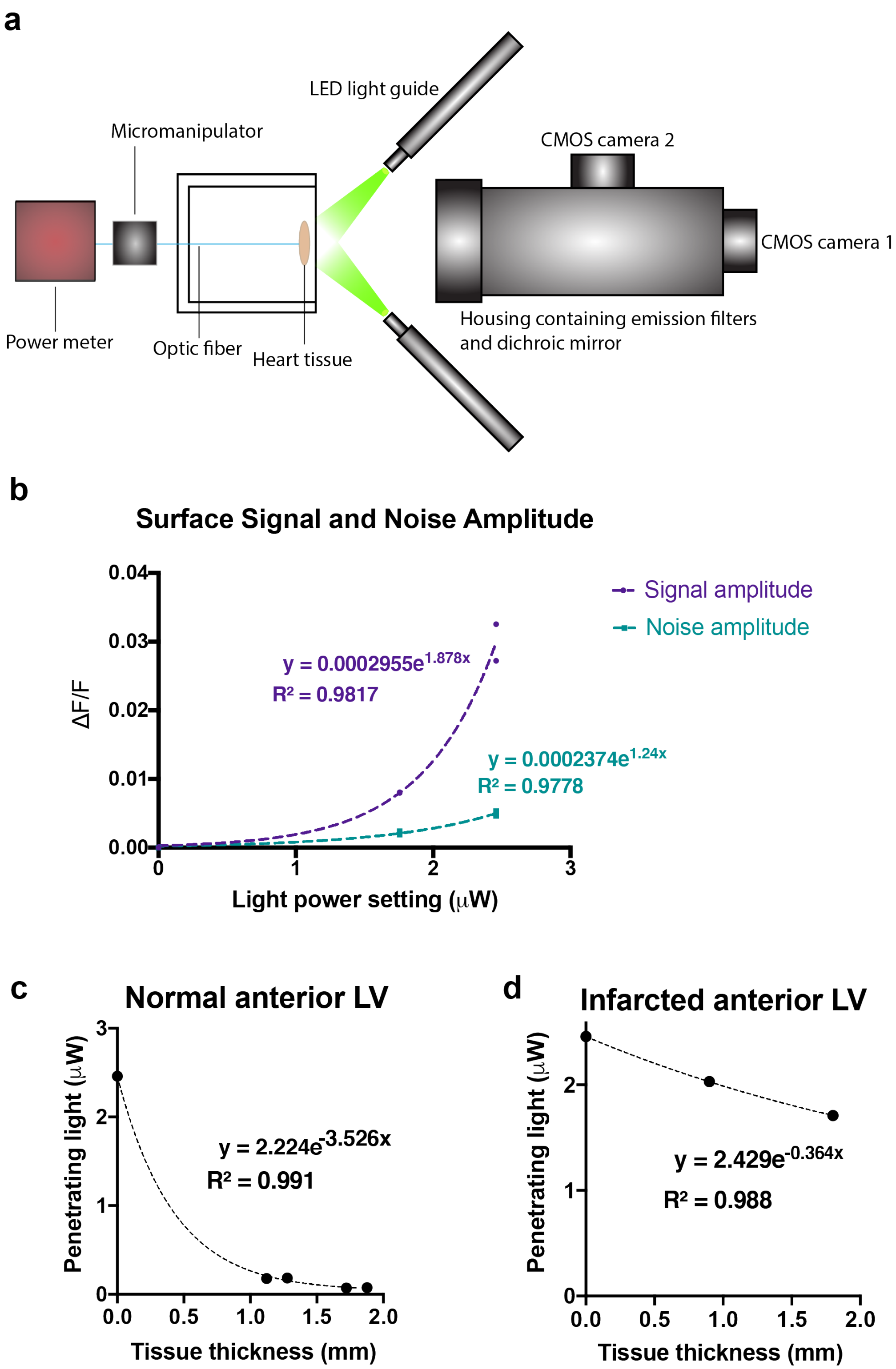

Figure 9. Light penetration measurements to calculate epicardial shell depth. To ensure structural image features were extracted from the same depth as optical action

potential (AP) signals, we empirically determined the depth of AP signals from our optical mapping system by measuring light penetration through myocardial tissue slices of varying thicknesses **(a)**. First, we plotted the relationship of different excitation light power settings to the detected signal and noise amplitude from 2 hearts **(b)**. With this plot, we used exponential regression to determine the excitation light power at which the resulting signal amplitude is equal to the noise amplitude generated by the maximal light power setting. Next, we measured the penetrating light power through normal **(c)** and infarcted **(d)** anterior LV tissue slices of different thicknesses, which displayed expected exponential decay curves per Beer's Law. Finally, we used exponential regression to calculate the tissue depth at which the light power calculated from **(b)** occurs. This was approximately 100µm deep, when correction is applied for tissue shrinkage during modified immunolabeling-enabled 3-dimensional imaging of solvent-cleared organs (iDISCO). Since this is the depth where the penetrating light power can only generate a signal amplitude equal to the noise amplitude at the surface, we defined this as our structural shell depth.

Table 1. Statistics from alignment of structural and functional heart maps.

Heart ID	Angular correlation coefficient	p-value from Mantel test of matrix similarity
59	0.8382	3.2991e-07
61	0.7776	4.5807e-07
72	0.7666	6.0493e-07
76	0.8218	5.7375e-07

REFERENCES

1. Harvey RD, Hume JR. Autonomic regulation of a chloride current in heart. Science 1989;244:983–985.

2. Harvey RD, Belevych AE. Muscarinic regulation of cardiac ion channels. Br J Pharmacol 2003;139:1074–1084.

3. Habecker BA, Anderson ME, Birren SJ, et al. Molecular and cellular neurocardiology: development, and cellular and molecular adaptations to heart disease. The Journal of Physiology 2016;594:3853–3875.

4. Raum WJ, Laks MM, Garner D, Ikuhara MH, Swerdloff RS. Norepinephrine increases beta-receptors and adenylate cyclase in canine myocardium. American Journal of Physiology-Heart and Circulatory Physiology 1984. Available at: https://journals.physiology.org/doi/abs/10.1152/ajpheart.1984.246.1.H31. Accessed May 10, 2021.

5. Lohse Martin J., Engelhardt Stefan, Eschenhagen Thomas. What Is the Role of β-Adrenergic Signaling in Heart Failure? Circulation Research 2003;93:896–906.

6. Shivkumar K, Ajijola OA, Anand I, et al. Clinical neurocardiology defining the value of neuroscience-based cardiovascular therapeutics. J. Physiol. (Lond.) 2016;594:3911–3954.

7. Shivkumar K. Catheter Ablation of Ventricular Arrhythmias. N Engl J Med 2019;380:1555–1564.

8. Vracko R, Thorning D, Frederickson RG. Nerve fibers in human myocardial scars. Hum. Pathol. 1991;22:138–146.

9. Yokoyama T, Lee J-K, Miwa K, et al. Quantification of sympathetic hyperinnervation and denervation after myocardial infarction by three-dimensional assessment of the cardiac sympathetic network in cleared transparent murine hearts. PLoS ONE 2017;12:e0182072.

10. Rajendran PS, Challis RC, Fowlkes CC, et al. Identification of peripheral neural circuits that regulate heart rate using optogenetic and viral vector strategies. Nature Communications 2019;10:1944.

11. Renier N, Wu Z, Simon DJ, Yang J, Ariel P, Tessier-Lavigne M. iDISCO: a simple, rapid method to immunolabel large tissue samples for volume imaging. Cell 2014;159:896–910.

12. Kléber AG, Rudy Y. Basic mechanisms of cardiac impulse propagation and associated arrhythmias. Physiol. Rev. 2004;84:431–488.

13. Weidmann S. The electrical constants of Purkinje fibres. J Physiol 1952;118:348–360.

14. Valderrábano M. Influence of anisotropic conduction properties in the propagation of the cardiac action potential. Prog Biophys Mol Biol 2007;94:144–168.

15. Veeraraghavan R, Gourdie RG, Poelzing S. Mechanisms of cardiac conduction: a history of revisions. Am J Physiol Heart Circ Physiol 2014;306:H619–H627.

16. Bayly PV, KenKnight BH, Rogers JM, Hillsley RE, Ideker RE, Smith WM. Estimation of conduction velocity vector fields from epicardial mapping data. IEEE Trans Biomed Eng 1998;45:563–571.

17. Rutherford SL, Trew ML, Sands GB, LeGrice IJ, Smaill BH. High-resolution 3-dimensional reconstruction of the infarct border zone: impact of structural remodeling on electrical activation. Circ Res 2012;111:301–311.

18. Tomek J, Hao G, Tomková M, et al. β-Adrenergic Receptor Stimulation and Alternans in the Border Zone of a Healed Infarct: An ex vivo Study and Computational Investigation of Arrhythmogenesis. Front Physiol 2019;10:350.

19. Lang D, Sulkin M, Lou Q, Efimov IR. Optical Mapping of Action Potentials and Calcium Transients in the Mouse Heart. J Vis Exp 2011. Available at: https://www.ncbi.nlm.nih.gov/pmc/articles/PMC3230201/. Accessed August 17, 2020.

20. Gloschat C, Aras K, Gupta S, et al. RHYTHM: An Open Source Imaging Toolkit for Cardiac Panoramic Optical Mapping. Sci Rep 2018;8:2921.

21. Cathey B, Obaid S, Zolotarev AM, et al. Open-Source Multiparametric Optocardiography. Sci Rep 2019;9:721.

22. O'Shea C, Holmes AP, Yu TY, et al. ElectroMap: High-throughput open-source software for analysis and mapping of cardiac electrophysiology. Scientific Reports 2019;9:1389.

23. Schindelin J, Arganda-Carreras I, Frise E, et al. Fiji: an open-source platform for biological-image analysis. Nat Methods 2012;9:676–682.

24. Feng L, Zhao T, Kim J. neuTube 1.0: A New Design for Efficient Neuron Reconstruction Software Based on the SWC Format. eNeuro 2015;2.

25. Berens P. **CircStat** : A *MATLAB* Toolbox for Circular Statistics. Journal of Statistical Software 2009;31. Available at: http://www.jstatsoft.org/v31/i10/. Accessed December 17, 2020.

Chapter 3:

Altered sympathetic function at infarct border zones

Introduction

Myocardial infarction (MI) and its consequent cardiac arrhythmias are leading causes of mortality in the world(1, 2). Following MI, injured myocardium creates a substrate for discontinuous electrical propagation(3–5), and concomitant neural remodeling leads to dysregulation at multiple levels of the cardiac autonomic nervous system(6–8). Together, these pathophysiological changes can lead to lethal arrhythmias.

While post-MI structural changes have been well described in several animal models (9–12) and in humans (13, 14), their mechanistic significance in arrhythmogenesis remains unclear. Functional studies using multielectrode arrays (10, 11) and optical mapping (15–19) have demonstrated perturbations in impulse propagation with stimulation of the sympathetic nervous system following MI. Yet these studies utilize imprecise approximation to define physiologically relevant regions such as the MI BZ. Thus there are limited conclusions regarding how structural remodeling of nerves impacts functional regulation of the heart post-MI in the same hearts. By merging functional electrical maps obtained by optical voltage mapping with global structural maps of the heart obtained by tissue clearing, we examine post-MI neurocardiac dynamics at microstructural resolution.

RESULTS

A composite metric of myofiber anisotropy and tissue activation time uniquely defines infarct border zones

To begin studying how structural remodeling alters electrical function after MI, we segmented both sham and MI hearts into anatomical regions of interest (ROIs) using specific structural criteria to maintain consistency across hearts. Dense scar and infarct border zone (BZ) were defined using intensity of muscle autofluorescence, and LV basal, LV apical, and RV regions were determined using anatomical landmarks (Figures 10-12). Dense scar data were excluded from these analyses due to lack of surviving myocytes (Figure 13, Supplemental Movie 1). Quantitative data from these ROIs were extracted from aligned myofiber structure maps (Figure 14A) and activation maps (Figure 14B) and were used to calculate tissue activation times and anisotropy indices of myofiber disorder. Conduction vectors at structurally defined BZ regions displayed discontinuous electrical propagation (Figure 14C). Compared to the isotropic activation curve of sham LV apex, BZ regions displayed activation curves consistent with anisotropic conduction and conduction block (20) (Figure 14D). In plots of myofiber anisotropy index versus tissue activation time, we found that ROIs from sham hearts were all tightly clustered in the low-anisotropy, fast-activation-time region of the plots (Figure 14E, Spearman r=0.0667, p=0.8801, n=9 regions from 3 mice). In contrast, the BZ in MI hearts were significantly distinct from other ROIs and localized to the high-anisotropy, slow-activation-time region of the plot (Figure 14F, Spearman r=0.833, p=0.0083, n=9 regions from 3 mice). Thus, by integrating regionally specific structural and functional data, we establish a novel quantitative metric which precisely defines the

BZ.

Chronic MI induces altered patterning of ventricular neuroeffector junctions

Having established perturbed myocardial structure-function relationships in our chronic MI model, we next turned our attention to assessing sympathetic nerve remodeling. Automatically detected nerve fiber tracings, from confocal microscopic images of whole-heart TH staining, were binned into small (1.2-3μm), medium (3-5μm), and large (5-100μm) fibers according to previously reported diameters (21–23). The same anatomically segmented ROIs used in the aforementioned myofiber analyses were applied to extract and quantify regional nerve fiber lengths (Figure 15A-F). Qualitatively, there was obvious denervation with absent TH staining at the LV apex (dense scar) of MI hearts compared to sham (Figure 15A,D). Dense scar data were excluded from these analyses due to the extremely low amount of surviving nerve fibers (Figure 16). In both sham and MI hearts, the LV base tended to have significantly more large fibers than medium and small (Kruskal-Wallis, p=0.0048 for sham, p=0.0005 for MI, n=4 mice per group), while the RV had fewer large fibers than medium and small (Kruskal-Wallis, p=0.0132 for sham, p=0.0031 for MI, n=4 mice per group) (Figure 15H,I).

The post-MI changes in small-size fibers were of special interest, as these are both closest to, and include, the neuroeffector varicosities which interface with myocytes to control cardiac function. In MI hearts, the infarct BZ showed significant increase in small fiber prevalence compared with sham LV apex (Mann-Whitney, p=0.0286), as well as decrease in medium fiber prevalence (Mann-Whitney, p=0.0286) (Figure 15G). This was visually apparent on high-magnification images of BZ versus sham LV apex (Figure 15B,E) and was detectable by our automated fiber tracing algorithm (Figure 15C,F). Interestingly, the LV base in MI hearts also displayed a decrease in small fiber prevalence (Mann-Whitney, p=0.0286) compared with sham LV base (Figure 15H). Taken together, these data establish a regional pattern of nerve sprouting at the infarct BZ along with small-fiber denervation at the remote LV base, specifically indicative of perturbed neuroeffector junction topography.

Post-MI changes in neuroeffector junction patterning underlies regional heterogeneity in sympathetic control of impulse propagation

Given the altered neuroeffector junction distribution we discovered after chronic MI, we next examined whether these regional neural changes had functional effects on myocardial impulse propagation. Using our alignment technique, we overlaid neural structural data with optical mapping data from the same hearts and assessed regional changes in repolarization after sympathetic stimulation with tyramine, which stimulates norepinephrine release from neuroeffector terminals. For previously discussed reasons, dense scar was excluded from these analyses.

We found that in sham hearts, tyramine infusion caused an expected initial prolongation of eighty percent of action potential duration (APD_{80})(24), in an evenly distributed fashion across the whole heart (Kruskal-Wallis p=0.7463) (Figure 17A,B,H). In contrast, MI hearts exhibited significant regional variation in APD_{80} prolongation after tyramine infusion (Figure 17C,D,H, Kruskal-Wallis p=0.0132). Specifically, there was more APD_{80} prolongation of the RV in MI hearts compared to the LV base and infarct

BZ (Figure 14E-G,H, Mann-Whitney p=0.0286, n=4 mice per group). When we correlated small-fiber distribution after MI to these functional repolarization changes (Figure 14I), we found that while there was a positive correlation between small-fiber prevalence and tyramine-induced APD_{80} prolongation at the LV base and RV regions (Spearman r=0.7381, p=0.0458), the BZ notably lacked this functional correlation despite having the highest prevalence of small fibers (Spearman r=0.021, p=0.956). These data demonstrate a direct, anatomically precise relationship between regional small fiber content – a surrogate index of neuroeffector junction quantity – and sympathetic control of myocardial repolarization, with the interesting exception of the functionally distinct infarct BZ.

DISCUSSION

Using our integrative mapping platform, we report several novel findings: 1) a mathematically precise definition of the infarct BZ that integrates both its distinctive microstructural and functional features; 2) perturbed neuroeffector-junction topography of the whole post-MI ventricle; and 3) a direct relationship between post-MI neuroeffector-junction distribution and altered sympathetic control of impulse propagation.

The high spatial resolution of our alignment pipeline also allows structurally precise regional analyses, which we utilized to define the infarct BZ with a novel composite metric that encompasses both myofiber anisotropy as well as discontinuous impulse propagation. The relationship between myofiber disorder and conduction block has been demonstrated previously in computational models(25) and low-resolution electrode recordings or optical maps from grossly approximated BZ regions(11, 26–29), but these studies utilized methods of localizing the BZ that are highly variable and subjective. Our findings represent the first experimental correlation of perturbed myofiber architecture to disordered electrical propagation at this degree of microstructural resolution and mathematical precision. This integrative approach to defining the BZ region by both structure and function offers unparalleled anatomical consistency for studies of its pathophysiology.

Previous studies examining the post-MI distribution of cardiac sympathetic innervation relied on manual quantification of total nerve immunofluorescence(9, 30–32) and thus lacked specificity for nerve endings versus larger pass-through fibers. In contrast, our microstructural feature detection algorithms identified regional patterns of size-specific nerve fiber remodeling, allowing focus on the functionally important neuroeffector junction. Because we were able to automatically detect and define small fiber dimensions specifically by the size of sympathetic neuroeffector terminals(21–23), we revealed the novel and important finding of small-fiber predominance at the infarct BZ and small-fiber decrease at the remote LV base. This post-MI perturbation of small-fiber topography suggests an altered neural-myocardial interface, with regional loss of neuroeffector terminals at the LV base and nerve sprouting at the BZ.

Moreover, we discovered that the altered small nerve fiber pattern after MI has a direct relationship to altered sympathetic control of ventricular repolarization. Specifically, we found that chronic MI hearts display a correlation between regional variation in tyramine-mediated APD prolongation (higher in RV compared with LV base) and the spatial distribution of small fiber prevalence (also higher in RV compared with

LV base). This finding is especially important, as it establishes a potential neural-structural substrate for the sympathetically driven increase in regional heterogeneity of repolarization, which may lead to arrhythmogenic gradients(5, 33).

Interestingly, the infarct BZ did not display higher APD prolongation compared with other regions, despite the higher small-fiber prevalence suggestive of nerve sprouting. While nerve sprouting has previously been shown to be localized at the infarct BZ and to correlate with sudden death(12, 34), the precise pathophysiological processes remain unclear. Several possible mechanisms may underlie our finding. These sprouts may be dysfunctional in tyramine uptake via the norepinephrine transporter (NET) (35), which has been previously shown to be downregulated after MI(30, 35). Alternatively, the sprouts may have altered neurotransmitter release functions(31), or the cardiomyocytes in this region may have altered adrenergic receptor profiles(36, 37). That nerve sprouting at the BZ does not align with tyramine-mediated influence on APD points to the functional distinctiveness of this boundary between surviving myocardium and dense scar, and promotes the generation of highly specific hypotheses regarding sympathetically driven arrhythmias after MI.

METHODS

Animals

Animal experiments complied with all relevant ethical regulations and institutional regulations of the UCLA Animal Research Committee (Protocol #16-033). All mice used were male, C57BL/6J strain, obtained from the Jackson Laboratory, and approximately 16 weeks (±4 days) of age at the time of terminal mapping experiments.

Creation of chronic MI mouse model

Survival surgeries to create chronic MI were performed when mice were 12 weeks (±5 days) of age (weighing 22-28g), and terminal optical mapping experiments occurred approximately 4 weeks after MI, when mice were 16 weeks (±4 days) of age. Mice were anesthetized with isoflurane (2%), endotracheally intubated, and mechanically ventilated. A small thoracotomy incision was made in the left 7th or 8th intercostal space to access the heart, the pericardium was opened with fine forceps, and the left coronary artery (analogous to the human left anterior descending artery)(38) was ligated with 8-0 silk suture at the mid-level of the LV. Acute transmural ischemia was confirmed by visualization of myocardial blanching and ST elevation on electrocardiogram (ECG). The incision was then closed in two layers (muscle and skin), and the animal was extubated and allowed to recover on a temperature-controlled surface. Carprofen (5mg/kg, intraperitoneal injection every 24 hours) and buprenorphine (0.02mg/kg, intraperitoneal injection every 8 hours) were given for pain control on the day of and for 48 hours after surgery. Sham surgeries included all steps except coronary artery ligation.

Optical mapping of action potentials

In Langendorff-perfused hearts, optical mapping of V_m was performed as previously described(39, 40). Briefly, mice were sacrificed per protocol by anesthesia with 5% isoflurane followed by cervical dislocation. Hearts were removed immediately and perfused via the aortic root with Tyrode's solution (130mM NaCl, 1.25mM $CaCl_2$, 5mM KCl, 1.2mM NaH_2PO_4, 1.1mM $MgCl_2$, 22mM $NaHCO_3$, and 50mM dextrose). Hearts were immobilized and immersed in a Tyrode's solution bath within a 3-D printed chamber to reduce motion artifact. Perfusate and bath temperature were maintained at 36.6-37°C. Hearts were stained with bolus injections of voltage-sensitive dye RH237 (8-10 µl of 2 mg/ml in DMSO, Thermo Fisher Scientific, S1109) into the coronary perfusate. Blebbistatin (Cayman Chemical, 13186) was added to the perfusate at a concentration of 1.7ug/mL for excitation-contraction uncoupling.

Light from two collimated ultra-high-power LED (Prizmatix, UHP-T-520-EP) guides was focused on the ventral epicardial surface of the heart for excitation. Emitted fluorescence was collected using a tandem-lens arrangement of Nikon NIKKOR 50mm f/1.2 camera lenses and split with a 635 nm dichroic mirror (Edmund Optics, 87064).(41) The V_m signal was filtered at 690 ± 50 nm (Chroma ET690/50m), and a simultaneous brightfield image for vascular visualization and alignment was taken using the shorter-wavelength filtered light at 590 ± 33nm (Chroma ET590/33m). The emitted Vm signals and brightfield images (for vascular alignment) were recorded using 2 CMOS cameras (SciMedia, MiCAM N256) with a sampling rate of 1.03 kHz and 256 x 256 pixels with a 14 x 14 mm field of view. Pixel resolution of the images was approximately 55 x 55 µm. Data were acquired in 2-second intervals before and after addition of tyramine to the perfusate at a concentration of 5 µM. Data acquisition was done using BV Workbench software version 1.7.10 (SciMedia).

For conduction velocity analyses, epicardial pacing was performed from the basolateral LV wall at a cycle length (CL) of 167ms (with current of 1.1-1.3 mA and pulse width of 0.8 ms), using a Transonic Scisense 1.1F mouse EP catheter (FTS-1113A-0518). For analyses of tyramine effect on repolarization, pre- and post-tyramine time points were taken in sinus rhythm, just before heart rate increase, to allow comparison at the same CL (Figure 18).

Optical mapping data analysis

Optical mapping data was analyzed using the open-source software ElectroMap(20). V_m activation maps were displayed as isochronal maps generated from points of maximum upstroke $(dF/dt)_{max}$ as well as depolarization midpoint of optical APs. Repolarization maps were generated from points of APD_{80}. A minimum of 4 beats were averaged at baseline and after tyramine infusion. A 3x3 Gaussian spatial filter, Top-hat, and Savitzky-Golay filters were applied to correct for baseline drift and noise. Maps were exported as 256 x 256 data matrices for alignment with structural data and quantitative analyses.

Immunohistochemistry and tissue clearing

After optical mapping, whole mouse hearts were fixed by immersion in 4% paraformaldehyde/phosphate-buffered saline (PBS) overnight at 4°C, then washed three times for 1h in 0.01M PBS at room temperature (RT). Hearts were stained and cleared using a modified iDISCO protocol(42). Fixed hearts were dehydrated by graded methanol treatments (20%, 40%, 60%, and 80% methanol in H_2O (vol/vol), each for 1 h at RT), washed twice with 100% methanol for 1 h at RT, and chilled at 4°C. Hearts were then immersed in 66% dichloromethane/33% methanol overnight at RT with agitation, washed twice in 100% methanol for 1 h at RT, and chilled to 4°C. Next, hearts were bleached with 5% H_2O_2 in methanol (vol/vol) overnight at 4°C. After bleaching, hearts were rehydrated with graded methanol treatments, followed by one wash with 0.01 M PBS and 2 washes with 0.01 M PBS with 0.2% Triton X-100, each for 1 h at RT. Hearts were permeabilized with 0.01 M PBS with 0.2% Triton X-100, 20% DMSO, and 0.3 M glycine and blocked with 0.01 M PBS with 0.2% Triton X-100, 10% DMSO, and 5% normal donkey serum, each for 2 d at 37°C with agitation. Hearts were incubated in sheep anti-TH (EMD Millipore, AB1542, 1:200) and/or rabbit anti-periostin (Abcam, ab14041, 1:200) diluted in 0.01 M PBS with 0.2% Tween-20 and 10 mg/ml heparin (PTwH) for 5-7 days at 37°C with agitation. Hearts were then washed 4-5 times in PTwH overnight at RT before incubating in secondary antibodies donkey anti-rabbit Cy3 (Jackson ImmunoResearch, 711-165-152, 1:300) and/or donkey anti-sheep Alexa Fluor 647 (Jackson ImmunoResearch, 713-605-147, 1:300) diluted in PTwH for 5-7 days at 37°C with agitation. Primary and secondary Ab were replenished approximately halfway through incubation period. Hearts were then washed several times in PTwH overnight at room temperature. For clearing, stained hearts were dehydrated with a graded methanol series and incubated in 66% dichloromethane/33% methanol for 3 h at room temperature with agitation. Hearts were then washed twice in 100% dichloromethane for 15 min at room temperature. Hearts were stored in benzyl ether

(Millipore Sigma, 108014 ALDRICH; refractive index: 1.55) for up to 7 days prior to imaging.

Confocal imaging

Hearts were mounted in benzyl ether with adhesive plastic spacers (Sunjin Labs, IS012 and IS012). Images were acquired on a confocal laser scanning microscope (Zeiss, LSM 880) fitted with the following objectives: Fluar 5x/0.25 M27 Plan-Apochromat (working distance 12.5mm) and 10x/0.45 M27 (working distance 2.0 mm). Images were taken at both 5x and 10x magnifications for specific ROIs, such as RV and LV base, prior to the whole hearts being imaged at 5x in tiles with XY-resolution of 1.661μm and Z-resolution of 8.29μm.

Image processing and automated structural mapping

All image processing was performed using Zeiss Zen 2.1 v11, NIH ImageJ, Fiji(43), and custom Matlab scripts (available upon request from corresponding author). Computational tracing of nerve fibers was performed using a customized version of the open-source software neuTube(44). neuTube software was originally developed for tracing morphology of single cells. To trace nerves in large image volumes required additional pre- and post-processing including: (1) partitioning large volumes into smaller tiles, tracing each tile, and reassembling the traced morphologies, and (2) filtering out spurious junctions between parallel fibers and inaccurate fiber diameter estimates arising due to background staining. To quantify myofiber orientation distributions, we utilized confocal images of muscle autofluorescence. This was validated using comparison of autofluorescence with virally labeled myocyte imaging (Figure 8). We computed the image gradient orientation at each point and then smoothed the gradient orientation field using a Gaussian weighted moving average window of size σ=100μm.

Structural images were aligned to functional images using vascular fiducial points from brightfield images obtained during optical mapping. For each sample, 5-10 fiducial points (branches in vasculature, sutures or scars) visible in both brightfield optical mapping and confocal images were used to fit a perspective warping (homography) between the two images. Only structural data from the outer 100μm-thick "shell" of each heart were used for alignment and correlation with optical mapping data. This depth was determined empirically by light penetration experiments (Figure 9).

Quantitative data analysis

Conduction velocity and activation curves were calculated using ElectroMap.

Regional myofiber anisotropy was a normalized index defined as the coefficient of variation (angular standard deviation over the angular mean) of fiber angles, divided by the total surface area of the segmented ROI:

$$myofiber\ anisotropy\ index = \frac{\frac{angular\ standard\ deviation}{angular\ mean}}{ROI\ surface\ area}$$

Per prior reports(21–23), nerve fiber size bins were defined by the following diameters: small fibers = 1.2-3 μm, medium fibers = 3-5 μm, large fibers = 5-100 μm. 1.2μm was used as the lower limit of small fibers to minimize detection of non-specific background staining. Fiber prevalence was a normalized index defined as the proportion of a particular size fiber in a ROI, divided by the proportion of that fiber size in the whole heart:

$$fiber\ size\ prevalence\ index = \frac{percent\ of\ particular\ fiber\ size\ in\ ROI}{percent\ of\ same\ fiber\ size\ in\ whole\ heart}$$

Statistics

Data are presented as medians in figures, and sample sizes are indicated in figure legends or main text. All statistical analyses for comparison are indicated in figure legends or main text, were two-tailed, and were performed in Prism 9.0.2 (GraphPad).

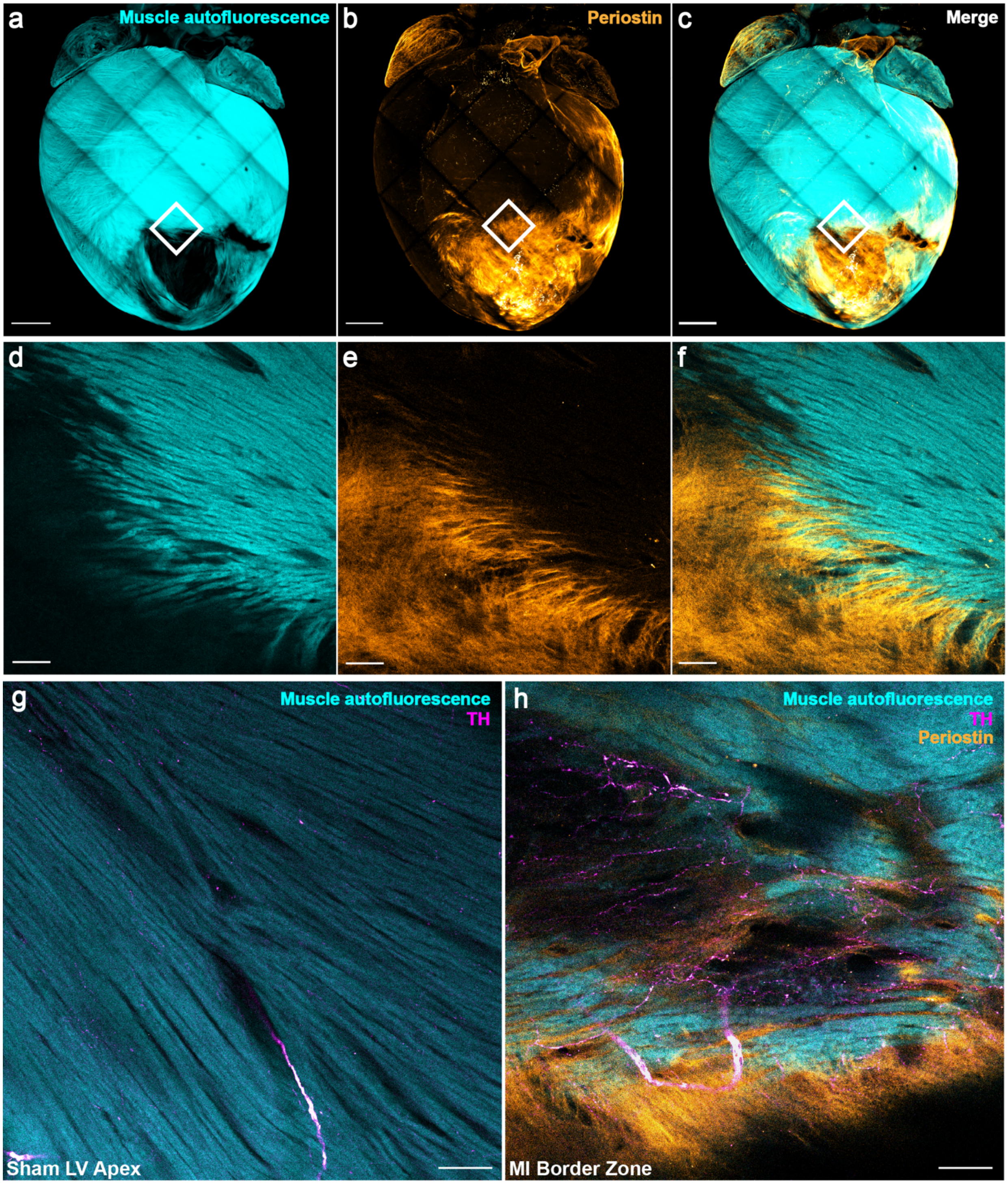

Figure 10. Validation of using autofluorescence to define dense scar versus surviving myocardium. Periostin (1:200, abcam, ab14041) staining of cleared chronic myocardial infarction heart imaged at 5X magnification **(a-c)** shows dense scar is visibly

devoid of muscle autofluorescence. Zoomed inset of the border zone (BZ) (10X magnification) **(d-f)** shows interdigitation of periostin-labeled scar with living muscle. In contrast to normal left ventricular apex **(g)**, infarct BZ at the interface of periostin with muscle autofluorescence demonstrates nerve sprouting **(h)**. All images are maximum intensity projections. TH = tyrosine hydroxylase. Scale bars are 1mm **(a-c)** and 100μm **(d-h)**.

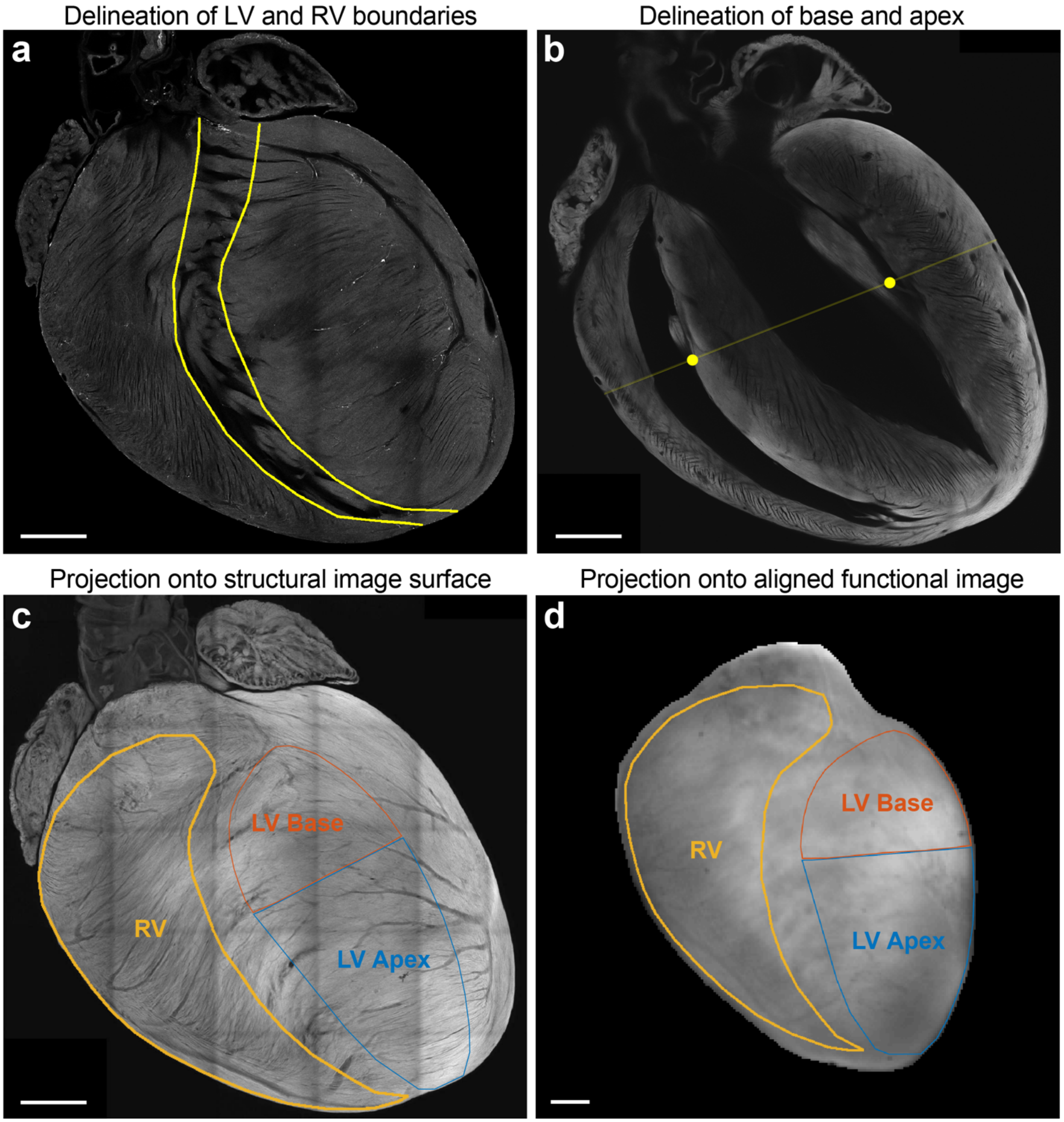

Figure 11. Defining regions of interest (ROIs) based on 3-dimensional anatomical landmarks. For consistency across hearts, ROIs were defined by anatomical landmarks in confocal microscopic image stacks of muscle autofluorescence in cleared hearts. Left ventricular (LV) and right ventricular (RV) boundaries were carefully delineated by exclusion of the ventricular septal trabeculations **(a)**. LV base and apex

were delineated by drawing a line between two points: the RV septal papillary-muscle-chordae-tendinae junction and the LV anterolateral papillary-chordae junction **(b)**. All myocardial infarction border zone and dense scar regions in analyzed hearts were visually confirmed to be below this line. These delineations were then projected onto the structural image surface of the heart **(c)**, which, when aligned by vascular fiducials with the brightfield optical image **(d)**, allowed projection of the ROIs onto the functional electrical maps. Scale bars are all 1mm.

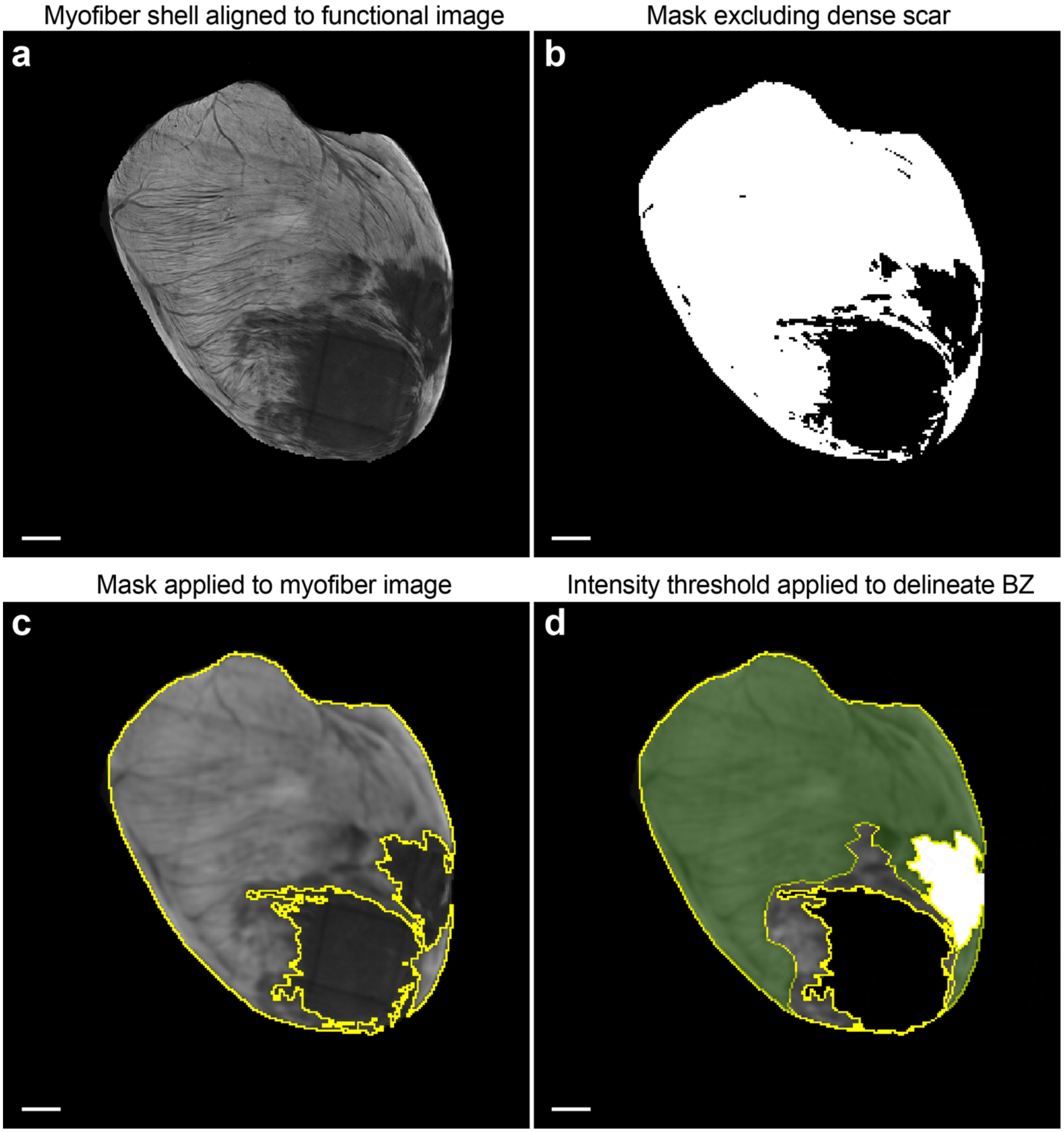

Figure 12. Defining border zone and dense scar based on myofiber imaging. To maintain structural consistency in border zone (BZ) definition across infarcted hearts, 16-bit maximum intensity projection images of 100µm-thick epicardial shells were created **(a)**, and a mask was applied to define regions with <100µm-thick surviving myocardium as dense scar **(b)**. A 2x2 pixel Gaussian blur was then applied to the

remaining surviving myocardial image **(c)**, and a threshold was applied at half the maximal fluorescence intensity of the image to define the BZ. Panel **(d)** shows the resulting segmentation, where the region in green is surviving myocardium above the fluorescence intensity threshold, the region in gray is below the threshold and thus defined as BZ, the dense scar is in black, and the location of the coronary ligature is in white (also excluded from quantitative analyses). All scale bars are 1mm.

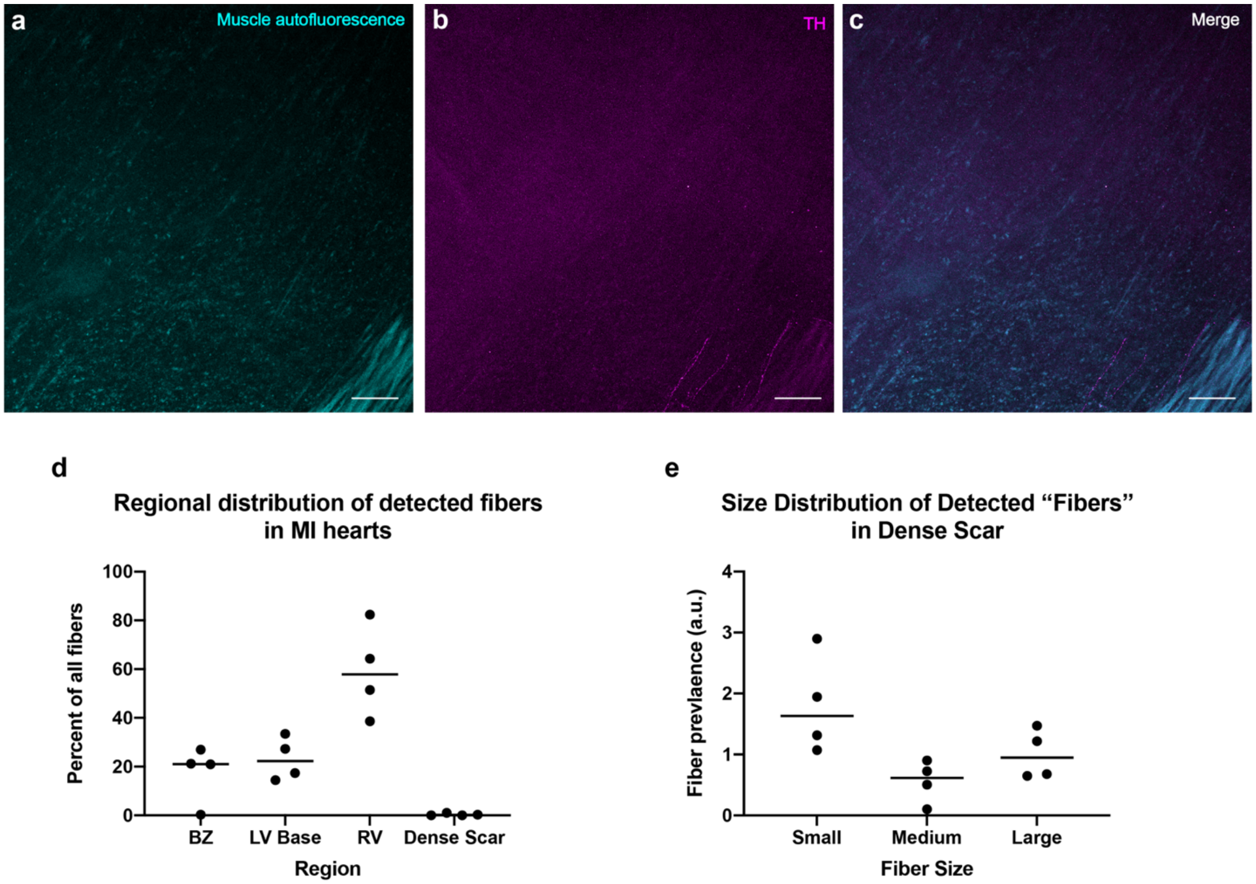

Figure 13. Dense scar structural data. We excluded regions of dense scar as defined in Figure 12 from our quantitative structural analyses due to the negligible amount of living muscle and nerve fibers detected in these regions, as shown qualitatively by immunofluorescence in 4 cleared infarcted hearts **(a-b)** and quantitatively by automated nerve fiber detection **(d)**. The relative predominance of "small fibers" in dense scar **(e)** possibly reflects detection of background or artifactual signal. Scale bars in **(a-c)** are 100μm. TH=tyrosine hydroxylase. a.u. = arbitrary units.

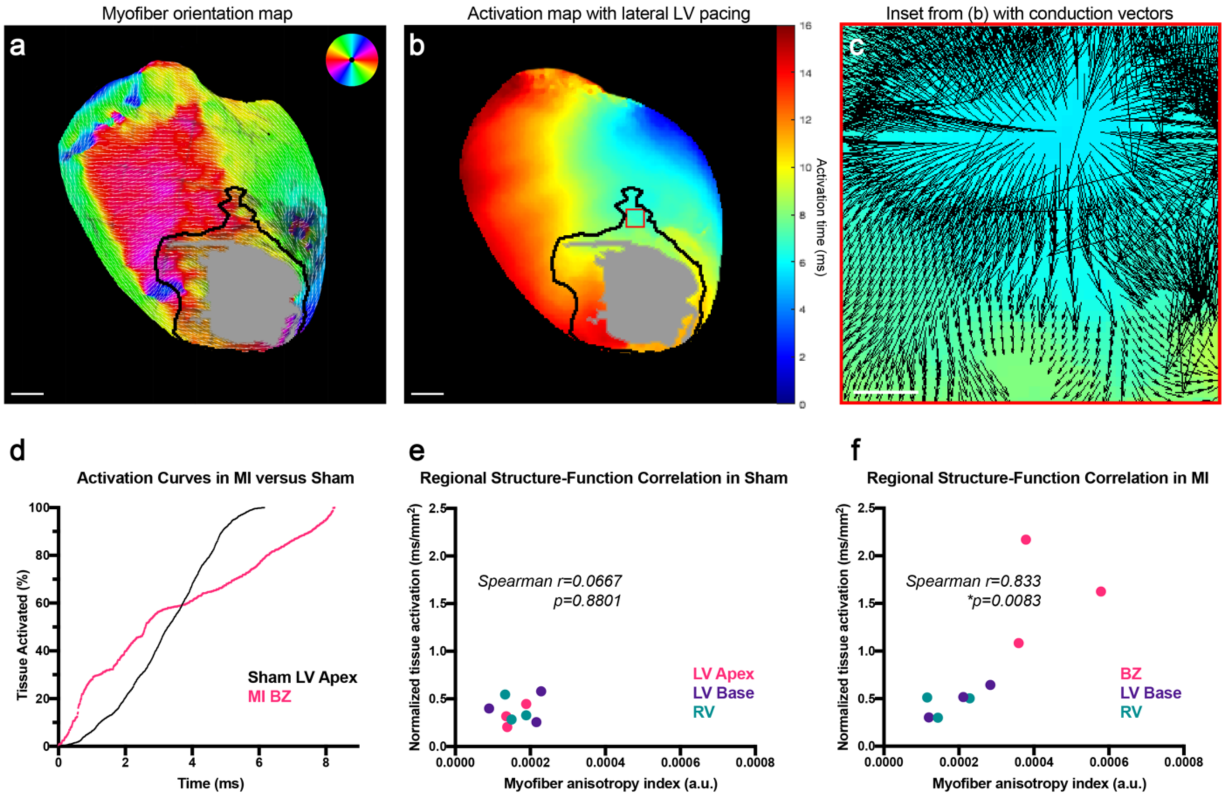

Figure 14. A composite metric of myofiber anisotropy and tissue activation defines infarct border zones. **(a)** Color-coded myofiber orientation map from chronic myocardial infarction (MI) heart with black line delineating border zone (BZ) and gray patch delineating dense scar. Dark patch on LV lateral wall is location of coronary ligature, which was excluded from quantitative analyses. Atria were cropped from image for ease of interpretation. **(b)** Activation map from same chronic MI heart with dense scar region defined by gray patch and BZ delineated by black line. **(c)** Zoomed inset from activation map with overlay of conduction velocity vectors showing discontinuous propagation. **(d)** Representative tissue activation curves from anatomically defined LV apex region of sham heart (black) versus infarct BZ region (magenta), showing isotropic conduction versus anisotropic and conduction block. **(e, f)** Plots of regional myofiber anisotropy indices versus normalized tissue activation times, showing no correlation in

Sham (Spearman r=0.0667, p=0.8801, n=9 regions from 3 mice) versus positive correlation in MI (Spearman r=0.833, p=0.0083, n=9 regions from 3 mice). Scale bars are 1mm (**a, b**) and 100µm (**c**). a.u. = arbitrary units.

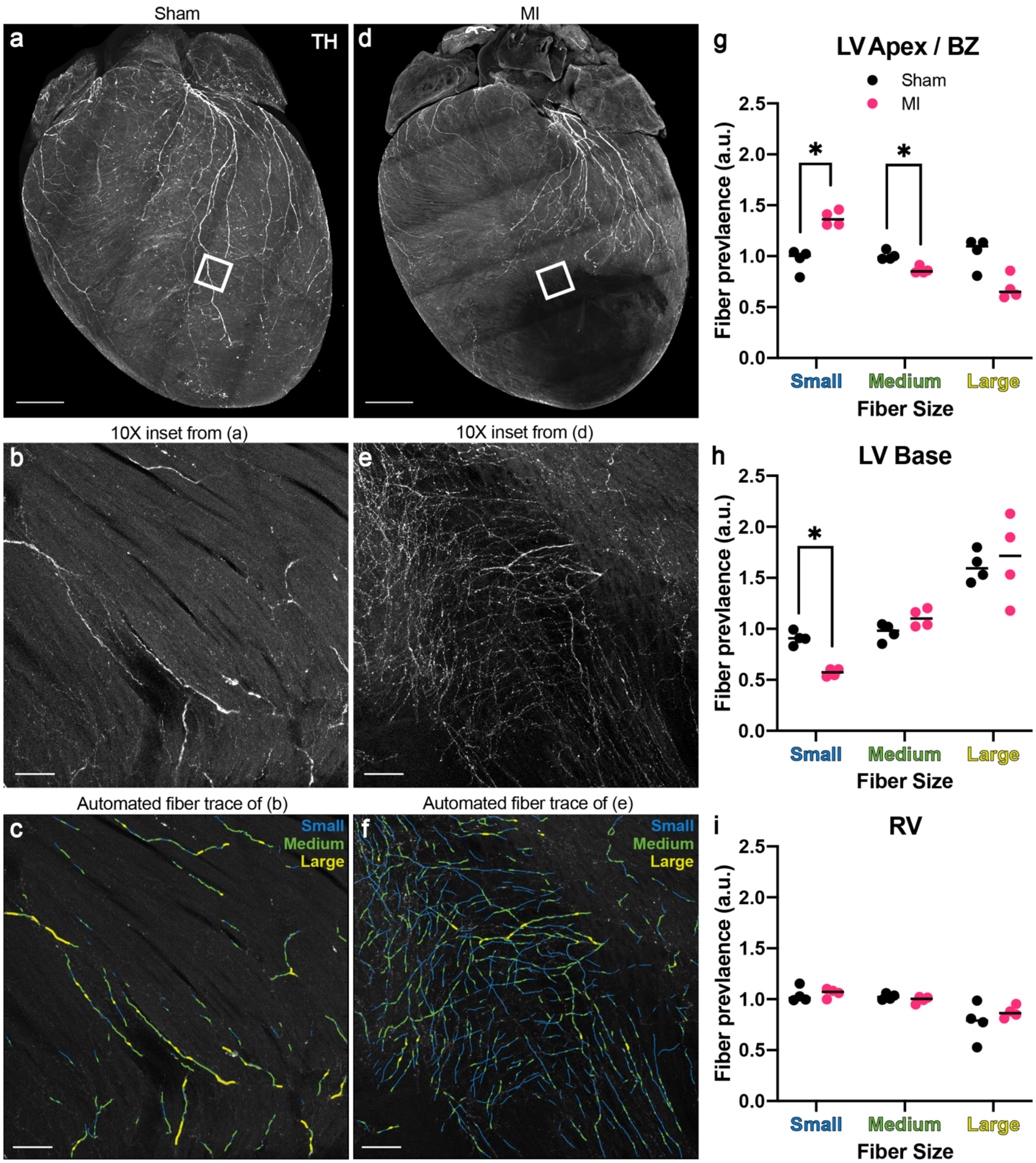

Figure 15. Altered distribution of neuroeffector endings after myocardial infarction (MI). (a) Maximum intensity projection (MIP) confocal image of global tyrosine hydroxylase (TH) staining of sham heart (same heart MIP was originally shown in Figure 1D for methodological demonstration purposes). **(b, c)** Representative 10X

inset from sham left ventricle (LV) showing TH staining and automated fiber tracing, binned by small (1.2-3µm), medium (3-5µm), and large (5-100µm) diameters. **(d)** MIP confocal image of global TH staining in MI heart, previously. **(e, f)** Representative 10X inset from border zone (BZ) showing TH staining and automated fiber tracing, binned by small (1.2-3µm), medium (3-5µm), and large (5-100µm) diameters. **(g-i)** Regional comparisons of fiber size prevalence between sham (black) and MI (magenta), with black lines denoting medians and asterisks denoting statistical significance (*= Mann-Whitney, p=0.0286, n=4 mice per group). Scale bars are 1mm (**a, d**) and 100µm (**b, c, e, f**). RV=right ventricle. a.u.=arbitrary units.

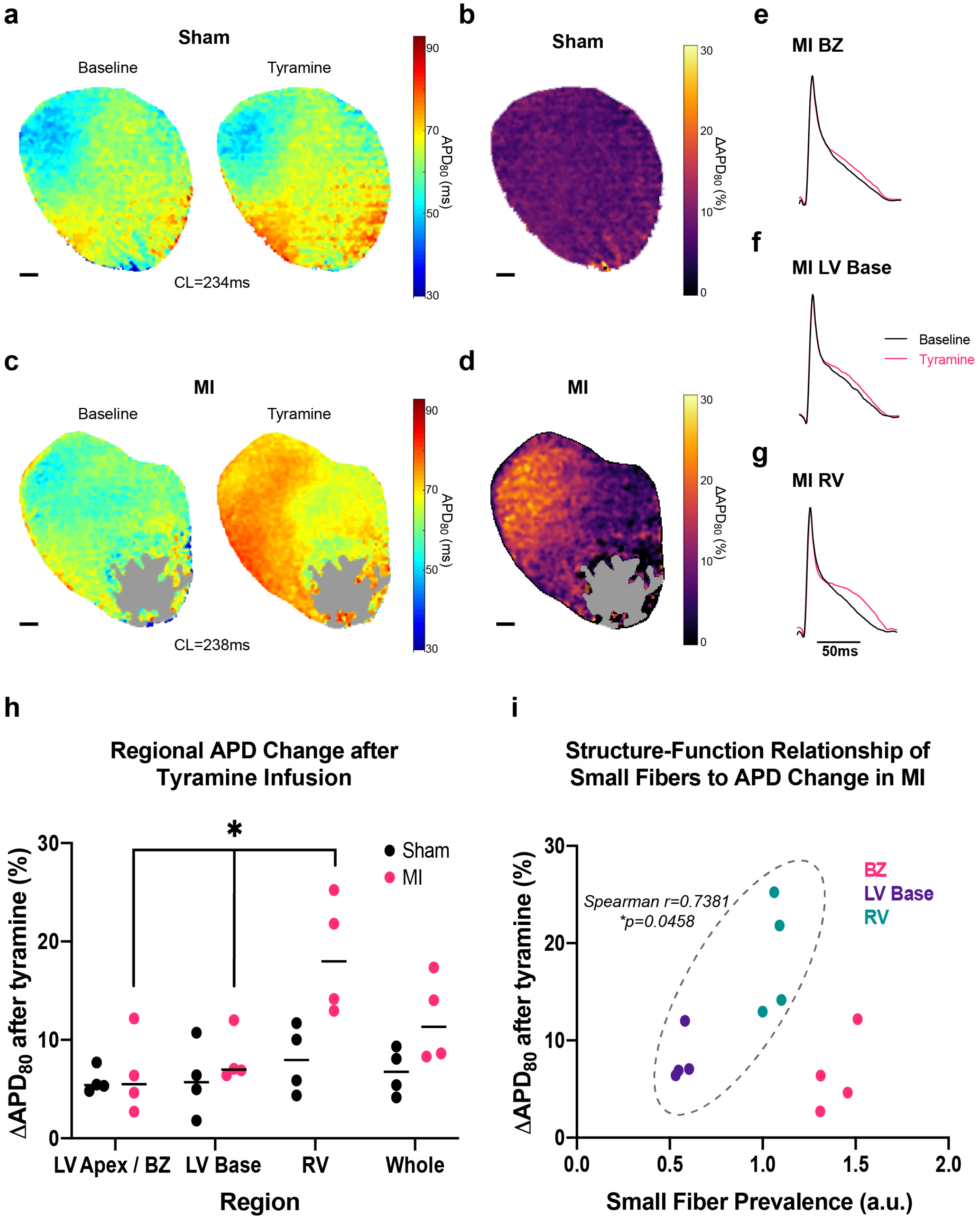

Figure 16. Altered neuroeffector distribution underlies perturbed myocardial

sympathetic control after chronic infarction. (a) Eighty percent of action potential duration (APD_{80}) maps of representative sham heart at baseline and after infusion of 5 μM tyramine. **(b)** Change in APD_{80} (ΔAPD_{80}) map of sham heart. **(c)** APD_{80} maps of representative MI heart at baseline and after infusion of 5 μM tyramine. Gray region denotes dense scar. **(d)** ΔAPD_{80} map of MI heart. **(e-g)** Representative action potentials at baseline (black) and after tyramine (magenta) in anatomically segmented regions of MI heart. **(h)** Comparison of regional, tyramine-mediated changes in APD_{80} between sham and MI hearts, with MI heart showing significant regional variation in tyramine effect (*=Kruskal-Wallis p=0.0132, n=4 mice per group) while Sham heart showed no significant regional variation (Kruskal Wallis p=0.7463, n=4 mice per group). **(i)** Plot of regional small fiber prevalence in MI hearts versus tyramine-mediated APD change, with positive correlation in left ventricular (LV) base and right ventricular (RV) regions (Spearman r=0.7381, p=0.0458, n=8 regions from 4 mice) but no correlation when border zone (BZ) is included (Spearman r=0.021, p=0.956, n=12 regions from 4 mice). Scale bars are 1mm (**a-d**). a.u.=arbitrary units.

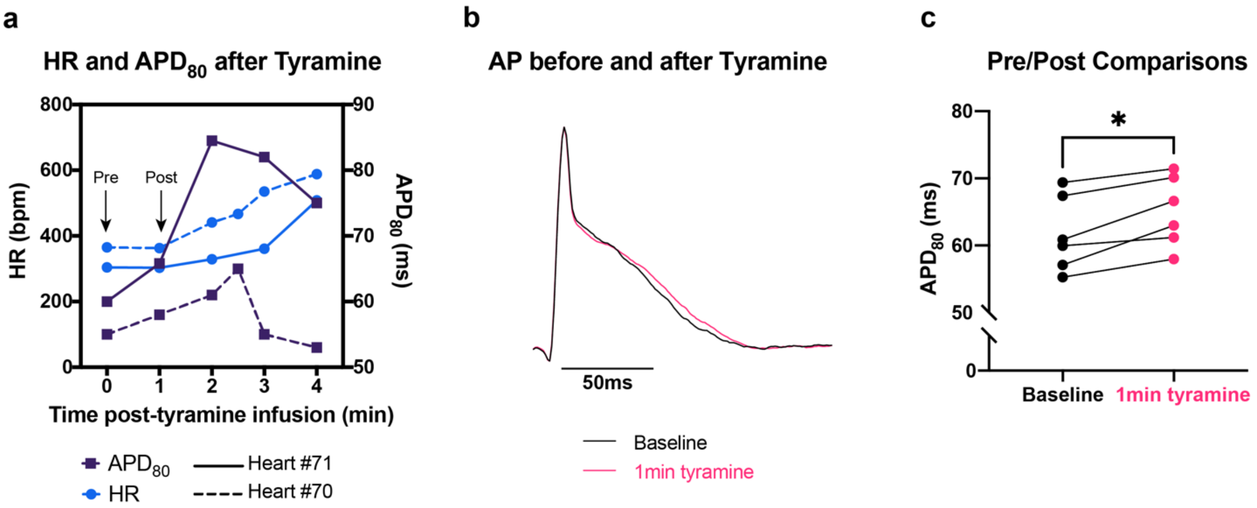

Figure 17. Validating choice of pre- and post- tyramine time points for action potential duration (APD) analyses. To avoid potentially confounding neuromodulatory effects of pacing, we chose to analyze tyramine-mediated APD changes in sinus rhythm. We found that in all our ventricular APD maps, there was a global increase in 80% of APD (APD80) prior to an increase in heart rate (HR), at approximately 1 minute after 5 µM tyramine infusion, with representative data shown in **(a)** and **(b)**. This increase suggests that tyramine has a myocardial effect prior to its nodal effect and was statistically significant across all the sham hearts we mapped for this study **(c)** (Wilcoxon p=0.0312, n=6 mice). Thus we defined pre- and post- tyramine timepoints of APD analyses as immediately before, and approximately 1 minute following, the start of tyramine infusion, just prior to HR increase.

REFERENCES

1. Zipes DP, Wellens HJ. Sudden cardiac death. Circulation 1998;98:2334–2351.

2. Chugh SS, Reinier K, Teodorescu C, et al. Epidemiology of sudden cardiac death: clinical and research implications. Prog Cardiovasc Dis 2008;51:213–228.

3. El-Sherif N, Scherlag B J, Lazzara R, Hope R R. Re-entrant ventricular arrhythmias in the late myocardial infarction period. 1. Conduction characteristics in the infarction zone. Circulation 1977;55:686–702.

4. Peters NS, Coromilas J, Severs NJ, Wit AL. Disturbed connexin43 gap junction distribution correlates with the location of reentrant circuits in the epicardial border zone of healing canine infarcts that cause ventricular tachycardia. Circulation 1997;95:988–996.

5. Kléber AG, Rudy Y. Basic mechanisms of cardiac impulse propagation and associated arrhythmias. Physiol. Rev. 2004;84:431–488.

6. Vaseghi M, Shivkumar K. The role of the autonomic nervous system in sudden cardiac death. Prog Cardiovasc Dis 2008;50:404–419.

7. Shen MJ, Zipes DP. Role of the autonomic nervous system in modulating cardiac arrhythmias. Circ. Res. 2014;114:1004–1021.

8. Rajendran PS, Nakamura K, Ajijola OA, et al. Myocardial infarction induces structural and functional remodelling of the intrinsic cardiac nervous system. J. Physiol. (Lond.) 2016;594:321–341.

9. Yokoyama T, Lee J-K, Miwa K, et al. Quantification of sympathetic hyperinnervation and denervation after myocardial infarction by three-dimensional assessment of the

cardiac sympathetic network in cleared transparent murine hearts. PLoS ONE 2017;12:e0182072.

10. Ajijola OA, Yagishita D, Patel KJ, et al. Focal myocardial infarction induces global remodeling of cardiac sympathetic innervation: neural remodeling in a spatial context. Am J Physiol Heart Circ Physiol 2013;305:H1031-1040.

11. Ajijola OA, Lux RL, Khahera A, et al. Sympathetic modulation of electrical activation in normal and infarcted myocardium: implications for arrhythmogenesis. Am J Physiol Heart Circ Physiol 2017;312:H608–H621.

12. Cao JM, Chen LS, KenKnight BH, et al. Nerve sprouting and sudden cardiac death. Circ. Res. 2000;86:816–821.

13. Vracko R, Thorning D, Frederickson RG. Nerve fibers in human myocardial scars. Hum. Pathol. 1991;22:138–146.

14. Cao JM, Fishbein MC, Han JB, et al. Relationship between regional cardiac hyperinnervation and ventricular arrhythmia. Circulation 2000;101:1960–1969.

15. Tapa S, Wang L, Francis Stuart SD, et al. Adrenergic supersensitivity and impaired neural control of cardiac electrophysiology following regional cardiac sympathetic nerve loss. Scientific Reports 2020;10:18801.

16. Ng GA, Mantravadi R, Walker WH, et al. Sympathetic nerve stimulation produces spatial heterogeneities of action potential restitution. Heart Rhythm 2009;6:696–706.

17. Mantravadi R, Gabris B, Liu T, et al. Autonomic nerve stimulation reverses ventricular repolarization sequence in rabbit hearts. Circ Res 2007;100:e72-80.

18. Ng GA, Brack KE, Patel VH, Coote JH. Autonomic modulation of electrical restitution, alternans and ventricular fibrillation initiation in the isolated heart. Cardiovasc Res 2007;73:750–760.

19. Ng GA, Brack KE, Coote JH. Effects of direct sympathetic and vagus nerve stimulation on the physiology of the whole heart--a novel model of isolated Langendorff perfused rabbit heart with intact dual autonomic innervation. Exp Physiol 2001;86:319–329.

20. O'Shea C, Holmes AP, Yu TY, et al. ElectroMap: High-throughput open-source software for analysis and mapping of cardiac electrophysiology. Scientific Reports 2019;9:1389.

21. Siegel A, Sapru HN. Essential Neuroscience. Lippincott Williams & Wilkins; 2006.

22. Falck B, Torp A. New evidence for the localization of noradrenalin in the adrenergic nerve terminals. Med Exp Int J Exp Med 1962;6:169–172.

23. Prando V, Da Broi F, Franzoso M, et al. Dynamics of neuroeffector coupling at cardiac sympathetic synapses. J Physiol 2018;596:2055–2075.

24. Wang L, Morotti S, Tapa S, et al. Different paths, same destination: divergent action potential responses produce conserved cardiac fight-or-flight response in mouse and rabbit hearts. J Physiol 2019;597:3867–3883.

25. Rutherford SL, Trew ML, Sands GB, LeGrice IJ, Smaill BH. High-resolution 3-dimensional reconstruction of the infarct border zone: impact of structural remodeling on electrical activation. Circ Res 2012;111:301–311.

26. Wu TJ, Ong JJ, Hwang C, et al. Characteristics of wave fronts during ventricular fibrillation in human hearts with dilated cardiomyopathy: role of increased fibrosis in the generation of reentry. J Am Coll Cardiol 1998;32:187–196.

27. Anderson KP, Walker R, Urie P, Ershler PR, Lux RL, Karwandee SV. Myocardial electrical propagation in patients with idiopathic dilated cardiomyopathy. J Clin Invest 1993;92:122–140.

28. de Bakker JM, Coronel R, Tasseron S, et al. Ventricular tachycardia in the infarcted, Langendorff-perfused human heart: role of the arrangement of surviving cardiac fibers. J Am Coll Cardiol 1990;15:1594–1607.

29. Saba S, Mathier MA, Mehdi H, et al. Dual-dye optical mapping after myocardial infarction: does the site of ventricular stimulation alter the properties of electrical propagation? J Cardiovasc Electrophysiol 2008;19:197–202.

30. Li W, Knowlton D, Van Winkle DM, Habecker BA. Infarction alters both the distribution and noradrenergic properties of cardiac sympathetic neurons. Am J Physiol Heart Circ Physiol 2004;286:H2229-2236.

31. Olivas A, Gardner RT, Wang L, Ripplinger CM, Woodward WR, Habecker BA. Myocardial Infarction Causes Transient Cholinergic Transdifferentiation of Cardiac Sympathetic Nerves via gp130. J Neurosci 2016;36:479–488.

32. Pianca N, Di Bona A, Lazzeri E, et al. Cardiac sympathetic innervation network shapes the myocardium by locally controlling cardiomyocyte size through the cellular proteolytic machinery. J Physiol 2019;597:3639–3656.

33. Vaseghi M, Lux RL, Mahajan A, Shivkumar K. Sympathetic stimulation increases dispersion of repolarization in humans with myocardial infarction. Am. J. Physiol. Heart Circ. Physiol. 2012;302:H1838-1846.

34. Zhou S, Chen LS, Miyauchi Y, et al. Mechanisms of cardiac nerve sprouting after myocardial infarction in dogs. Circ. Res. 2004;95:76–83.

35. Schroeder C, Jordan J. Norepinephrine transporter function and human cardiovascular disease. Am J Physiol Heart Circ Physiol 2012;303:H1273-1282.

36. Tomek J, Hao G, Tomková M, et al. β-Adrenergic Receptor Stimulation and Alternans in the Border Zone of a Healed Infarct: An ex vivo Study and Computational Investigation of Arrhythmogenesis. Front Physiol 2019;10:350.

37. Billman GE, Castillo LC, Hensley J, Hohl CM, Altschuld RA. Beta2-adrenergic receptor antagonists protect against ventricular fibrillation: in vivo and in vitro evidence for enhanced sensitivity to beta2-adrenergic stimulation in animals susceptible to sudden death. Circulation 1997;96:1914–1922.

38. Fernández B, Durán AC, Fernández MC, Fernández-Gallego T, Icardo JM, Sans-Coma V. The coronary arteries of the C57BL/6 mouse strains: implications for comparison with mutant models. J Anat 2008;212:12–18.

39. Lang D, Sulkin M, Lou Q, Efimov IR. Optical Mapping of Action Potentials and Calcium Transients in the Mouse Heart. J Vis Exp 2011. Available at: https://www.ncbi.nlm.nih.gov/pmc/articles/PMC3230201/. Accessed August 17, 2020.

40. Gloschat C, Aras K, Gupta S, et al. RHYTHM: An Open Source Imaging Toolkit for Cardiac Panoramic Optical Mapping. Sci Rep 2018;8:2921.

41. Cathey B, Obaid S, Zolotarev AM, et al. Open-Source Multiparametric Optocardiography. Sci Rep 2019;9:721.

42. Renier N, Wu Z, Simon DJ, Yang J, Ariel P, Tessier-Lavigne M. iDISCO: a simple, rapid method to immunolabel large tissue samples for volume imaging. Cell 2014;159:896–910.

43. Schindelin J, Arganda-Carreras I, Frise E, et al. Fiji: an open-source platform for biological-image analysis. Nat Methods 2012;9:676–682.

44. Feng L, Zhao T, Kim J. neuTube 1.0: A New Design for Efficient Neuron Reconstruction Software Based on the SWC Format. eNeuro 2015;2.

Chapter 4:

Conclusions and Future Directions

Conclusions

Taken together, these data generated from our novel platform for structure-function alignment establish an important framework for understanding how structural cardiac diseases such as MI perturb specific myocardial electrical functions, as well as the neural substrates and mechanisms which control these functions. While most of the existing neurocardiac literature focuses on molecular and cellular alterations in arrhythmogenic heart disease(1–6), current clinical therapies for arrhythmia actually depend heavily on anatomical substrate modification(7) and neuromodulation at multiple structures of the autonomic nervous system(8). These therapies have benefited greatly from advancements in clinical imaging(9) to localize potential arrhythmogenic substrates, yet spatially correlating these substrates to their functional roles remains an important challenge. Thus, our study addresses the crucial need to understand post-MI neurocardiac dynamics at the whole-organ level, while still offering the high spatial resolution necessary to target the microstructural features underlying arrhythmogenic processes.

Future Directions

Overall, the synergistic neural-myocardial framework we present in this study is vitally important to elucidating the pathophysiology leading to sudden cardiac death. The distinct functional profile of nerve sprouts we identified in this study gives rise to several mechanistic hypotheses regarding the neurobiology and physiology of these structures. It is possible that the axonal nerve sprouts at the BZ have defective NET function or defective vesicular release function at their neuroeffector synapses.

Our approach to structure-function alignment could feasibly incorporate emerging technologies, such as spatial detection of interstitial neurotransmitter levels with fast-scanning cyclic voltammetry(10) and optical norepinephrine tracers(11), to generate additional mechanistic insights. Ultimately, a combination of such techniques will be needed to enable the development of more powerful and targeted neuromodulatory therapies for heart disease. Our ongoing studies seek to (1) probe synaptic release activity at the infarct BZ and (2) experimentally perturb BZ axon remodeling.

Assays of Synaptic Release Activity at the Infarct Border Zone

One follow-up study that is ongoing is assaying catecholaminergic neurotransmitter release at the BZ. Currently we are pursuing adapting fast-scanning cyclic voltammetry (FSCV) for use in real-time detection of regional norepinephrine release in the mouse heart. This method utilizes electrodes to detect alterations in norepinephrine and epinephrine levels and has already been used in porcine studies of myocardial infarction (10, 12).

Another method of probing BZ neurophysiology is the use of active synaptic mapping via optical techniques. Genetically encoded calcium sensors such as calcium-modulated photoactivatable ratiometric integrator (CAMPARI) allow mapping of active neurons and synapses (13, 14). These tools are able to be transfected into neural tissue utilizing adeno-associated viral (AAV) vectors. Though previously used in the central nervous system, we plan to adapt this tool for peripheral nervous system delivery using an engineered AAV serotype previously validated for this purpose (15)

Experimental Perturbation of Nerve Sprouting: Mechanisms of Sympathetic Axon Patterning and Arrhythmogenesis

One potential method of understanding sympathetic axon function at the infarct BZ is to perturb the patterning of these axons after ischemic injury. We are investigating developmental pathways of sympathetic axon guidance so that they can potentially be leveraged in the post-MI disease process of sympathetic axon sprouting and remodeling. One such pathway of interest that has previously been implicated in arrhythmogenesis is the semaphorin (Sema)-plexin (Plxn) signaling pathway (16).

Sema3a, which signals primarily through PlxnA3 and PlxnA4, is primarily responsible for sympathetic innervation of the heart during development (17). This pathway has been shown to regulate heart rate (16) as well as play a role in sudden cardiac death syndromes (18, 19). Unfortunately, the Sema3a-knockout (Sema3a KO) mouse is difficult to study due to the lethality of the mutation (16, 20).

We recently obtained an alternative model of perturbed Sema-Plxn signaling that is viable and has a similar cardiac phenotype with Sema3a KO mice – PlxnA3/PlxnA4 KO mice (21). In preliminary studies, we have observed these mice to have perturbed sympathetic patterning of the ventricular myocardium (Figure 18). Continuous ECG telemetry recordings in these mice (while conscious and freely moving) reveal potentially decreased baseline sympathetic tone, as they have lower baseline heart rate and blunted response to propranolol, as well as possible denervation supersensitivity with exaggerated response to isoproterenol (Table 2). These mice may also have increased arrhythmic susceptibility (Figure 19). Interestingly, PlxnA3/A4 KO mice likely have structurally normal hearts on echocardiography (Table 3), which could point to a purely neural basis for arrhythmogenesis. Ultimately, we hope to use mouse models of altered cardiac neural patterning to gain a deeper understanding of arrhythmogenic consequences, which can be leveraged for attenuating MI pathophysiology.

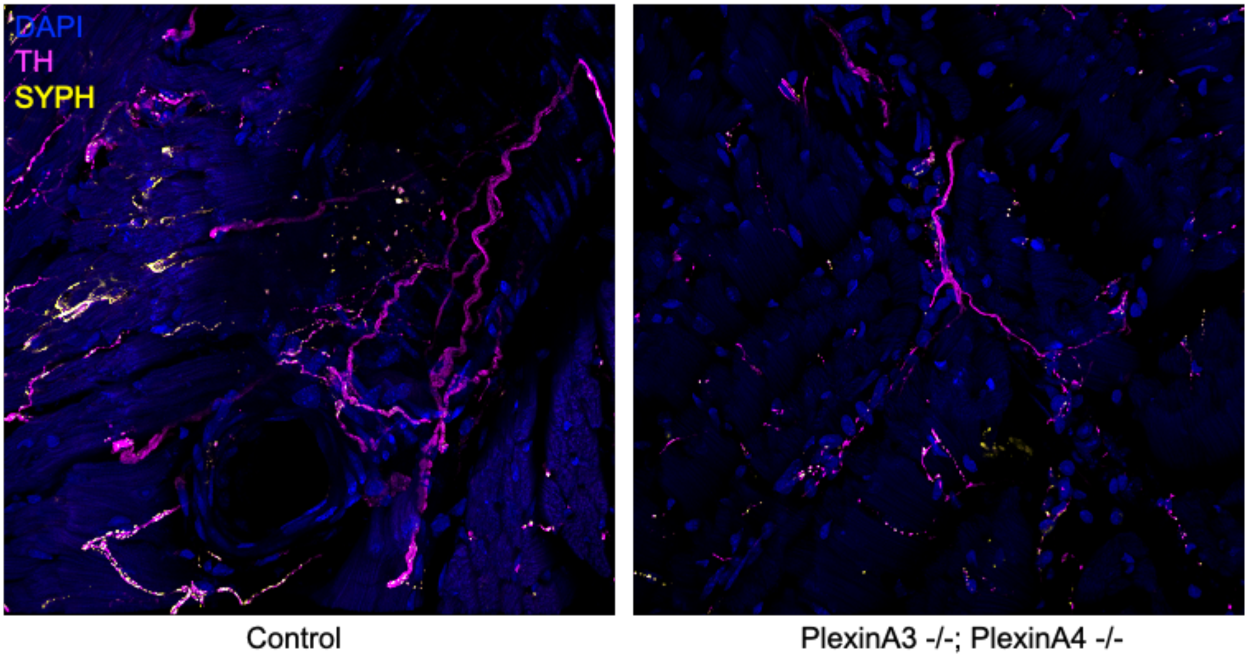

Figure 18. PlexinA3/A4 mutants have abnormal sympathetic patterning of the heart. Histological sections of left ventricular tissue demonstrate altered sympathetic patterning in plexin double mutant versus control littermate. Preliminary data from Takako Makita.

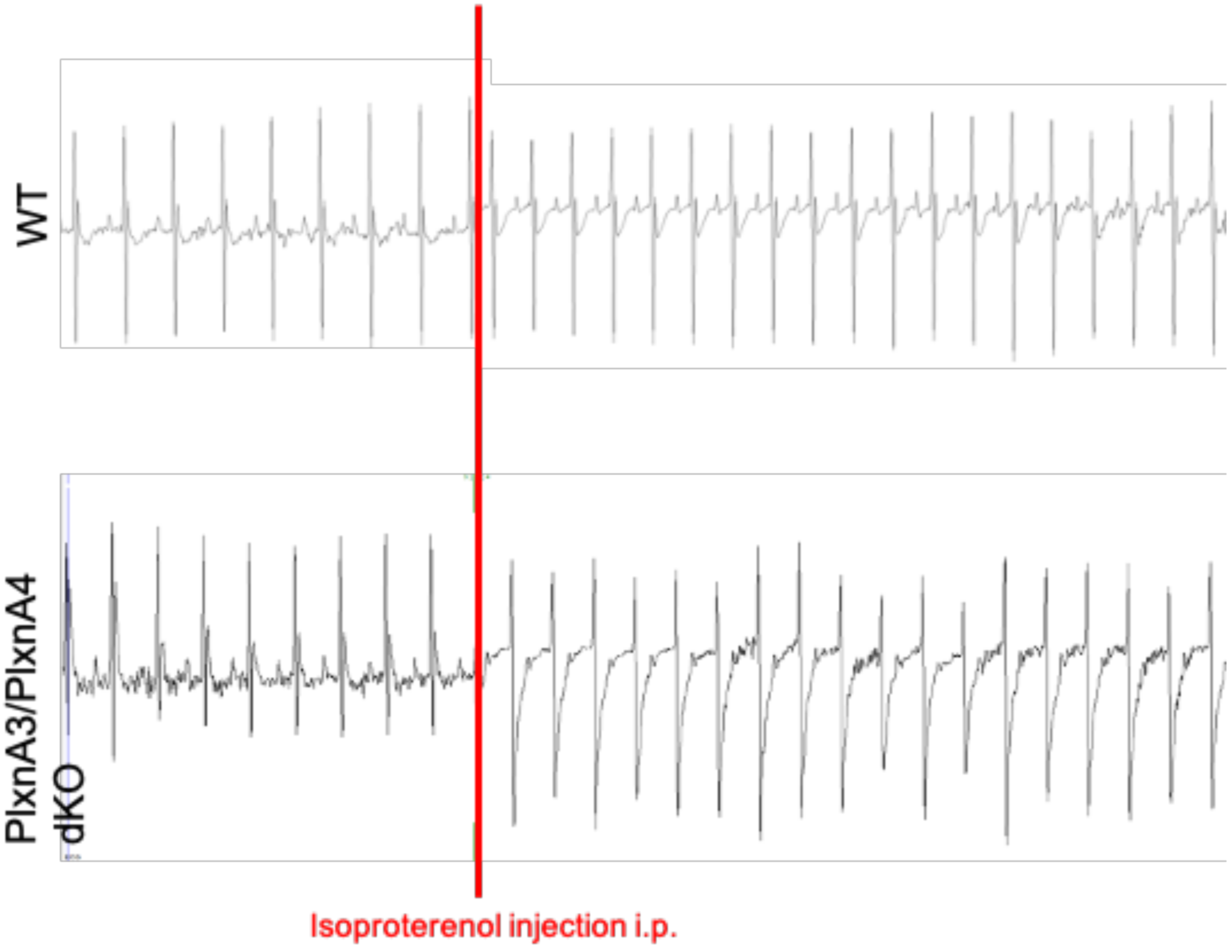

Figure 19. PlexinA3/A4 mutants have increased susceptibility to ventricular arrhythmia. Continuous telemetric ECG in conscious, freely moving mice with double plexin mutations reveals inducible ventricular arrhythmia with isoproterenol injection (1mg/kg i.p.). In contrast, sinus tachycardia is expectedly induced in control mouse.

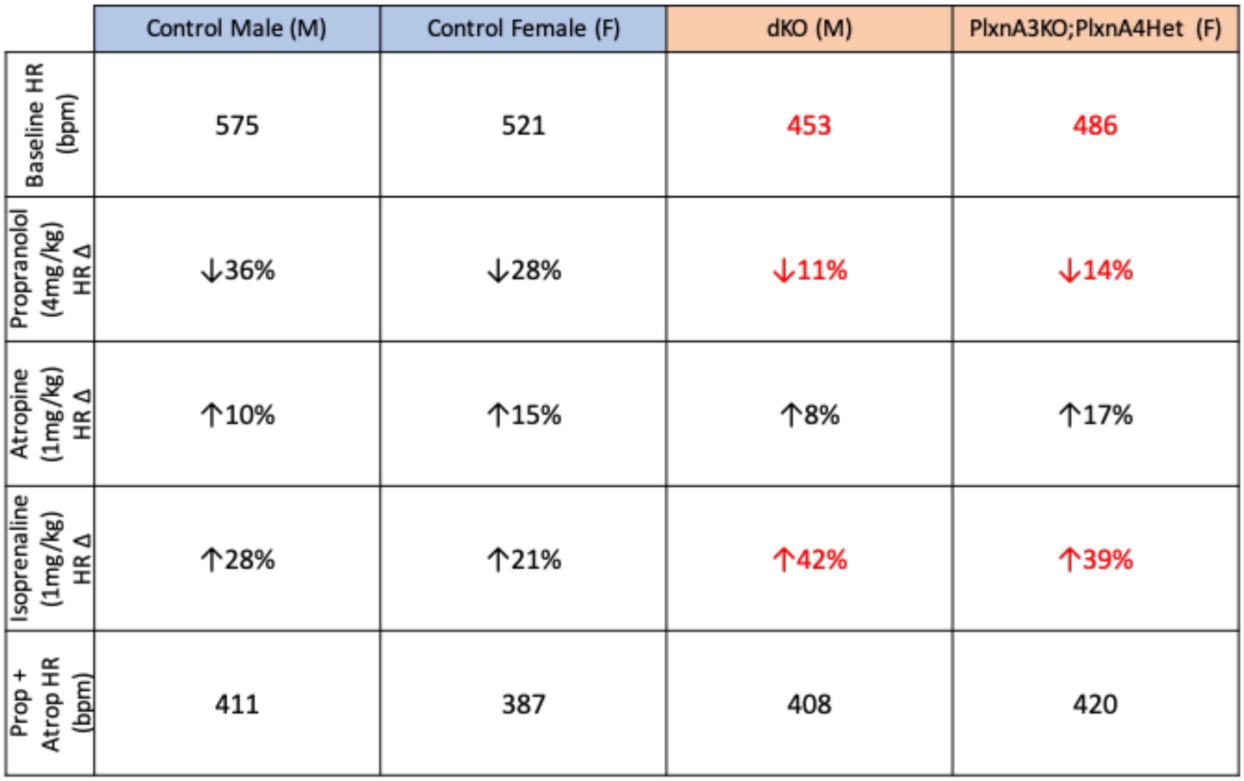

	Control Male (M)	Control Female (F)	dKO (M)	PlxnA3KO;PlxnA4Het (F)
Baseline HR (bpm)	575	521	453	486
Propranolol (4mg/kg) HR Δ	↓36%	↓28%	↓11%	↓14%
Atropine (1mg/kg) HR Δ	↑10%	↑15%	↑8%	↑17%
Isoprenaline (1mg/kg) HR Δ	↑28%	↑21%	↑42%	↑39%
Prop + Atrop HR (bpm)	411	387	408	420

Table 2. Baseline heart rates and responses to neuromodulatory drugs in control and plexin-mutant mice. M=male, F=female.

	Control Male (M)	Control Female (F)	dKO (M)	dKO (F)
LVEF (%)	57	64	61	56
LV Vol;d (uL)	77.6	95.8	96.5	85.9
LVPW;d (mm)	0.82	0.71	0.69	0.73

Table 3. Echocardiographic measurements in control and plexin-mutant mice. M=male, F=female, LVEF = left ventricular ejection fraction, LV Vol; d = diastolic LV volume, LVPW;d = LV posterior wall diastolic thickness.

References

1. Bristow MR, Ginsburg R, Umans V, et al. Beta 1- and beta 2-adrenergic-receptor subpopulations in nonfailing and failing human ventricular myocardium: coupling of both receptor subtypes to muscle contraction and selective beta 1-receptor down-regulation in heart failure. Circ Res 1986;59:297–309.

2. Harvey RD, Hume JR. Autonomic regulation of a chloride current in heart. Science 1989;244:983–985.

3. Billman GE, Castillo LC, Hensley J, Hohl CM, Altschuld RA. Beta2-adrenergic receptor antagonists protect against ventricular fibrillation: in vivo and in vitro evidence for enhanced sensitivity to beta2-adrenergic stimulation in animals susceptible to sudden death. Circulation 1997;96:1914–1922.

4. Tomek J, Hao G, Tomková M, et al. β-Adrenergic Receptor Stimulation and Alternans in the Border Zone of a Healed Infarct: An ex vivo Study and Computational Investigation of Arrhythmogenesis. Front Physiol 2019;10:350.

5. Harvey RD, Belevych AE. Muscarinic regulation of cardiac ion channels. Br J Pharmacol 2003;139:1074–1084.

6. Habecker BA, Anderson ME, Birren SJ, et al. Molecular and cellular neurocardiology: development, and cellular and molecular adaptations to heart disease. The Journal of Physiology 2016;594:3853–3875.

7. Shivkumar K. Catheter Ablation of Ventricular Arrhythmias. N Engl J Med 2019;380:1555–1564.

8. Zhu C, Hanna P, Rajendran PS, Shivkumar K. Neuromodulation for Ventricular Tachycardia and Atrial Fibrillation: A Clinical Scenario-Based Review. JACC Clin Electrophysiol 2019;5:881–896.

9. Kung GL, Ajijola O, Ramirez RJ, et al. Microstructural remodeling in the post-infarct porcine heart measured by diffusion tensor MRI and T1-weighted late gadolinium enhancement MRI. J Cardiovasc Magn Reson 2012;14:P66.
10. Chan S-A, Vaseghi M, Kluge N, Shivkumar K, Ardell JL, Smith C. Fast in vivo detection of myocardial norepinephrine levels in the beating porcine heart. Am J Physiol Heart Circ Physiol 2020;318:H1091–H1099.
11. Dunn M, Henke A, Clark S, et al. Designing a norepinephrine optical tracer for imaging individual noradrenergic synapses and their activity in vivo. Nat Commun 2018;9:2838.
12. Hadaya J, Buckley U, Gurel NZ, et al. Scalable and reversible axonal neuromodulation of the sympathetic chain for cardiac control. American Journal of Physiology-Heart and Circulatory Physiology 2022;322:H105–H115.
13. Fosque BF, Sun Y, Dana H, et al. Neural circuits. Labeling of active neural circuits in vivo with designed calcium integrators. Science 2015;347:755–760.
14. Perez-Alvarez A, Fearey BC, O’Toole RJ, et al. Freeze-frame imaging of synaptic activity using SynTagMA. Nat Commun 2020;11:2464.
15. Chan KY, Jang MJ, Yoo BB, et al. Engineered AAVs for efficient noninvasive gene delivery to the central and peripheral nervous systems. Nat Neurosci 2017;20:1172–1179.
16. Ieda M, Kanazawa H, Kimura K, et al. Sema3a maintains normal heart rhythm through sympathetic innervation patterning. Nature Medicine 2007;13:604–612.
17. Sun Q, Liu S, Liu K, Jiao K. Role of Semaphorin Signaling During Cardiovascular Development. Journal of the American Heart Association 7:e008853.

18. Boczek NJ, Ye D, Johnson EK, et al. Characterization of SEMA3A-Encoded Semaphorin as a Naturally Occurring Kv4.3 Protein Inhibitor and its Contribution to Brugada Syndrome. Circ Res 2014;115:460–469.

19. Nakano Y, Chayama K, Ochi H, et al. A nonsynonymous polymorphism in semaphorin 3A as a risk factor for human unexplained cardiac arrest with documented ventricular fibrillation. PLoS Genet. 2013;9:e1003364.

20. Rienks M, Carai P, Bitsch N, et al. Sema3A promotes the resolution of cardiac inflammation after myocardial infarction. Basic Res Cardiol 2017;112. Available at: https://www.ncbi.nlm.nih.gov/pmc/articles/PMC5443852/. Accessed August 5, 2019.

21. Yaron A, Huang P-H, Cheng H-J, Tessier-Lavigne M. Differential requirement for Plexin-A3 and -A4 in mediating responses of sensory and sympathetic neurons to distinct class 3 Semaphorins. Neuron 2005;45:513–523.